

**Quantum Dot-Sensitized 1D-based Semiconducting
Heterostructures for Optical-related Applications**

| | |
|-------------------------------|--|
| Journal: | <i>Energy & Environmental Science</i> |
| Manuscript ID | EE-PER-07-2018-002143.R2 |
| Article Type: | Perspective |
| Date Submitted by the Author: | 15-Jan-2019 |
| Complete List of Authors: | Yue, Shiyu; Chemistry, Li, Luyao; SUNY Stony Brook McGuire, Scott; Stony Brook University, Chemistry Hurley, Nathaniel ; Stony Brook University, Chemistry Wong, Stanislaus; Stony Brook University, |
| | |

**Metal Chalcogenide Quantum Dot-Sensitized 1D-based
Semiconducting Heterostructures for Optical-related Applications**

Shiyu Yue¹, Luyao Li¹, Scott McGuire,¹ Nathaniel Hurley¹, and Stanislaus S. Wong^{1,*}

¹Department of Chemistry, State University of New York at Stony Brook,

Stony Brook, NY 11794-3400

*To whom correspondence should be addressed.

Email: stanislaus.wong@stonybrook.edu; sswong@bnl.gov

Abstract: In terms of understanding and tuning the optoelectronic behavior of 3rd generation solar cells, such as quantum dot (QD) - sensitized solar cells, QD-based heterostructures represent an excellent and relevant model system and opportunity for analyzing exciton dissociation and charge separation across a well-defined nanoscale interface. In particular, because QDs possess a tunable bandgap and the capability of initiating multi-electron exciton generation, QD-based components tend to be incorporated within optical-related devices, including photovoltaics, light emitting diodes, photoelectrochemical devices, photosensors, and phototransistors. The community has collectively expended significant effort in terms of creating, formulating, and optimizing novel forms of heterostructures comprised of QDs, immobilized by predominantly chemical means onto one-dimensional (1D) motifs, such as but not limited to carbon nanotubes (CNTs) and carbon nanofibers (CNFs). In so doing, it has been noted that key physical variables such as but not limited to (a) QD size, (b) QD loading and coverage, as well as (c) ligand identity can impact upon optoelectronic behavior of CNT-based heterostructures. In recent years, work has extended towards analyzing the opto-electronic ‘cross-communication’ between QDs with related, adjoining 1D semiconducting metal oxides, metal chalcogenides, and metal fluorides. In these examples, other important factors that also are relevant for determining the optical properties of these more generalized classes of heterostructures include parameters, such as (i) morphology, (ii) surface coverage, (iii) chemical composition of the underlying platform, (iv) QD identity, (v) luminescence properties of activating species, as well as (vi) the identity and concentration of dopant ions. In other words, to alter, manage, and manipulate the charge versus energy transfer channels within these materials in a deterministic manner requires basic insights into the close correlation and interplay between physical structure, chemical bonding, and observed performance.

Broader Context:

One means of combining the unique physical and chemical properties of distinctive and complementary classes of material component motifs (such as carbon nanotubes, semiconducting nanowires, metal chalcogenide quantum dots (QDs), and metal oxide nanostructures, as illustrative examples) within an interesting functional configuration can be achieved by generating zero-dimensional QD – one-dimensional nanotube/nanowire-based heterostructures. These materials could be subsequently utilized as novel and interesting constituent building blocks for the assembly of functional light harvesting devices, and because of their architectural and functional flexibility, can potentially open up novel means of using renewable energy sources. In this Perspective, we not only report on strategies for inducing a reliable and reproducible synthesis of several unique and distinctive model 0D-1D-based heterostructured systems but also provide for key insights into understanding charge transfer and energy flow properties within mixed-dimensionality nanomaterial systems for their potential incorporation into a range of practical solar energy conversion devices and light sensitizing configurations. The knowledge gained from these model systems is invaluable for guiding future efforts towards developing additional, chemically tunable, and potentially promising material synthesis targets.

Table of Contents

1. Introduction
2. 0D QD – 1D Heterostructures
3. Carbon-Based Heterostructures
 - 3.1. Carbon Nanotube-Based Heterostructures
 - 3.1.1. Attachment Protocols within Heterostructures
 - 3.1.2. Size and Coverage Density Dependence of Charge Transfer within Heterostructures
 - 3.1.3. Ligand Dependence of Charge Transfer within Heterostructures
 - 3.1.4. CNT-based Heterostructures Incorporating Compositionally Distinctive QDs
 - 3.2. Carbon Nanofiber-Based Heterostructures
 - 3.2.1. CNF-based Heterostructures Used within Dye-Sensitized Solar Cells (DSSCs)
 - 3.2.2. CNF-based Heterostructures within QD-Sensitized Solar Cells (QDSSCs)
 - 3.2.3. CNF-based Heterostructures for Additional Optically-Related Applications
4. Metal Oxide-based Heterostructures
 - 4.1. Binary Metal Oxide-based Heterostructures;
 - 4.1.1. CeO_2 - Photocatalytic H_2 Evolution
 - 4.1.2. SnO_2 - Photocatalytic Degradation and Solar Cell applications;
 - 4.1.3. ZnO - Solar Cell-based Applications;
 - 4.1.4. TiO_2 - Solar and Photocatalytic-based Applications;
 - 4.1.5. Examples of Other Metal Oxide-based Heterostructure Systems
 - 4.2. Complex Metal Oxide-based Heterostructures;
 - 4.2.1. Orthophosphate-based Heterostructures
 - CePO_4 : Initial Proof of Principle- Idea of structure & chemical composition controlling charge vs. energy transfer channels
 - LaPO_4 : Effect of morphology, surface coverage, and dopants on optical properties.
 - 4.2.2. Tungstate-based Heterostructures
 - CaWO_4 : Deliberative band gap alignment between acceptors and donors – Concept of optical behavior mediated by ligands and morphology.
 - CaMoO_4 - CaWO_4 : Roles of QD identity and Metal Oxide Composition
 - Heterostructures incorporating other tungstates with CdS

- 4.2.3. Other Types of Complex Metal Oxide-based Heterostructures
 - β - $\text{Pb}_{0.33}\text{V}_2\text{O}_5$ - Tunable interfacial energy offsets
 - Silicate/Silica-based heterostructures with tunable optical emission
5. Metal Chalcogenide-based Heterostructures
 - 5.1. Binary Metal Chalcogenide-based Heterostructures:
 - 5.1.1. 0D QD – 1D nanorod structures: quasi core/shell dot-in-rod (DIR) structures
 - 5.1.2. Complex 0D QD - 1D - 0D QD Chalcogenide-based DIR Heterostructures
 - 5.1.3. Doped 0D QD – 1D nanorod structures: QD/dopant chemistry with a ZnS host.
 - 5.1.4. Other Examples: Epitaxial growth of 0D-1D hybrid nanostructures.
 - 5.2. Ternary Metal Chalcogenide-based Heterostructures
6. Metal Fluorides
 - 6.1. NaYF_4 : Idea of intrinsic morphology-specific physical surface area and porosity. Trend in energy transfer efficiency correlates well with QD loading.
 - 6.2. Metal Fluoride Systems Beyond NaYF_4
7. Thoughts on Future Directions for the Field
8. Conclusions
9. Acknowledgements

1. Introduction

The ability to synthesize pure crystalline motifs of functional nanomaterials and to understand their transport, optical and mechanical properties lies at the forefront of current materials science research. From a basic science point-of-view, it is important to understand structure-property correlations that fundamentally define unique and unusual behavior within materials. Nanostructured materials offer several potential advantages for solar energy conversion by providing for efficient exciton separation, relatively high electron and hole transport efficiencies, large excitation multiplication possibilities, high surface-to-volume ratios, and short electron-hole diffusion lengths to junctions. All of these interesting attributes are also beneficial for a number of other optical-based device applications, including but not limited to light-emitting diodes (LED),¹ photocatalysts,² light sensing,³ and opto-electronics.⁴ However, the role of nanoscale heterojunctions in promoting exciton dissociation and charge separation is not completely understood. It is expected that junctions between nanomaterials will behave differently as compared with bulk junctions, since the presence of low dimensionality as a structural ‘variable’ in addition to the concomitant high surface area associated with nanostructures in general may collectively promote favorable synergistic interactions.

With respect to these optical-based applications, the key objective is to maximize the longevity and efficiency of charge/exciton separation while simultaneously minimizing competing processes, such as charge recombination. Choosing the correct model material system that will successfully accomplish this goal is therefore necessarily challenging. Specifically, the semiconductor in question can only absorb photons with an energy equal to or greater than its intrinsic band gap energy level in order to generate sufficient numbers of either electron-hole pairs or excitons. These excitons and charges can then be transferred to either counter electrodes

or reactive active sites to initiate the intended photophysical and photochemical activity.⁵ However, undesirable relaxation pathways are possible. For example, the photo-generated electrons and holes can potentially recombine either in bulk or on the surfaces of these semiconductors within a very short time duration, giving off the excess energy in the form of either waste heat or as lower-energy photons.⁶ Therefore, the key issues of (a) constructing a novel composite architecture with a proper band gap alignment so as to improve photon conversion (i.e., light harvesting and exciton generation) while (b) maximizing charge separation and transfer efficiency are two critical problems that have occupied our attention and that of many other groups. As such, we have chosen to investigate novel semiconductor-based, low-dimensional nanoscale heterostructures with the idea of being able to chemically ‘tune in’ and control advantageous and desirable charge and exciton creation and movement. We should also emphasize at the outset, that in this Perspective, in order to simplify the discussion, we will focus primarily on heterostructures incorporating *semiconducting-semiconducting* (S-S) junctions as opposed to broadening our analysis to probing their interesting metal-semiconducting analogues. The implication within these S-S systems is that the valence and conduction bands of the constituent semiconducting units, i.e. band edge positions, can be aligned, relative to each other, so as to promote separation and migration of photogenerated carriers (such as electron-hole pairs) in a tunable and spatially directed manner. The expectation is that such a degree of control will have an impact with respect to the probability of electron-hole recombination⁷ and hence, subsequent operational efficiency for relevant optical-related applications.⁸

Over the years, our group, along with many others in the field, has attempted to gain valuable insights into the basic principles underlying and governing charge separation versus less desirable processes such as either charge recombination or charge trapping (which can limit the

efficiency of charge transfer) within a prototypical heterogeneous nanomaterial system, i.e. zero-dimensional (0D) – one-dimensional (1D) nanomaterial hybrids. In so doing, we have put forth a fundamental emphasis on synthesizing and understanding more complex nanoscale materials, including metal oxide-based heterostructures in particular, of significance to being able to thoughtfully design, tailor, and develop novel and effective classes of light harvesting motifs.

In these efforts, a key strategic direction we and others have pursued has been to combine the unique physical and chemical properties of both 1D systems (such as carbon nanotubes (CNTs) in addition to analogous metal oxide, metal chalcogenide, metal phosphate, and metal fluoride nanowires) with complementary zero-dimensional material motifs (such as metal chalcogenide quantum dots (QDs)) so as to achieve nanotube/nanowire-based heterostructures. These component nanoscale materials were conceptualized as novel and interesting constituent building blocks for the basic understanding and subsequent assembly of optical-based energy harvesting motifs and devices. Because of their architectural and functional flexibility, these unique heterostructures can potentially open up novel means of effectively exploiting, converting, and ultimately storing the essential products of renewable energy sources.

In this Perspective, we present various means for inducing the reliable and reproducible production of several model 0D-1D-based heterostructured systems as well as include an accompanying discussion about the charge transfer and energy flow properties of these materials for their potential incorporation within a range of practical optical-based devices. Specifically, the objective was to (i) systematically vary synthesis reaction conditions and/or preparative methods in order to control key parameters (such as local physical structure and chemical bonding) within a model system that combined both a 0D quantum dot with a 1D material, (ii) characterize the physical structure and opto-electronic properties of these materials, and (iii) put

forth a set of viable structure-property correlations to enable and improve upon our understanding of charge and energy flow in such mixed-dimensionality nanomaterial systems. Indeed, the underlying goal was to tune these composite heterostructures for their potential use and to gauge their possible limitations for practical optical-based (e.g. solar) applications. The knowledge gained from these model systems should hopefully guide the rational production of additional material synthesis targets.

2. 0D QD-1D heterostructures

Nanometer-sized QDs are sometimes referred to as artificial atoms and exhibit properties substantially different as compared with analogous bulk materials. For example, with the quantum confinement effect in these materials, the band gap between the highest occupied molecular orbital (HOMO) and the lowest unoccupied molecular orbital (LUMO) widens with decreasing crystallite size,⁹ leading to unique phenomena such as size-dependent fluorescence emission and size-tunable absorption properties.¹⁰ Hence, in principle, one can design a controlled synthesis of semiconducting chalcogenide-based QDs (i.e., CdS, CdSe, and CdTe), possessing different sizes to span, match, and overlap with the entire solar absorption spectrum.

A more interesting and relevant attribute of QDs has been the discovery that these nanoscale particles can undergo multiple exciton generation (MEG), whereby the injection of a single photon can (in both theory and practice) lead to the generation of more than one (i.e. multiple) electron-hole pair or exciton. That is, whereas with conventional bulk semiconductors, the excess kinetic energy of electrons and holes often gets wasted as either heat or other inefficient, ineffectual energy-intensive processes,^{9, 11} the use of QDs offers an alternative, viable means of potentially exceeding the standard Shockley-Queisser limit of 31% maximum

conversion efficiency¹² by allowing for this excess kinetic energy to be ‘usefully’ absorbed in creating additional excitons.¹³⁻¹⁷ Such a capability is particularly intriguing, as this underlies the potential development of so-called 3rd generation solar cells, such as QD-sensitized solar cells (QDSSCs), with the exciting promise of quantum efficiencies that can exceed 100%.¹⁷⁻²⁰

Experimentally as an example, PbSe QD-based solar cells were reported to maintain an internal quantum efficiency of 130%.²¹ Nevertheless, the limitations of QD-based solar devices cannot be minimized. Specifically, QD-based systems yield high quantum efficiencies but relatively lower power conversion efficiencies (PCE). That is, theoretical thermodynamic conversion efficiencies can be as high as 44%.²² Experimentally, the observed performance metrics of (i) 10.4% within mixed-PbS QD-based systems, denoting one of the highest values reported, and (ii) 3.35% associated with a complementary architecture consisting of TiO₂/CdS QDSSCs wherein the QDs were coated by a Cu-ZnS passivation layer²³ still lag behind those of many other types of dye-sensitized solar cell configurations.²⁴ For instance, third-generation, state-of-the-art perovskite solar cells give rise to PCE metrics as high as either 20%²⁵ or 21%,²⁶ which are more than double in magnitude that of conventional QDSSCs.

This Perspective, which is primarily focused on the QD-based heterostructure ‘building block’ itself, is not necessarily meant to be a treatise on perfecting the design and device engineering of QDSSCs. That discussion is beyond the scope of the present work. Nonetheless, it is worth pointing out that the initial optimism and promise regarding the widespread ubiquity and commercialization of QDSSCs has been tempered by a number of practical considerations.

First and foremost, the reliance on consistent, sustained, and prolonged MEG formation appears to be somewhat problematic and misplaced within the context of a photovoltaic device, since electron-hole pair formation (in addition to electron and hole mobilities themselves) is

necessarily affected by a host of practical processing conditions including QD film thicknesses, surface ligand treatments (and consequently, degree of surface passivation), sizes, and reproducible loading concentrations, in addition to the presence of defects.²¹ Second, to be effective, QDs need to access and absorb radiation across the full range of the solar spectrum through proper bandgap matching, but MEG is not necessarily uniform at all absorption wavelengths,^{27, 28} as the MEG multiplication factor varies with bandgap itself.²⁹ One strategy towards this mitigating for this deficiency has been to incorporate multilayers of QDs of varying mean sizes as well as different chemical compositions and dopant profiles to span ultraviolet (UV), visible, and near-IR regions;^{30, 31} one manifestation of this idea has been the creation of ‘rainbow solar cells’ incorporating differently-sized CdSe QDs deposited onto a TiO₂ nanotube so as to increase the effective capture efficiency of incident light.³² Third, charging processes can increase the possibility of non-radiative Auger relaxation, which can compete with electron transfer from QDs toward the electrodes and thereby lead to a quenched luminescence.³³ Fourth, high charge recombination at the interface of the photoanode and the surrounding electrolyte, perhaps due to poor redox coupling, complicates matters still further.^{34, 35} All of these limitations have led to relatively poor current-potential characteristics and low fill factors (FF) for practical QDSSCs.^{36, 37} Nevertheless, in spite of these drawbacks, QDSSCs still represent a promising low cost and high efficiency alternative,³⁷ whose performance shortcomings may be enhanced with additional research. Indeed, the challenging (and as yet unsolved) problem associated with applying conventional self-assembly and patterning techniques to the spatial organization of QD-based heterostructures over large areas, while simultaneously maintaining their favorable optoelectronic attributes in the process, denotes one such avenue of exploration.^{38, 39}

In terms of other optical applications in which QDs play a significant role, a number of appealing possibilities exist. For instance, it has been reported that QDs can act as a co-sensitizer along with ZnO nanowire array-based photoanodes for photoelectrochemical hydrogen generation,⁴⁰ wherein the presence of a strong absorption by QDs can give rise to a relatively high incident-photon-to-current-conversion efficiency (IPCE). Another example consists of QD-based light emitting diodes (QLEDs), which have begun to be commercially incorporated within large screen display devices. Specifically, as compared with the older generation of liquid crystal display (LCD) and organic light-emitting diode (OLED)-based television (TV) sets, QLED-based TVs maintain a number of advantages, including a wider high dynamic range (HDR), a lower cost, and a larger area of projection, coupled with a better efficiency, a higher pixel resolution, an improved color-quality scheme, and an overall greater stability as compared with conventional analogues.⁴¹ Overall, these favorable advantages of QDs underlie the ‘bright’ future of QLED-based displays and more significantly, highlight the benefits of incorporating QDs within useful and interesting optical-based applications.

Again, as with solar cell-based applications, issues of undesirable charge recombination and short excitonic lifetimes remain. Work in these areas is driven by the prospect of low-cost, large-area, high-efficiency, high-color-quality, stable, all-solution-processed electroluminescent QD-based devices for display and lighting.⁴² Hence, for all of these applications, we have sought to exploit the unique quantum size effect of QDs, which can yield a tunable band gap and light absorption profile, by combining these nanomaterials with the favorable optical characteristics of complementary low-dimensional 1D motifs as a rational strategy for improving upon the observed charge separation and exciton transport efficiency.

Indeed, single-crystalline 1D nanostructures represent desirable structural motifs, as they possess (a) high aspect ratios, (b) fewer lattice boundaries, (c) long segments of smooth crystal planes, and (d) a low number of surface defect sites.⁴³⁻⁴⁷ Moreover, the surfaces of 1D morphologies can be tuned so as to preferentially display different crystal faces.^{48, 49} Within 1-D systems, the charge collection efficiency can be improved by enhanced charge transport.

With single-walled CNTs in particular, electronic band structure calculations predict that the (n, m) indices of the roll-up vector will determine whether a nanotube is either metallic or semiconducting. Interestingly, CNTs can give rise to ballistic charge transport over relatively large distances at room temperature,⁵⁰⁻⁵² because of the possibility of reasonably long electron mean free paths in low-dimensional materials.^{53, 54} This phenomenon of ballistic charge transfer can dramatically reduce the observed resistance of CNTs. Furthermore, excitons have large binding energies and are very stable at room temperature within low-dimensional systems, thereby yielding favorable overall conduction properties.⁵⁵ Recent studies have even shown the quantum dot-like excitonic behavior within an isolated single-walled carbon nanotube (SWNT).⁵⁷ Moreover, when subjected to optical excitation and irradiation, CNTs can undergo detectable charge separation, which can be analyzed using both absorption and emission measurements.⁵⁸ In addition, the formation of hierarchical architectures, consisting of semiconducting CNTs coupled with adjoining semiconducting component units such as QDs, is conducive to potentially reducing undesirable electron recombination.⁵⁶

Carbon nanofibers (CNFs) share many structural similarities with CNTs in terms of a nanoscale hollow structure, but these materials possess a stacked-cup morphology based on an underlying graphene motif.⁵⁹ Moreover, CNFs maintain large active 'surface areas', a high aspect ratio, and a reasonable conductivity, all of which are useful for their incorporation as

viable components of batteries, field-emission devices, supercapacitor electrodes, and electrochemical probes. Furthermore, CNFs can enhance photocatalytic activity by inducing photogenerated charge carrier separation and production.⁶⁰

In general, one individual nanoscale component will have some but not all of the desired properties needed for enhanced overall solar energy utilization. Hence, by ‘merging’ CNTs, CNFs, and additional analogous 1D semiconducting-based motifs with other nanostructures, unique heterostructures, with surprising and potentially unexpected opto-electronic properties, can be generated. Indeed, heterostructures created from distinctive nanomaterial components offer a practical means of not only lowering the exciton binding energy by delocalizing one type of carrier versus the other but also allowing for the option of selectively favoring the formation of one charge carrier channel versus another in order to facilitate charge transfer.⁶¹ As such, the study of the interface itself will be critical towards fundamentally understanding and both physically and chemically tailoring the processes that underlie charge separation, charge recombination, and trapping efficiency, all of which are vital towards reliably improving upon the performance of these materials for optical-based devices.

For example, QDs can be used to enhance absorption. One possible mechanism of collecting the separated charges and minimizing charge recombination in QDs is through close proximity with a 1D structure to harvest the exciton created by absorption in the quantum dot. There are several possible pathways for charge transfer and energy flow in combinations of 0D and 1D materials which could lead to more efficient devices. As an example, chemically attaching semiconducting QDs onto CNTs represents a convenient and practical method of not only capturing photo-induced charges but also transporting them to the electrode surface.⁵⁸ Not surprisingly, CNT-based composites have been reported as building blocks within light

harvesting architectures, because of their excellent carrier mobilities and tunable direct band gaps.^{62,63} Therefore, optimizing exciton harvesting through the mediation of well-defined nanoscale interfaces will be critical, if the use of nanomaterials can result in an increased overall efficiency and potential integration within a real, practical device for solar electric systems.⁶⁴

In this Perspective, we describe various research directions from a number of different groups, aimed at creating specifically tailored 0D-1D heterostructures. The goal of these efforts has been not only to induce favorable exciton harvesting but also to promote either charge transfer or energy transfer through rational chemical strategies and manipulation of key reaction variable(s). In this context, 0D-1D heterostructures have been created in which QDs of diverse sizes and compositions have been immobilized onto underlying 1D platforms, consisting of materials such as but not limited to carbon nanotubes, carbon nanofibers, semiconducting metal oxides, metal chalcogenides, metal sulfides, and metal fluorides. Despite the crucial advantage of functional ‘flexibility’ in terms of being able to tune in a range of physical and chemical capabilities into these heterostructures, 0D-1D composites are not the perfect ‘panacea’ for optoelectronic applications. In part, as implied earlier, this situation has arisen, because these types of composites, which have been meticulously tailored to maintain favorably desirable, reliable, and reproducible performance metrics at the lab scale, are correspondingly difficult to produce over a larger, commercially relevant scale in an environmentally sustainable and cost-efficient fashion. For instance, precise control over important observables such as photophysics has been much more challenging to achieve, replicate, and maintain within practical and stable bulk-like device configurations under standard operating conditions.

3. Carbon-Based Heterostructures

3.1. Carbon Nanotube-Based Heterostructures

In the past within our group, we have successfully demonstrated not only a covalent but also an *in situ* route towards the site-selective synthesis of a series of SWNT and multiwalled carbon nanotube (MWNT) – nanoparticle-based conjugates containing two different types of nanoscale species, i.e. Au nanoparticles (NPs) and CdSe/CdTe QDs.⁷¹⁻⁷⁴ The key point is that we demonstrated the capability of not only spatially controlling where we placed our nanoparticles (e.g. ends versus sidewalls) but also their size, density, and numbers on the CNT surface. Moreover, we quantitatively probed the effects of varying oxidation treatments, precursor concentrations, and incubation times to alter the spatial coverage and distribution of either metallic NPs or semiconducting QDs immobilized onto the MWNT sidewalls and tips.⁷⁵

In this previous work, we and others found that the emission of the CdSe QDs appears to be totally quenched when bound covalently to the MWNT, suggesting a strong and intimate electronic ‘communication’ with the adjoining nanotubes.^{76, 77} To explain the observed emission quenching, the de-activation process of photo-excited CdSe QDs could be attributed to an appreciable and rapid electron transfer and charge injection from the excited semiconducting QDs into the MWNT platform.^{58, 78} That is, once MWNTs were brought into physical contact with these excited QDs, a non-radiative quenching process became competitive with the intrinsic radiative decay process, thereby resulting in the observed decrease in the intrinsic photoluminescence (PL) intensity of the CdSe QDs.⁷⁹ The analogous quenching of the excitonic emission of QDs has also been previously observed in SWNT-QD composites by our group and others.^{73, 74, 76, 77, 80} This phenomenon has been ascribed to the electron-acceptor behavior of SWNTs. That is, photoexcited electrons produced upon illumination of QDs can conceivably flow into SWNTs, nonradiatively, prior to their recombination with photogenerated holes in QDs.

Indeed, an enhanced charge injection from photoexcited QDs into underlying CNTs can contribute to an increased photoconversion efficiency of the corresponding hybrid solar cells.⁸¹

The overall point is that efficient charge separation and transport can be achieved in these nanoscale conjugate systems but needs to be optimized and controlled in a way that it is predictable and hence, useful for potential applications. As such, complementary and innovative pathways have been developed towards accomplishing this objective. Specifically, within CNT-based heterostructures, we have sought to achieve this goal by (i) exploring different attachment protocols with which to combine QDs with the CNTs, (ii) varying constituent QD sizes, and (iii) altering the physical and electronic properties of the linkers connecting the 0D and 1D motifs.

3.1.1. Attachment Protocols within Heterostructures

We have spent significant effort primarily on exploring covalent and non-covalent means of creating the desired heterostructures. Moreover, in our group's experiments, we have specifically chosen to use double-walled carbon nanotubes (DWNTs) as opposed to SWNTs. With DWNTs, in principle, we can achieve the best of all scenarios in that we can selectively functionalize the outer tube for attachment of the QDs and yet still retain the desirable and favorable electronic properties of the inner tube.⁸²

In terms of a traditional chemical means of attaching QDs with CNTs, we devised a covalent attachment method to synthesize DWNT-CdSe QD heterostructures. Specifically, we utilized the 2-aminoethanethiol (AET) molecule in the role of both the capping agent and the linker. We observed a trap emission for CdSe QDs upon coating with AET ligands, and this emission peak was quenched after conjugation with DWNTs, implying charge transfer from CdSe QDs to DWNTs.⁸²

Our next step was to develop a different and alternative attachment method through a parallel non-covalent protocol, which was an inherently milder procedure that did not involve any high temperature, in situ, electrodeposition, or reduction reactions. Our hypothesis was that we could effectively control the degree of charge transfer between these two nanoscale components via tuning of the attachment method. Hence, in exploring the non-covalent route, we expected to take advantage of π - π stacking interactions, which could make full use of the extended and delocalized π -conjugated electron system, characteristic of the CNT surface.⁸³

In practice, we chose 4-aminothiophenol (4-ATP) ligand as the linker between the DWNT and the adjoining CdSe QDs to create the desired heterostructures via two different and contrasting sets of synthesis protocols, namely covalent attachment and non-covalent π - π stacking. Figure 1A and B highlights the transmission electron microscopy (TEM) images acquired of DWNT-4-ATP-capped CdSe QD heterostructures, prepared using covalent and non-covalent methods, respectively. In effect, both procedures successfully yielded heterostructures.

Moreover, photoluminescence and Raman spectra were acquired to compare and analyze the influence of these two distinctive synthetic attachment modes upon the resulting CdSe QD coverage and hence, the degree of charge transfer between QDs and the adjoining DWNTs. That is, we probed charge transfer behavior within 4-ATP-functionalized CdSe QD-DWNT heterostructures (Figure 1D versus F and G). From our microscopy visualization data, it was evident that heterostructures generated by non-covalent π - π stacking interactions gave rise to a higher observed QD coverage density. In parallel, we found not only greater PL quenching but also a larger Raman G band shift with these non-covalently-derived heterostructures (Figure 1H). As such, due to the larger numbers of attached QDs, these non-covalently-bound DWNT-based systems evinced notably more efficient charge transfer as compared with their counterparts,

produced using covalent linker-mediated protocols alone. These observations could fundamentally be ascribed to the retention and conservation of the inherent electronic structure of the DWNTs, characteristic of the non-covalent π - π stacking method.⁸³

In recent years, a novel, ligand-free means of covalently attaching QDs onto MWNTs has been demonstrated. In essence, the 0D-1D ‘connection’ was created through the mediation of robust ligand exchange between the organic ligands (specifically, oleic acid) coating the QDs and the pendant oxygen-containing, carboxylic acid groups on functionalized MWNTs in a process, incorporating an ultrasonication step. This covalent-based approach appeared to provide for a robust and relatively uniform attachment of CdSe QDs onto the external surfaces of the MWNTs, with extended X-Ray absorption fine structure spectroscopy (EXAFS) providing for confirmation of a direct metal-oxygen bond formation between the Cd atoms of the QDs and the oxygen-containing acid moieties of the MWNTs.⁸⁴ Importantly, fast charge transfer between these two species was confirmed by the observations of not only a complete quenching of the steady state PL response of the QDs but also a significant decrease in the measured PL lifetimes of QDs, as noted by time-resolved luminescence studies, consistent with the successful formation of 0D-1D heterostructures with closely interacting constituent components. Specifically, PL lifetimes of pristine, ‘free’ CdSe QDs were more an order of magnitude longer than what were observed for analogous QDs incorporated within these heterostructures. Overall, this ligand free-based protocol allows for a more facile, efficient, and potentially generalizable way to induce the covalent attachment of QDs not only onto CNTs but also onto other functionalizable 1D surfaces.

An ultrasonication method⁸⁴ has been reported as a means of directly depositing CdSe QDs (~3 nm in diameter) onto the external surfaces of carboxylic acid-functionalized MWNTs (fMWNTs). This strategy represents a facile means of attaching QDs onto MWNTs, though the

resulting heterostructure may be correspondingly less stable. The characteristic luminescence peak for these CdSe QDs (at ~ 522 nm) essentially disappeared after introducing in the fMWNTs. The quenching process was indicative of electron transfer from the conduction band of QDs to the fMWNTs, because of the latter's high electron affinity.⁸² With respect to analogous time-resolved fluorescence spectra, the normalized luminescence emission of the 0D-1D composite decayed much faster than that of pure CdSe QDs alone, corroborating the idea that charge transfer accounted for the observed quenching.⁶³

Lastly, we should note that an 'in-situ growth' protocol has been used as a means for fabricating 0D-1D PbSe-SWNT composites.⁸⁵ To be more specific, a pre-heated Pb-precursor stock solution was mixed in with a certain amount of SWNT under argon flow, followed by a rapid injection and quenching of the Se precursor after various reaction times so as to create QDs with size ranges of 5 to 35 nm. PbSe QDs were found to have grown with their (002) planes aligned perpendicularly to the SWNT bundles.⁸⁶ Since the typical Raman D-band peak intensity at ~ 1290 cm^{-1} is a probe of the amount of defects within the SWNTs, the invariance of the D-band intensity for the resulting PbSe-SWNT hybrid upon functionalized suggested that the interaction between QDs and the SWNTs was 'non-covalent'. That is, the intrinsic conjugated π -electron network of the underlying SWNTs was not chemically altered by the reaction, but in fact, appeared to have stabilized growth of the PbSe QDs.⁸⁷ As such, this in-situ growth method demonstrated an effective way of forming QD-CNT composites with controllable QD sizes.

3.1.2. Size and Coverage Density Dependence of Charge Transfer within Heterostructures

It is well known that TEM images (Figure 2A - C), near-edge X-ray absorption spectroscopy (NEXAFS) data (Figure 2D), Raman spectra, and electrical transport measurements (Figure 2F and G) can be separately and independently used as complementary probes of charge

transfer and QD coverage within various types of CNT-based heterostructures. Our novel contribution was to utilize a collective and systematic combination of *all* of these disparate and distinctive measurement techniques in an effort to achieve unique qualitative and quantitative insights within these 1D CNT-0D QD systems. Indeed, our focus was to understand and correlate the effect of varying different parameters, including but not limited to (i) QD sizes and (iii) QD coverage density, with the corresponding charge and energy transfer behavior of our as-prepared nanoscale composites. We should note that the observed QD coverages are fundamentally dependent upon other factors, including, most significantly, QD size, ligand identity, and the attachment method used. As such, our efforts were initially directed towards analyzing charge transfer behavior within nanoscale heterostructures as *a function of both QD size and coverage*.⁸⁸

As such, we probed the structure and morphology of our heterostructures with TEM, and studied the interfaces of a number of different DWNT-CdSe QD heterostructures, possessing various *QD average diameters* (i.e., 2.3 nm, 3.0 nm, and 4.1 nm) (Figure 2A - C). These composites were created using a facile, non-covalent π - π stacking attachment strategy, through the mediation of a bridging hole-trapping thiol linker molecule, i.e. 4-mercaptophenol (MTH) in this case. What we noted from the TEM images was that the observed QD coverages depended on the sizes of the constituent QDs. For example, heterostructures incorporating 4.1 nm diameter QDs yielded the highest coverage densities, whereas heterostructures containing 2.3 nm diameter QDs exhibited the lowest coverage densities (Figure 2A - C).

Our objective was to correlate these structural measurements with the nature of charge transfer, which we detected via (i) changes in the NEXAFS intensities of π^* resonance in the C *K*-edge (Figure 2D) and Cd *M*₃-edge spectra as well as (ii) corresponding trends in the down shifts of the G-band frequency within as-collected Raman spectra. In fact, from an optical

perspective, all of these results were consistent with the idea that the heterostructures possessing the smallest QD sizes (i.e. 2.3 nm) gave rise to the largest driving force for charge transfer, in accordance with what one would have predicted from Marcus theory. Figure 2E highlights the tunneling barriers as well as the band gap alignment of these various systems that support this assertion. We explained the anomalously greater charge transfer behavior of heterostructures incorporating the largest 4.1 nm diameter QDs versus ones characterized by smaller 3.0 nm diameter QDs as being plausibly attributable to the higher QD coverage densities on the underlying DWNT templates, associated with the former (4.1 nm) as opposed to the latter (3.0 nm). To summarize, control over QD size (i.e. the smaller, the better) may have resulted in a rational manipulation of the driving force for charge transfer, but this trend was necessarily impacted to some degree by the actual magnitude of QD loading onto the DWNT surfaces.

In terms of the corresponding field effect transistor (FET) devices constructed from pristine and 4-mercaptophenol (MTH) - capped QD (i.e., 2.3 nm, 3.0 nm, & 4.1 nm) *individual* functionalized DWNTs, we obtained output and transfer characteristics both (i) with and (ii) without illumination to understand transport in these various hybrid structures. In the absence of illumination, the functionalized QD-DWNT FETs revealed a clear threshold voltage shift trend with increasing amount of QD ‘doping’ onto the underlying DWNTs (Figure 2F), that not only was consistent with a charge transfer model but also was found to be dependent upon the QD coverage density. By contrast, in the presence of light, we were able to quantitatively compute a nominal charge transfer efficiency, k_e , between the MTH-capped QDs and the underlying DWNTs, whose inherent magnitude critically depended on the QD size itself and not necessarily on the laser frequency used (Figure 2 G). Smaller QDs yielded smaller effective tunneling barrier heights, and hence, a larger driving force for electron transfer from the QDs to the DWNTs.⁸⁹

To reinforce the importance of QD coverage, mercaptopropionic (MPA)-capped CdTe QD-MWNT heterostructures have been generated by a different group using an ambient, relatively simple, and non-covalent route. Specifically, these hierarchical structures were constructed, based on taking advantage of electrostatic interactions between negatively charged, carboxylate-terminated QDs and self-assembled layers of positively charged, cationic polyelectrolytes, such as poly(4-styrene sulfonate) and poly(diallyldimethylammonium chloride), deposited onto the MWNT surface. In effect, a series of composites was produced with varying QD coverages. It was noted that due to the presence of charge transfer and/or energy transfer from the CdTe QDs to the MWNTs, the observed PL intensity quenching within the heterostructures altered directly and proportionately with increasing QD concentration.⁹⁰

To re-emphasize the significance of coverage,⁹¹ CdS QD-MWNT nanohybrids with different QD loadings were prepared. Decreased PL intensities were observed with higher CdS QD content, suggestive of an enhanced electron-hole separation efficiency with increasing QD coverage. This coverage variation had practical consequences. Specifically, the photocatalytic decomposition efficiencies of malachite green (MG) pollutant increased, as follows: pure MWNTs (34.2%) < 1.0 CdS QD-MWNT (81.8%) < 1.5 CdS QD-MWNT (90.7%) < 2.0 CdS QD-MWNT (92.4%) < 2.5 CdS QD-MWNT (94.9%). That is, the hybrids all exhibited much higher activity as compared with pure MWNTs alone, with the observed photocatalytic activity enhancement ascribable to enhanced electron-hole separation within the heterostructures.

In a very recent report, CdSe QDs with four different sizes ranging from 2.49 nm to 3.06 nm were prepared by a typical hot injection method and immobilized onto purified MWNTs.⁹² To probe the interaction between 0D QDs and 1D MWNTs, UV-visible absorption spectra for all of the various heterostructures were collected. A number of key observations were noted. First, a

red shift in the CdSe excitonic bands was observed, as the QD sizes were increased. Second,, excitonic peaks within the heterostructures shifted to lower wavelength as compared with pure, free CdSe QDs alone, indicative of a charge transfer from the QDs to the underlying MWNTs. To compare the optical conductivity for all of the nanocomposites, terahertz (THz) spectra were acquired. The scattering rates for all of the CdSe QD-MWNT composites decreased gradually with increasing QD sizes; pure MWNTs evinced the highest scattering rates. All of these data could be rationalized by postulating that larger QD sizes were associated with a higher electronic density of states and gave rise to an enhanced charge transport to the underlying MWNTs. These results also were consistent with what has been previously published earlier by other groups.⁹³

3.1.3. Ligand Dependence of Charge Transfer within Heterostructures:

The presence of either a surfactant or a ligand on the QD surface can behave as a stabilizing influence, while also facilitating chemical bonding and electron transport within the context of a larger heterostructure constructed from a number of constituent components. We emphasize the role and importance of two different types of ligands herein. (1) Long-chain alkyl-based surfactants (such as hexadecanoic acid) used during the synthesis process can stabilize a QD solution. However, they are often insulating and can inhibit exciton transport. By contrast, (2) shorter-chain conductive ligands (such as aminoethanethiol) are generally more conductive and by contrast, facilitate exciton movement in solution. Therefore, to highlight the importance of the ligand itself in charge transfer, we addressed the issue of charge transfer in nanotube-QD model systems with the objective of understanding (i) the structural and chemical role of the pendant functional group as well as (ii) the presence of the π -conjugated system within various ligands upon the opto-electronic behavior of as-prepared nanocomposites.⁹⁴

The average diameter of QDs we probed in this set of studies was kept fixed at ~ 4.1 nm, whereas the CNTs were initially treated with a similar oxidative protocol. The **ligands** used to covalently mediate the linkage of the CdSe QDs with the adjoining DWNTs were systematically varied. Specifically, we deliberately chose *p*-phenylenediamine (PPD), 2-aminoethanethiol (AET), and 4-aminothiophenol (ATP) within DWNT – CdSe QD composites (Figure 3A-C), because these ligands maintained different terminal functionalities (i.e. amine versus thiol moieties) and degrees of conjugation (i.e. presence or absence of π -conjugated groups).

We discovered that the choice of ligand had a discernible impact upon the coverage density observed. Specifically, heterostructures generated using PPD-capped QDs yielded the lowest surface coverage of DWNTs, whereas heterostructures produced with AET-capped QDs gave rise to the highest surface coverages of QDs on the underlying DWNT templates. In terms of NEXAFS and Raman spectra, shown in Figures 3D–I, we correlated evidence of charge transfer as manifested in detectable trends associated with (i) shifts of the C *K*-edge peaks in NEXAFS spectra (Figure 3D-F) and (ii) alterations in Raman peak positions (Figure 3G-I), both *before* and *after* CdSe QD deposition onto the underlying DWNT surface. We also found predictable (iii) changes in the observed threshold voltages within our associated transport data.

Our overall data suggested that the key characteristics dictating the charge transfer behavior of the ligands included not only the chemical identity and electron affinity of their pendant groups but also the presence of an underlying π -conjugated carbon framework. For example, the PPD-capped CdSe QDs yielded a much lower coverage density as compared with their AET and ATP-based heterostructured counterparts. We believe that this observation can be ascribed to the weaker binding strength of $-\text{NH}_2$ within PPD as compared with the $-\text{SH}$ groups, characteristic of AET and ATP, in anchoring ligands to the Cd sites spatially localized on the QD

surface (Figure 3A-C). Similarly, the larger enhancement of the C *K*-edge peak within the NEXAFS spectra associated with the AET-based heterostructures versus the PPD-bounded ones could be attributed not only to their greater associated QD coverages but also to the inherently higher electron affinity of AET's terminal –SH groups versus PPD's pendant –NH₂ moieties (Figure 3D-F). Moreover, based on trends noted not only with the experimental C *K*-edge spectra (specifically the C=C π^* transition) but also with the DWNT G⁺-band down-shift in the Raman spectra, ATP's intrinsic π -conjugated, electron-rich aromatic system likely mediates and facilitates greater charge transfer as compared with its aliphatic AET counterpart (Figure 3G-I).

Theoretical findings were generally consistent with all of these experimental results. Moreover, theory corroborated previous published data which implied that electron-rich, conjugated systems are much more efficacious at enabling the charge transfer process as compared with their non-conjugated counterparts.⁹⁵ Highlighting the key role of small molecule-mediated optoelectronic behavior in heterostructures, we noted the peculiar selectivity of ligands for tuning QD coverages, electron transfer efficiency, and ultimately, optical performance.⁹⁶

The significance of ligands with respect to QD-MWNT architectures, created through covalent attachment, has also been emphasized by other groups. As a specific example, CdSe@ZnS core/shell QDs have been directly attached onto not only the CNT sidewalls using a diazonium salt-based linker but also the corresponding CNT ends with the mediation of mercaptotriethoxysilane. In both cases, a significant PL quenching effect was observed, which highlighted a degree of charge transfer from the QDs to the CNTs. Interestingly, it was the species at the CNT ends as opposed to the sidewalls, which yielded a more significant PL peak intensity decrease, despite the fact that mercaptotriethoxysilane is insulating. The explanation for this observation was attributed to a higher electron mobility permitting for a more reliable charge

transfer, induced by the presence of mercaptotriethoxysilane. This ligand is effectively a shorter linker than the thiolated diazonium coupling agent, thereby permitting for a 'direct', less diluted, and hence more effective charge transfer from the QDs to the adjoining CNTs. The diazonium linker was also thought to polymerize in an undesirable fashion on the surfaces of the CNTs.⁹⁷

In a similar vein, the controlled assembly of organic-inorganic heterostructures, consisting of individual, DNA-wrapped SWNTs selectively coupled to single QDs, which were spatially localized at the nanotube ends, in aqueous solution has been successfully reported. Specifically, the sidewalls of the SWNTs were stabilized and encapsulated by DNA, such that amino-terminated CdSe/ZnS core/shell QDs could be attached onto SWNT ends via covalent bond-inducing amidation reactions. Time-resolved and steady-state photoluminescence studies performed both in solution and on the surfaces of these single nanohybrids yielded expected evidence of an electronic coupling between the QDs and the SWNTs. It was even explicitly proposed that varying the lengths and chemical nature of the ligands would allow for deliberative tuning of the electronic coupling at the organic-inorganic interface, of relevance for creating novel QD-based optoelectronic and light-energy conversion devices.⁹⁸

3.1.4. CNT-based Heterostructures Incorporating Compositionally Distinctive QDs

Variations on the QD-CNT theme exist. For instance, one could consider using alternative QDs. Specifically, apart from conventional chalcogenide CdSe, CdS, and CdTe QDs, analogous heterostructures have been created by using either core-shell InP/ZnS QDs or ZnO QDs, which possess different absorptive and emissive properties.

As one example, a combination of QDs with MWNTs was probed as a potential additive within the active layer of polymer-based solar cells. Specifically, InP/ZnS core/shell QDs with an emission peak wavelength of 660 nm were added to MWNTs within a non-conducting and

transparent polymethyl methacrylate (PMMA) matrix. In this case, the role of the QDs was designated as a light sensitizer to enhance the long wavelength response of the solar cell, whereas the CNTs were meant to increase overall charge carrier efficiency by enhancing charge separation and conductivity.⁹⁹

Composites composed of ZnO QDs deposited onto O₂ plasma-treated CNTs through a vapor-liquid-solid (VLS) method give rise to a cathodoluminescence profile characterized by a weak UV emission peak coupled with two distinctive and strong green emission peaks at 2.51 eV and 2.4 eV, the latter of which could be attributed to Zn-rich band-to-donor and oxygen-rich ZnO band-to-acceptor transitions, respectively.^{100, 101} Moreover, these heterostructures evinced dramatically enhanced field emission properties, likely due to the prevalence of extra electron emission paths and higher charge carrier concentrations.¹⁰²

ZnO QD-MWNT heterostructures have also been reported as excellent photo-sensitive, high-performance ultraviolet photodetectors. In particular, the conjugation of these two components enabled a direct transfer of photoinduced charge carriers from ZnO QDs to MWNTs, thereby creating efficient electrical pathways which lessened charge recombination during UV exposure. Overall, the hybrid heterostructures exhibited an excellent reversible photoresponse behavior and superior response times in photodetection as compared with control devices.¹⁰³

3.2. Carbon Nanofiber-Based Heterostructures

The morphology, growth mechanism, degree of surface oxidation,¹⁰⁴ and corresponding physical properties (i.e. optical and electronic) of CNFs are typically controlled by synthesis methods such as chemical vapor deposition (CVD),¹⁰⁵ electrospinning,¹⁰⁶ and the use of a hard template.¹⁰⁵ Each of these protocols has specific advantages. As an example, the morphology of as-produced CNF can be controlled by tailoring CVD growth conditions.¹⁰⁵ Electrospun carbon

nanofibers fabricated via electrospinning can be produced not only on a large-scale but also with uniform alignment such that complex functional three-dimensional structures can be created from one-dimensional constituent nanofiber components.¹⁰⁶ Interestingly, with CNFs, control over both structure¹⁰⁷ and degree of oxidation¹⁰⁴ can lead to perceptible enhancements in optical performance. Given the high electrical conductivity of CNFs,¹⁰⁸ CNF-based heterostructures have been incorporated as components of solar cell configurations and photocatalysts.

3.2.1. CNF-based Heterostructures Used within Dye-Sensitized Solar Cells (DSSCs)

Dye-sensitized solar cells (DSSCs) have been reported as a promising alternative to conventional energy conversion device, because of inherent advantages associated with a simple fabrication procedure, a relatively low cost, and a high power conversion efficiency.^{109, 110} A traditional DSSC is typically composed of (i) a dye-sensitized photoanode, (ii) an electrolyte containing a redox couple of I^-/I_3^- , (iii) a porous semiconducting film, and (iv) a standard platinum counter electrode (CE), also known as a catalytic cathode. Platinum is typically used as the counter electrode, because it can not only serve as an efficient catalyst for the redox reaction within the electrolyte but also assist in transferring electrons. However, as a precious metal, Pt is both scarce and comparatively expensive.¹¹¹ Hence, replacing Pt with a more earth-abundant and low-cost material, such as but not limited to carbonaceous compounds, conducting polymers, metal sulfides, as well as metal oxides,¹¹² while simultaneously retaining Pt's excellent electrocatalytic activity, remains a significant challenge. Typically, as compared with Pt itself, these material alternatives tend to exhibit a decreased efficiency, mostly due to their poor charge transfer kinetics at the electrode/electrolyte interface.¹¹³

Carbon nanofibers possess a relatively more efficient conductivity and a better chemical stability as compared with most materials studied, which can lead to not only a lower charge

transfer resistance but also a greater availability and abundance of reaction sites, all of which can promote the overall efficiency of DSSCs.^{109, 114} Thus, the combination of CNFs with QDs within a 0D/1D composite represents a viable architectural motif as the counter electrode that can be used within a DSSC configuration. Indeed, experimental investigations of these composites have revealed that the synergistic effects introduced by the simultaneous presence of both the 1D carbon nanofiber support and the 0D QDs can give rise to a higher catalytic activity, an increased chemical stability, and an enhanced energy conversion efficiency.^{115, 116}

As examples, composites composed of metal sulfides with CNFs are thought to promote charge transport within a solar cell device. Specifically, various compositions of 0D Co_xS_y nanoparticles, such as Co_3S_4 , have been combined with 1D CNFs to create 0D/1D hybrids, created through the mediation of a hydrothermal treatment. Specifically, an aqueous mixture of $\text{Co}(\text{NO}_3)_2$ and cysteine coupled with carbon nanofibers was heated within a Teflon-lined autoclave at 160°C for 12 h; the final product was isolated by means of filtration, followed by washing with alcohol. TEM and SEM images indicated that as-prepared 0D Co_3S_4 nanoparticles were relatively evenly dispersed on the external surface of CNFs without apparent aggregation. To highlight the role of the carbon nanofiber support towards Co^{3+} reduction reaction, cyclic voltammetry (CV) analysis was carried out on pure Co_3S_4 nanoparticles as well as on the $\text{Co}_3\text{S}_4/\text{CNF}$ composite itself. Current densities measured for the Co^{3+} reduction process followed the sequence of $\text{Co}_3\text{S}_4/\text{CNF}$ composite (i.e., 0.308 mA/cm^2) > pure Pt (i.e., 0.236 mA/cm^2) > pure Co_3S_4 (i.e., 0.205 mA/cm^2). Additionally, the peak-to-peak separation (ΔE_p) value of the 0D/1D composite decreased significantly with respect to pure Co_3S_4 nanoparticles alone. Since ΔE_p is inversely proportional to the charge transfer rate, these findings implied that the composite possessed an increased charge transfer rate as compared with the pure Co_3S_4

nanoparticulate control sample. The high current density and relatively small ΔE_p value both were consistent with the superior catalytic activity of the 0D/1D composite as compared with the pure Co_3S_4 control alone. To further ascertain the photovoltaic potential of these as-prepared hybrid materials, a functional cell was subsequently fabricated and tested.

In effect, a high photovoltaic performance was noted with these as-fabricated heterostructures used as the CE within DSSCs.¹¹⁷ Specifically, the solar cell employing $\text{Co}_3\text{S}_4/\text{CNF}$ heterostructures as the CE evinced a PCE value of 9.23%, which is higher than that of the solar cell incorporating controls consisting of either a pure Pt CE (i.e. 8.38%), a pure Co_3S_4 CE (i.e. 6.77%), or a pure carbon nanofiber CE (i.e. 6.04%). The high PCE demonstrated by the DSSC utilizing $\text{Co}_3\text{S}_4/\text{CNF}$ as the counter electrode can be explained by its superior incident light reflecting ability, which resulted in a higher photo-generated electron efficiency. Hence, because the 0D/1D composite heterostructures gave rise to not only a higher photovoltaic performance within the DSSC but also a more favorable catalytic activity towards the Co^{3+} reduction reaction as compared with control samples, all of these results collectively confirmed the validity of substituting the Pt CE with as-prepared $\text{Co}_3\text{S}_4/\text{CNF}$ composites.

A similar scenario was observed with Co_9S_8 QDs, dispersed uniformly onto the surface of an underlying 1D CNF support (Figure 4A-C).¹¹⁸ The $\text{Co}_9\text{S}_8/\text{CNF}$ hybrid was similarly synthesized using a hydrothermal protocol but with a slightly different combination of precursors and solvents; moreover, the isolated powder was further annealed under nitrogen at 350°C for 2 h so as to notably improve upon sample crystallinity. CV curves were also obtained for the composite towards the oxidation and reduction of the I^-/I_3^- system. Specifically, the $\text{Co}_9\text{S}_8/\text{CNF}$ composite yielded a higher current density as compared with that of both pure Pt and CNF alone, thereby implying an enhanced catalytic activity associated with the hybrid. Figure 4D highlights

how photoelectrons generated at the anode could flow via the external circuit to the CE; the Co₉S₈/CNF composite (i.e. the CE) at the counter electrode injects electrons to the electrolyte to complete the electrical circuit. To evaluate the photovoltaic performance of these as-prepared heterostructures within the DSSC, relevant experimental parameters, such as the short circuit current density (J_{sc}), the open circuit voltage (V_{oc}), and the power conversion efficiency (PCE), were examined under AM 1.5 illumination with a light intensity of 100 mW/cm² (Figure 4E). In effect, the composite used as the counter-electrode ($J_{sc} = 23.91$ mA/cm², $V_{oc} = 0.676$ V, and PCE = 8.37%) dramatically outperformed that of the pure CNF alone ($J_{sc} = 19.20$ mA/cm², $V_{oc} = 0.641$ V, and PCE = 6.23%) with the improved metrics of the composite ascribable to the synergistic combination of Co₉S₈ nanoparticles coupled with the CNF support. Moreover, stability testing of the DSSC incorporating the 0D/1D hybrid as CE exhibited outstanding performance. In effect, 98.5% of the original PCE value was retained, even after thirty days of testing. Hence, 0D cobalt sulfide / 1D carbon nanofiber heterostructure denote a promising alternative material with which to substitute pure Pt as the counter electrode within a DSSC.

In the case of metal oxides, molybdenum oxides (MoO_x) in particular are considered as an attractive material for energy-related applications, because of their high theoretical capacity, sizeable conductivity, as well as attractive chemical stability.¹¹⁹ One such study utilized a solvothermal fabrication protocol, involving heating a homogeneous dispersion, comprised of CNFs and ammonium molybdate within aqueous ethanol, for 12 h at 180°C to yield a MoO₂/CNF composite. The expected uniform spatial distribution of 0D MoO₂ nanoparticles on the external surface of 1D CNF of as-synthesized heterostructures was confirmed by means of TEM and SEM. The corresponding chemical composition was measured and verified using a combination of TEM-based elemental mapping, XRD, and XPS. Electrochemical results (i.e.,

CV curves) revealed that the composite in the role of the DSSC CE maintained a higher catalytic activity for the Γ/I_3^- redox couple. In particular, the composite yielded a higher current density (i.e., 5.4 mA), and more importantly, a decreased ΔE_p value (i.e., 0.450 V) as compared with a conventional Pt (i.e., 5.2 mA for current density and 0.499 V for ΔE_p) control thereby highlighting the effective performance of the composite as a counter electrode.

To examine the potential applicability of such a heterostructure as a viable component within a realistic functioning cell environment, photocurrent density versus photovoltage (J-V) data were collected for both the composite and pure Pt, operating as the CE within DSSCs. Not surprisingly, the MoO_2/CNF composite as the CE evinced a noticeably enhanced photovoltaic performance ($J_{sc} = 21.12 \text{ mA/cm}^2$, $V_{oc} = 0.722 \text{ V}$, and $\text{PCE} = 7.60\%$) with respect to the Pt CE ($J_{sc} = 20.70 \text{ mA/cm}^2$, $V_{oc} = 0.685 \text{ V}$, and $\text{PCE} = 7.34\%$) alone. In addition to the obvious improvement in PCE, it is also worth noting that the thickness of the MoO_2/CNF composite CE film had a perceptible impact upon the observed photovoltaic results. Specifically, the 20 μm thick film exhibited an optimized PCE value of 7.6%, which was not only superior to that of Pt alone (7.34%) but also surpassed the corresponding activity of both the 10 μm thick (i.e. 6.99%) and the 30 μm thick films (i.e. 5.63%), respectively. To more thoroughly examine the photophysical nature of the composite system, multiple, representative IPCE curves spanning the wavelength range from 300 to 800 nm were acquired. At the peak position of $\sim 500 \text{ nm}$, the composite gave rise to the best IPCE value of $\sim 75\%$, whereas the corresponding standard Pt and pure CNF samples yielded 70% and 60%, respectively. These data for the MoO_2/CNF composite reflected the higher light collecting efficiency of the anode. Hence, overall, the relatively low cost and the higher photovoltaic efficiency of as-fabricated MoO_2/CNF composites yielded a very promising CE for DSSCs.¹²⁰

With respect to metals, heterostructures, composed of Cr-doped Pt₃Ni nanoparticles supported onto carbon nanofibers, have been synthesized and subsequently utilized as a counter electrode within DSSCs.¹²¹ With respect to the order for the catalytic activity towards I⁻/I₃⁻ redox couples, the CV curves demonstrated it to be the following: Cr-Pt₃Ni/CNF composite > Pt standard > CNFs. Whereas the power conversion efficiency of a bare CNF counter electrode and a bare Pt counter electrode were reported to be 5.75% and 7.04%, respectively, as-prepared heterostructures evinced correspondingly higher values of as much as 8.76%. The enhanced PCE performance of the composite as a counter electrode was ascribed to its rapid charge transfer capability, resulting in not only a higher short-circuit current density but also an increased fill factor. These data are consistent with the observed electrochemistry. Specifically, composites fabricated with Mo-doped Pt₃Ni nanoparticles deposited onto carbon nanofiber supports¹²² similarly showed superior catalytic activity towards the I⁻/I₃⁻ regeneration reaction with respect to pure Pt, and not surprisingly, exhibited an improved value of 9.47% as a DSSC counter electrode, when measured with a simulated full solar intensity (AM 1.5 G). All of these examples highlight the viable idea of substituting Pt with complex heterostructures, characterized by equal if not superior performance metrics within actual devices.

3.2.2. CNF-based Heterostructures within QD-Sensitized Solar Cells (QDSSCs)

Replacing the functional role of dyes with that of QDs within the context of QDSSCs enables one to exploit the size quantization effect and MEG potential of QDs.^{123, 124} Nevertheless, the relatively low solar energy conversion efficiency of QDSSCs has limited their viable and ubiquitous commercial applicability. As with DSSCs, one primary area of concern relates to the cathode (i.e. counter electrode). Specifically, the performance of a conventional Pt counter electrode is hindered not only by the strong absorption of sulfur-containing species within the

electrolyte but also by its low chemical stability.¹⁰⁶ Whereas alternative cathode materials, such as Cu_2S ¹²⁵ and ZnS ,³⁵ have demonstrated an improved photovoltaic performance at lower cost, CNFs represent another promising and cost-effective substitute for Pt as a counter electrode.¹²⁶

QDSSCs consisting of a tin oxide photoanode and a CNF counter electrode gave rise to a 2.5% power conversion efficiency, a value higher than that of Pt (i.e., 2.1%).¹²⁷ Heterostructures composed of CuS controllably grown onto electrospun CNFs by a hydrothermal method have been used as an effective counter electrode within QDSSCs to facilitate charge transport, reduce charge transfer resistance, and decrease interfacial recombination, so as to improve overall efficiency.¹²⁸ In terms of sample preparation, an aqueous mixture of electrospun CNFs, CuCl_2 , and L-cysteine was transferred into a Teflon-lined autoclave and heated to 160°C for 12 h. The morphology of the CNF substrate both (i) before and (ii) after CuS nanoparticle deposition was studied by SEM; collected images confirmed the relatively uniform attachment of 0D CuS nanoparticles onto the underlying 1D CNF surface. TEM elemental mapping and XPS were also used to analyze elemental distribution and oxidation states. In effect, the CNF ‘platform’ served to bridge the adjoining CuS nanoparticles together, thereby exposing more active sites and enabling the production of spatial pathways to facilitate electron transport, all of which are beneficial for catalysis. Hence, when used as a counter electrode within QDSSC devices, the trend in efficiency for the various material systems tested was in the order of CuS/CNF composite (i.e. 3.86%) > CuS nanoparticles (i.e. 3%) > standard Pt (i.e. 2.1%) > CNF (i.e. 1.62%). The enhanced charge transfer promoted by the CuS/CNF composite, ascribable to a synergistic combination of catalytically active CuS nanoparticles coupled with the superior charge transport of 1D carbon nanofibers, likely contributed to the excellent PCE value of the QDSSC. Specifically, electrochemical impedance spectroscopy (EIS) results on the CuS/CNF

composite (used as the CE) highlighted that whereas the CNF support improved the observed charge transfer efficiency, the complementary metal sulfide possessed not only low resistance but also yielded a high catalytic activity for the polysulfide redox reaction.

3.2.3. CNF-based Heterostructures for Additional Optically-related Applications

Solar-driven photocatalysts is regarded as an effective and economical pathway for environmental remediation. In effect, visible light occupies a substantial component of the solar spectrum,¹²⁹ and semiconductors with wide band gaps, such as metal oxides, have often been used to photocatalyze the degradation of organic-based pollutants and model dye compounds in water.¹³⁰ As a typical example, 0D/1D composites composed of titanium oxide (TiO₂) nanoparticles, decorated onto the surfaces of CNFs, photocatalyze methylene blue degradation¹³¹ in as little as 2 min, which is much faster as compared with bare TiO₂ nanoparticles (i.e., 60 min).

ZnO is recognized as a very promising photocatalyst, due to its wide band gap (3.37 eV), high quantum efficiency, and excellent photosensitivity.¹³² However, the fast recombination of charge carriers within ZnO limits its applicability as an effective photocatalyst. Nevertheless, the addition of CNFs as a support material can promote the potential for photogenerated electron transfer coupled with a reduction in electron-hole recombination. Not surprisingly, ZnO/CNF composites were more active towards organic dye degradation under UV irradiation¹³³ as compared with bare ZnO alone. Yet, what also proved to be significant was the nature to which ZnO was attached onto the underlying CNF walls. Specifically, wet chemical treatments were used to construct different variants of identical composites, whose precise formulation depended upon merely interchanging specific reaction steps. In effect, these CNF-based heterostructures were characterized by either (i) an inhomogeneous distribution and agglomeration of non-uniformly-sized ZnO particles on relatively defective CNF surfaces or (ii) a uniform distribution

of more monodisperse, smaller, and well-formed ZnO particles on comparatively defect-free CNF surfaces, as implied by SEM and TEM data. The latter composites exhibited a ~2-fold higher rate constant towards organic pollutant (i.e. Rhodamine B or RB) degradation as compared with the former. This evident catalytic enhancement could be explained by an improved interfacial contact between ZnO and CNF, owing to a decreased amount of CNF defects, which in turn led to a more efficient charge transfer process. Mu et al. also fabricated ZnO QD (size < 5 nm) - CNF heterostructures via a combination of electrospinning and hydrothermal techniques under pH-controlled conditions.¹³⁴ Their photocatalytic activity towards organic pollutants was tested. Experiments were carried out under UV light irradiation, and the measured RB degradation turned out to be 70% and 96% for pure ZnO and ZnO-CNF composites, respectively. Additionally, PL emission spectra of as-synthesized ZnO-CNF composites exhibited a much lower intensity with respect to the ZnO control sample, reinforcing the efficiency of charge separation within the 0D/1D heterostructures.

It is assumed that electrons generated by the ZnO QDs transferred to the CNF supports, while holes reacted with surface oxygen species; the as-generated hydroxyl radicals produced on the ZnO surface also assisted in organic pollutant decomposition. The same group also noted the improved catalytic behavior of an analogous recyclable composite, composed of a CNF support coupled with In₂O₃ nanocubes. As with the ZnO/CNF system, the enhanced photogenerated electron-hole separation within the comparable In₂O₃/CNF system was substantiated by the PL emission behavior, wherein the In₂O₃/CNF composite evinced a noticeable decrease in PL intensity as compared with In₂O₃ alone. The increased charge separation efficiency yielded not only longer charge carrier lifetimes but also consequentially, an improved photocatalytic activity for the In₂O₃/CNF hybrid. In effect, the composite's superior performance in all of these

examples was attributed to the idea that charge recombination was inhibited and charge separation was enhanced, because of the cooperative coupling of the two constituent components, whereas charge transfer was improved upon, largely as a result of the highly conductive CNF.¹³⁵

4. Metal Oxide-based Heterostructures.

Over the years, in a parallel effort, our group has been actively involved in the development of innovative syntheses of nanotubular, nanorod, and nanocube formulations of oxide (particularly, technologically significant perovskites), sulfide, and fluoride-based materials.¹³⁶⁻¹³⁹ In the context of this Perspective, metal oxides are able to not only enhance the efficient movement of photo-generated excitons but also improve upon charge separation and transport capabilities for photovoltaic, light harvesting, and/or light-emitting diode applications. As such, we have been particularly interested in reliably tuning and tailoring photo-induced charge transfer and energy transfer processes within more generalized (i.e., apart from carbon-based) classes of composite heterostructures through manipulation of key reaction variables, such as (1) the excitation wavelength used; (2) the presence or absence of dopant species; (3) morphology and crystallinity; (4) QD coverage and density; (5) QD identity; as well as (6) the chemical composition of the relevant constituent metal oxide/fluoride/chalcogenide in question. As an example of the significance of each reaction parameter, we note that the precise morphology of the metal oxides themselves controls not only the extent of exposed reactive surface area but also the quantitative loading ratio and coverage density of immobilized QDs.

To highlight the importance and relevance of these metal oxide-based structures for solar cell applications, it is worth noting that all-inorganic heterostructured *n-p* junction devices created from ‘inks’ of colloidal PbS QDs (e.g, light harvester) and anatase TiO₂ nanorods (e.g.

electron acceptor) have been fabricated under relatively mild, room temperature, and solution-based conditions. Through Kelvin probe force microscopy and femtosecond pump and probe spectroscopy measurements, electron transfer was reported to have occurred at the interface between the QDs and the anatase nanorods with an overall observed power conversion efficiency of ~3.6% on glass and ~1.8% on flexible plastic substrates, respectively.¹⁴⁰

In essence, a fundamental understanding of metal oxide-based heterostructures could lead to an improved capability to tailor the optoelectronic properties of constituent nanomaterials for possible incorporation within functional light harvesting and PV devices. Composite architectures, in which structure, morphology, and chemical composition can be treated as independent reaction ‘variables’ with which to deliberately control optical behavior, offer an opportunity with which to initiate and promote highly efficient charge separation by purposely modulating localized chemical interactions within discrete constituent units.

4.1. Binary Metal Oxide-based Heterostructures

As alluded to thus far, metal oxides represent one of the most diverse classes of materials, with important structure-related properties, including superconductivity, ferroelectricity, magnetism, colossal magnetoresistivity, conductivity, and gas sensing capabilities. More precisely, metal oxides are plentiful and functionally active for many different types of applications. In this context, our group has expended a lot of effort in the use of molten-salt synthetic methods, hydrothermal protocols, and ambient template-directed techniques as viable methodologies to generate homogeneous and monodisperse metal oxide nanostructures with precise size and shape control without necessarily sacrificing on sample quality, purity, and crystallinity. With respect to this Perspective, a number of metal oxides, especially their doped analogues, possess intrinsically interesting optical (i.e. desirable band gaps), electronic, and

catalytic properties that render them as viable candidates with which to couple with 0D QDs so as to create novel, high-performing composites. As an illustrative example, 1D WO_3 nanostructures linked with CdS QDs are highly effective in terms of their photocatalytic efficiency, an observation which can be attributed to their enhanced visible light absorption and efficient charge separation potential.¹⁴¹ Due to space constraints, our discussion focuses on a subset of arguably more ‘commonly used’ metal oxides, such as CeO_2 , SnO_2 , ZnO , and TiO_2 .

4.1.1. CeO_2 - Photocatalytic H_2 Evolution

For example, doped cerium dioxide (CeO_2) is a highly sought-after semiconducting photocatalyst, because of its stability, natural abundance, relative non-toxicity, and low-cost.¹⁴² Recently, a heterostructure combining 1D CeO_2 nanorods with 0D CdSe QDs was created using a simple hydrothermal method in which the amount of CdS QDs coating the external surfaces of the nanorods could be quantitatively controlled by the molar ratio of QDs and cerium precursors utilized in the reaction. Photocatalytic hydrogen evolution experiments were performed to compare the activity of pure CeO_2 nanorods with that of analogous CdS / CeO_2 heterostructures. The resulting data (i.e. H_2 generation) were consistent with a very large enhancement observed for the heterostructures (i.e., up to $101.12 \mu\text{mol h}^{-1} \text{g}^{-1}$) as compared with that of the nanorods alone (i.e., $2.25 \mu\text{mol h}^{-1} \text{g}^{-1}$). Moreover, PL measurements indicated that the emission intensities for the CdS / CeO_2 heterostructures were considerably lower than those of pure CeO_2 . This evident quenching in emission suggests that the interface between CdS QDs and the adjoining CeO_2 promotes effective charge separation. This observation can be explained by the bandgap alignment of these two materials with the Z-scheme, which the CdS QDs and CeO_2 nanorods consume the h^+ species generated by CdS QDs and the corresponding e^- produced by CeO_2 nanorods. By contrast, average lifetime measurements for CdS / CeO_2 heterostructures and pure

CeO₂ yielded values of 4.05 and 2.14 ns, respectively. These cumulative findings suggest that CdS / CeO₂ heterostructures maintain a faster and more effective charge separation and transfer of charge carriers as compared with pure CeO₂ alone, thereby confirming the higher photocatalytic activity of these composite heterostructures.¹⁴³

4.1.2. SnO₂ - Photocatalytic Degradation and Solar Cell Applications

SnO₂ possesses a wide band gap of 3.6 eV at 300 K, and as such, has been incorporated as a component of not only (i) photocatalysts but also (ii) electrodes of DSSCs.¹⁴⁴ With respect to photocatalytic activity, CdS QD/SnO₂ nanorod-based heterostructures were found to induce the degradation of both methylene blue¹⁴⁵ and Congo Red solution¹⁴⁶ at notably higher levels as compared with pure SnO₂ nanowires alone. It was proposed that significant quenching of the band edge emission for not only SnO₂ but also CdS induced efficient charge separation. Analogous CdSe QD / SnO₂ nanowire-based heterostructures could initiate the corresponding photodegradation of hydrochlorothiazide.¹⁴⁷

With respect to solar cell applications, flower-like clusters of SnO₂ nanorods sensitized with CdS QDs evinced an IPCE of 6.5% in the range of 400 to 440 nm,^{147, 148} with similar findings reported for analogous 1D SnO₂ – 0D CdS hierarchical composites.^{145, 146, 149} With heterostructures generated from SnO₂ nanowires and CdSe QDs,¹⁵⁰ the photocurrent was found to have enhanced by as much as 350% upon deposition of CdSe QDs onto the underlying SnO₂ nanowire surface. Promising data were also collected on a series of heterostructures composed of Cd-free QDs consisting of CuInS₂ (CIS), ZnS-CuInS₂ (ZCIS), and core/shell ZCIS/ZnS, respectively coupled with SnO₂ nanowires.¹⁵¹ In particular, the photoresponses of pure SnO₂ nanowires and of the corresponding nanowires immobilized with CIS, ZCIS, and ZCIS/ZnS QDs were measured at 325 and 488 nm, denoting energies both higher and lower than the intrinsic

band gap of SnO₂, respectively. At 325 nm, an increase in the photocurrent of about 700%, 400%, and 200% for the CIS, ZCIS, and ZCIS/ZnS QD-based heterostructures, respectively, was measured. At 488 nm, the photocurrent for SnO₂ was barely detectable, as expected, since the excitation energy was lower than that of the band gap for SnO₂, but the observed photocurrents for the attached CIS and ZCIS QDs themselves increased by ~400% and 200%, respectively. These collective data were consistent with charge transfer emanating from the type II band alignment between constituent QDs and SnO₂ nanowires within the heterostructures.

4.1.3. ZnO: Solar Cell-based applications

ZnO is a low-cost, II-VI compound semiconductor, with a direct wide band gap value of 3.37 eV, and it possesses high mechanical, thermal, and chemical stability. Nevertheless, ZnO's wide band gap limits the absorption of visible light and decreases the light conversion efficiency. Apart from doping, chemical coordination with QDs offers a viable means for improving upon and extending ZnO's light absorption range.

1D ZnO/CdS QD core-shell heterostructures were initially formed using a sonochemical synthesis protocol.¹⁵² PL spectra highlighted significant quenching for ZnO/CdS QD heterostructures as compared with both pure ZnO nanorods and pure CdS QDs, suggestive of the presence of charge transfer. Additional developments of this composite centered on applications as diverse as but not limited to energy and catalysis-related fields, such as photoelectrochemical water splitting,^{153, 154} photodegradation,^{155, 156} and photocatalysis.¹⁵⁷

Regarding solar cell applications, the initial 1D ZnO/CdS QD heterostructures incorporated within a solar cell configuration yielded power conversion efficiencies of up to 0.54%,¹⁵⁸ with additional efforts only marginally improving upon this value.¹⁵⁹⁻¹⁶¹ As an example of some of the additional strategies developed to rectify this low efficiency problem, the

IPCE of ZnO flower-like nanoarrays sensitized with a layer of CdS QDs¹⁶² could be more than doubled by coating the ZnO/CdS heterostructure with a layer of CdSe QDs, thereby yielding a measured power conversion efficiency of 1.08%. PL spectra of bare ZnO gave rise to a narrow emission band at 407 nm, attributed to the near-band-edge emission of ZnO. Within the ZnO/CdS heterostructures, the band edge emission was significantly quenched and blue shifted, thereby implying that photogenerated electrons could be efficiently transferred from CdS to ZnO. Upon addition of the CdSe layer, the emission was found to have quenched even further, thereby suggesting that the bi-sensitization process further improved upon electron transfer, thereby accounting for the higher power conversion efficiency value observed. In effect, within a bi-sensitized ZnO photoelectrode, electron transfer occurred towards the lower conduction band of ZnO while hole transfer emanated from the valence band from ZnO to CdS and onwards to CdSe.

With respect to pure ZnO/CdSe QD heterostructures alone, first created using a linker-assisted assembly (LAA) method,¹⁶³ these composites incorporated within a solar cell configuration¹⁶⁴ achieved internal quantum efficiencies of 50-60% and a power conversion efficiency of 0.4%, when using mercaptopropionic acid (MPA) as the ligand. Comparable solar cells generated using heterostructures, incorporating thioglycolic acid (TGA) as the capping ligand on the CdSe QDs,¹⁶⁵ yielded a power conversion efficiency value of 0.66%. This increase in PEC was attributed to the shorter chain length of TGA, which allowed for faster charge transfer. With respect to data on the photocatalytic activity of these 1D ZnO/CdSe QD heterostructures,¹⁶⁶ the presence of a shorter ligand linker chain also corroborates the idea of a more efficient charge transfer process within these composites. On analogous composite architectures created from ZnO 1D nanorods decorated with CdSe/ZnS core/shell QDs, the acquired results showed that the core-shell motif led to a less effective photocatalytic ability, not

only because the ZnS shell layer served as a barrier to electron transport but also because the conduction band of CdSe was lower than that of ZnS, denoting data highlighting the primary importance of charge transfer in governing the observed performance of these heterostructures.

Based on all of these cumulative results, it is evident that co-sensitization of 1D ZnO with both individual CdS and CdSe QD species is more relevant for increasing efficiency as opposed to manipulating the linker chemistry itself. As such, solar cells incorporating ZnO nanowires co-sensitized with CdS and CdSe QDs with a ZnS passivation layer¹⁶⁷ demonstrated initial power conversion efficiency values of 1.33%, which was a tangible improvement as compared with data for 1D ZnO sensitized with either CdS or CdSe QDs alone.^{162, 165} It is also worth mentioning that the ZnS passivation layer performed differently as compared with a ZnS shell layer, which, as we noted earlier in a previous example, served to hinder hole transfer from ZnO to the adjacent QDs. In this case, the ZnS passivation layer, deposited onto ZnO/CdS/CdSe photoelectrode, was able to protect the QD from photocorrosion, and operated as a means for enabling hole transfer toward the electrode through bandgap level engineering considerations. In effect, optimizing the thickness of the ZnS passivation layer led to power conversion efficiencies of up to 2.03%.¹⁶⁸ To accentuate the equally significant role of the fabrication procedure itself, it was found that an in-situ sequential assembly process of both ionic layer adsorption and reaction (ILAR) and chemical bath deposition (CBD) to create the requisite heterostructures composed of ZnO nanowires sensitized with both CdS and CdSe QDs with a passivating layer of ZnS led to power conversion efficiencies of 2.68%.¹⁶⁹ Recent work has also focused on the deposition of electronically more complex, as-formed CdS/CdSe core/shell QDs onto ZnO nanowires.¹⁷⁰

Beyond the use of CdS and CdSe QDs alone, additional QD species, such as PbS and ZnS, have also been deposited onto 1D ZnO nanostructures. As representative examples, 1D/0D

QD-based solar cells encapsulating ZnO/PbS,¹⁷¹⁻¹⁷³ ZnO /ZnSe,¹⁷⁴ and ZnO/PbSe heterostructures¹⁷⁵ have been reported, though the associated PCE values varied in magnitude. One of the best performance metrics recorded was for the QDSSC incorporating the ZnO/PbS composite with a measured PCE of 6.87%. It is also worth noting that a CdTe QD monolayer sensitized ZnO nanowire array has been generated as an efficient photoelectrode for water splitting with 200% higher maximum PCE values as compared with that of ZnO alone.¹⁷⁶ In addition, ZnO/PbS QD heterojunction-based solar cells have been found to be effective in the near-IR region with ultra-high IPCE values measured at 58% (@ 1020 nm).¹⁷⁷ Overall, these results reveal the important role of proper band gap alignment of constituent materials for initiating the desired charge transfer.

4.1.4. TiO₂: Solar and Photocatalytic-based Applications

Titanium oxide (titania: TiO₂) is a wide bandgap material (3.0-3.2 eV), which exists as either crystalline anatase, rutile, or brookite. These materials have been utilized as components of applications including but not limited to batteries, photovoltaic cells, advanced photocatalysts for environmental purification, pigments, cosmetics, photonics, optoelectronic devices, and gas sensors, partly due to their low cost, chemical stability, and robustness under UV illumination. Coupled with quantum dots of varying chemical compositions, such as CdSe, CdS, CdTe, and PbSe as illustrative examples, it is conceivable to create an ‘adjustable’ heterostructure, wherein in principle, the degree of charge separation under visible light excitation can be tunably and systematically controlled by reaction variables, a theme we have previously investigated in the context of carbon nanotubes.

As we have seen previously, size matters. For example, when CdSe QDs of varying, controlled diameters (i.e., 2.3 nm, 2.6 nm, 3.0 nm, and 3.7 nm) were immobilized onto TiO₂, it

was evident that smaller-sized CdSe QDs evinced greater charge injection rates and also higher IPCE values (i.e. 36%) at the excitonic band. By contrast, larger QDs gave rise to an improved absorption profile in the visible region but were less efficient at injecting electrons into TiO₂.

Morphology makes a difference. Specifically, the use of a hollow 1D tubular structure as opposed to a 0D nanoparticle as an underlying scaffold affords heterostructures which generate higher maximum IPCE values within solar cell configurations.³² Specifically, in moving beyond the use of 0D TiO₂ nanoparticle films to 1D TiO₂ nanotube arrays, the IPCE readings of the corresponding CdSe QD-based heterostructures improved from 26% to 55%.¹⁷⁸ In addition, CdSe QD-sensitized 1D porous TiO₂ nanofibers, employed within a solar cell, achieved PCE values of up to 2.15% as compared with 1.50% for bare TiO₂ nanofibers¹⁷⁹ Not surprisingly, CdSe QD-sensitized TiO₂ nanotube arrays photocatalytically outperformed those of conventional nanoparticles in degrading methyl orange at values of up to 88.20% in 2 h.¹⁸⁰ Though these collective data from different papers are not directly comparable, they do also highlight the likely and related significance of QD surface loadings upon the observed metrics measured.

The attachment chemistry is another important variable. With respect to the photocatalytic activity of CdS QD-sensitized TiO₂ nanotube arrays,¹⁸¹ the effect of the attachment method (i.e. the use of chemical bath deposition versus sonochemistry to deposit QDs) on the resulting performance of the heterostructures was analyzed. Heterostructures created using the sonochemical method gave rise to superior photocatalytic activity in terms of being able to degrade 61.4% of methyl orange dye within 180 min. By contrast, the corresponding values for samples prepared with the chemical bath deposition method and for bare TiO₂ nanotube array controls were 53.0% and 4.2%, respectively. Other groups have also probed the rates of

photodegradation of dyes using TiO₂/CdS heterostructures,¹⁸²⁻¹⁸⁴ with the highest observed degradation of methyl orange reported to be as much as 98.83% after 3 cycles of activity.¹⁸⁵

As was observed with ZnO, co-sensitization of 1D TiO₂ nanostructures with both CdS and CdSe QDs gave rise to an evidently better photoelectrochemical performance than either TiO₂/CdS or TiO₂/CdSe composites alone.¹⁸⁶ As an added nuance to the previous studies on co-sensitization, if the sequence of QD addition were manipulated, it was found that the performance of the heterostructures was enhanced when CdS QDs were initially deposited onto the TiO₂ nanotubes followed by the subsequent combination with CdSe QDs. This apparent difference in performance can be rationalized on the basis of the band gaps of the three individual constituent components. In effect, because the band gap between the conduction and the valence band of CdS is closer to that of TiO₂, charge transfer is more efficient within a CdS-TiO₂ interface as opposed to a CdSe-TiO₂ interface. In effect, the overall positioning of energy levels suggests that CdSe could block charge transfer towards CdS, if the sequence of QD addition had been reversed. Nonetheless, co-sensitization with both types of QDs was found to further enhance the observed charge transfer. Not surprisingly, TiO₂/CdS/CdSe structures have been used to fabricate solar cells with measured power conversion efficiencies of 2.52%.¹⁸⁷

A different group showed TiO₂/CdS/CdSe composites could be used for hydrogen generation at a rate of as much as 10.24 μmol h⁻¹ cm⁻².¹⁸⁸ Interestingly, the spatial distribution of these CdS and CdSe QD species can also be precisely controlled. Indeed, an unusual tandem heterostructure configuration, grown onto FTO, consisting of TiO₂ nanotubes onto which CdS QDs had been controllably deposited on one side while CdSe QDs had been immobilized on their opposite side¹⁸⁹ yielded a solar-to-hydrogen conversion efficiency of 2.78%, which was

greater than that achieved by mixed CdS/CdSe QD-co-sensitized TiO₂ nanotubes without such a degree of spatial manipulation.

Beyond CdS and CdSe QDs, heterostructures incorporating CdTe, PbS, and PbSe have also been created and probed for a variety of optical applications. For example, composites generated from CdTe QDs deposited onto TiO₂ nanotube arrays could give rise to a photocurrent density of as high as 6 mA cm⁻², which is about 35 times higher than that for bare TiO₂ nanotubes alone. Additional studies were able to increase the observed photocurrent density of 1D TiO₂/CdTe QD heterostructures to 15.83 mA cm⁻² with a corresponding PCE of 7.9%.¹⁹⁰ In terms of photocatalysis, the oxidative decomposition of *p*-nitrophenol (PNP) was analyzed using CdTe QD-sensitized TiO₂ nanotube arrays with the finding that PNP photodegradation could be induced in as little as 2 h.¹⁹¹ The quenching of the PbSe bandgap emission within PbSe QD-sensitized TiO₂ nanorods fabricated by a hot-injection method demonstrated the possibility of a rapid 2.1 ns transfer of photoinduced carriers into the TiO₂ domain.¹⁹² As such, in terms of taking advantage of this interesting photophysics, PbSe QD-sensitized TiO₂ nanotube arrays have shown to photocatalytically degrade methyl orange by as much as 90% in 6 h;¹⁹³ TiO₂ nanotubes sensitized with PbSe QDs can generate hydrogen with power conversion efficiencies of up to 10.6%;¹⁹⁴ and finally, 1D TiO₂/PbS QD heterostructures can yield power conversion efficiencies of 1.9%, a value which is 40 times higher than that for bare TiO₂ alone.¹⁹⁵

4.1.5. Examples of Other Metal Oxide-based Heterostructure Systems

As implied earlier, we have discussed major, relevant examples of binary metal oxide-based 1D-0D heterostructures, incorporating TiO₂, SnO₂, ZnO, and CeO₂. Additional examples exist. For brevity, we highlight a few more instances so as to illustrate the breadth of work on

these types of structures, including Fe_2O_3 and a combined ZnO/TiO_2 metal oxide conjugate, which are conceptual extensions of the cases we have previously described.

$\alpha\text{-Fe}_2\text{O}_3$ hematite nanowires have been combined with PbSe QDs using an interesting epitaxial synthesis method, based on an initial dehydration procedure under ultra high vacuum conditions at high temperature following by a hot-injection process to induce QD nucleation.¹⁹⁶ The resulting heterostructure consisted of PbSe QDs immobilized onto 100 nm hematite nanowires such that the PbSe (002) and Fe_2O_3 (003) facets overlaid upon each other, along the [1-10] crystallographic direction of the wire. It was noted that longer dehydration times increased the QD coverage density and narrowed the QD diameter distribution, whereas lower injection temperatures decreased both the observed QD diameter and diameter distribution. It was postulated that other types of QDs including but not limited to CdSe and CdS could be similarly attached onto other binary metal oxide 1D structures with implications for bandgap alignment matching relevant for solar cell and/or water splitting applications.

ZnO/TiO_2 conjugate structures consisting of a thin TiO_2 passivation layer deposited onto the exterior surface of a ZnO nanorod array served as the platform for the subsequent accretion of a *p*-type CdTe shell to create a final composite with a PCE of 1.44%.¹⁹⁷ The TiO_2 thin layer ranged from 0.5 nm to 4 nm to effectively ‘neutralize’ the surface defects of the ZnO nanorods.

4.2. Complex Metal Oxide-based Heterostructures

4.2.1. Orthophosphate-based Heterostructures

- **CePO₄: Initial Proof of Principle - Idea of structure & chemical composition controlling charge vs. energy transfer channels.**

Tb-doped CePO_4 nanostructures have been extensively used as a green emitting material in fluorescent lamps, and have also been considered for optoelectronics as well as for biological

labeling applications.¹⁹⁸⁻²⁰⁰ Our motivation for the initial study in this area was to create a model semiconducting and luminescent 0D QD - 1D metal oxide architecture.⁸³ Specifically, we generated crystalline Tb³⁺ doped, high-aspect ratio 1D CePO₄ nanowires through a ‘biomineralization’ process that our group has developed and refined over the years. In parallel, we prepared 0D CdSe QDs coated with AET ligands, wherein the thiol groups were bound onto the CdSe surface. We successfully anchored the 0D CdSe QDs onto the external sidewalls of the 1D nanowires via hydrogen bonding interactions between the AET linkers and H₂O molecules that had intercalated within the CePO₄ structure. The as-generated 0D CdSe QD-1D CePO₄: Tb³⁺ nanowire-based heterostructures were characterized by HRTEM and TEM analysis (Figure 5A).

Due to their lower photobleaching capability, comparatively high quantum yields (up to 60%), good chemical stability, and relatively low toxicity,^{201, 202} metal ion-doped lanthanide orthophosphates represent an optically attractive class of metal oxides. Not surprisingly, Tb-doped CdPO₄ nanostructures have been incorporated as viable components of different kinds of device applications including but not limited to fluorescent lamps, optoelectronics, and biological labeling.^{199, 200} Within our studies, we characterized the optical absorption, luminescence behavior, and lifetimes of our CdSe QD-CePO₄: Tb³⁺ nanoscale heterostructures. In Figure 5C and 5D, we noted a perceptible PL quenching effect of our QDs at different excitation wavelengths as compared with unbound CdSe QDs and free CePO₄: Tb nanowires. Moreover, in terms of deducing structure-property correlations, we systematically varied the concentration ratios of CdSe QDs to CePO₄: Tb³⁺ from 3:1 to 3:2 to 1:1, and found that the degree of quenching within the heterostructures correlated with the relevant amounts of these two constituent components. Specifically, not only did the observed lifetimes shorten but also the amount of PL quenching of the CdSe increased proportionately with higher QD coverages

immobilized onto the underlying phosphate templates. We also showed the relative band gap alignments of all of the constituent units within the heterostructure in Figure 55B.

From this picture, we were able to prove that not only is photo-induced charge transfer possible within novel luminescent CdSe semiconducting quantum dots (QDs) and CePO₄: Tb³⁺ metal oxide nanowire heterostructures but also the direction of that charge transfer activity can be controlled by the magnitude of the irradiation energy used. Specifically, under near-UV-to-visible excitation, hole transfer from the valence band (VB) of the CdSe QDs to the conduction band (CB) of the CePO₄: Tb³⁺ nanowires was responsible for the reduction in the CdSe QD signal, whereas under deep UV irradiation, electron transfer from CePO₄:Tb³⁺ to CdSe QDs was posited as accounting for the observed quenching of the CePO₄:Tb³⁺ emission peaks (Figure 5B). These dual effects were more pronounced with higher coverages of CdSe QDs immobilized onto and therefore interacting with the underlying CePO₄: Tb³⁺ nanowire motif.^{83, 198}

- **LaPO₄: Effect of morphology, surface coverage, and dopants on optical properties.**

Rare earth doped LaPO₄ has not only been considered as an emitting material in fluorescent lamps but also has also been used within optoelectronics,²⁰³⁻²⁰⁵ due to its lower photo-bleaching capability, relatively high quantum yields (up to 90% at deep UV excitation), reasonable chemical stability, and fairly low toxicity. Our objectives in creating QD-based heterostructures, derived from these phosphates, were manifold.²⁰⁶

(a) First, from the *synthesis* perspective, we proposed a novel route with respect to generating a three-dimensional (3D), rare-earth-doped LaPO₄ submicron urchin-like structure. This synthesis technique was distinctive, because it incorporated a relatively facile, template-free, ambient, large-scale, and aqueous solution-directed protocol. The morphology of the as-prepared 3D phosphates is shown in Figure 6A. The ‘sea-urchin’-like structures possessed an apparent

overall diameter of ~ 500 nm and consisted of numerous constituent nanowires concentrically projecting out from a central core, like spokes of a wheel. (Figure 6A).

(b) Second, we analyzed the *growth mechanism* of our 3D sub-micron LaPO_4 -based architectures in fairly rigorous detail through a meticulous and thorough time-dependent scanning electron microscopy (SEM) visualization analysis. We found that isolated sizes of our hierarchical assemblies correlated proportionately with higher La/P molar elemental ratios (i.e. a measure of the chemical potential) and longer reaction times. In parallel, we prepared larger 1D nanowires (Figure 6B) with controlled diameters using a hydrothermal-based technique.

(c) Third, to test the role of morphology upon the optical properties of the resulting heterostructures, we attached semiconducting CdSe QDs onto these two different motifs of lanthanum phosphate to create *a unique and novel family of 0D CdSe QD - 1D/3D rare earth doped LaPO_4 heterostructures*. In so doing, our objective was to couple and take advantage of the intrinsically interesting optoelectronic properties of each of these nanomaterial components.

(d) Fourth, in terms of gaining a fundamental understanding of the optical behavior of our QD- LaPO_4 systems, we collected and subsequently interpreted a series of optical absorption and luminescence (i.e. emission) data (including lifetime measurements) on these CdSe QD- LaPO_4 heterostructures. We studied these phenomena as a function of (i) morphology, (ii) QD coverage density, and (iii) the presence of LaPO_4 dopants (i.e. Ce, Eu, and Tb).

Specifically, our results demonstrated that heterostructures attached with CdSe QDs yielded significant PL quenching and shorter average lifetimes as compared with pristine LaPO_4 . Nevertheless, in terms of a *distinctive morphological effect*, we found that under both 380 nm and 260 nm excitation, the CdSe QD-3D LaPO_4 : Eu heterostructures exhibited much less PL quenching and longer lifetimes as compared with their 1D counterparts (as noted by comparing

Figure 6C and E with Figure 6D and F). This assertion was ascribed to the observation that the 3D heterostructures possessed a nearly 3 times higher coverage density of CdSe QDs attached onto their surfaces as compared with their 1D analogues. As such, the presence of these additional QDs resulted in a more effective absorption of the LaPO₄: Eu³⁺ emission. Figure 6G highlights the relative band gap alignments of the species involved, and supports the idea that the observed PL quenching is most likely due to a photo-induced charge transfer from CdSe QDs to LaPO₄ through the mediation of water molecules coating the surfaces of LaPO₄.

Moreover, the *identity of the rare-earth dopant ion* used could also largely influence the magnitude of the PL signal and the corresponding lifetimes measured within the CdSe QD (0D)–LaPO₄ (1D/3D) heterostructures. Specifically, after doping with Eu, the PL intensity increased as compared with the undoped heterostructure, as is evident in Figures 6C and D for both 1D and 3D morphologies. From the band gap alignment picture, it is reasonable to suggest that charge transfer from CdSe QDs to LaPO₄: Eu³⁺ and a corresponding energy transfer from LaPO₄: Eu³⁺ to CdSe QDs are both feasible processes within this heterostructure motif. Moreover, heterostructures based on the 3D morphology seemed to be more efficient than their 1D counterparts for both of these charge and energy transfer processes.

In essence, the observed optical behavior was reflective of the band gap alignments of the various lanthanide ion participant species relative to that of CdSe itself. For example, with Ce³⁺, under the excitation of near UV–visible light illumination (i.e. 380 nm), photoexcited electrons from the VB of the QDs can flow into the corresponding VB of LaPO₄: Ce³⁺ in a non-radiative fashion, prior to their recombination with photogenerated electrons in the QDs. This scenario would explain the PL quenching shown in Figure 6H. Conversely, under the excitation of deep UV light irradiation (i.e. 260 nm), the CB levels of the Ce dopant ions are higher in energy than

the corresponding CB levels of CdSe QDs, implying that photoexcited electrons can migrate from Ce^{3+} to CdSe, thereby accounting for the evident reduction of the inherent PL emission signal of Ce^{3+} incorporated as part of LaPO_4 . By contrast, the positions of the VB levels of both Eu^{3+} (at -9.0 eV) and Tb^{3+} (at -7.7 eV) within LaPO_4 were located below that of CdSe QDs (-6.1 eV) themselves. Hence, we would not necessarily expect charge transfer from CdSe QDs to occur to either Eu^{3+} or Tb^{3+} ions, as this process would be nominally forbidden.

However, depending on the incident irradiation, either charge or energy transfer from Eu^{3+} and Tb^{3+} ions to CdSe QDs was possible, because the corresponding CB levels of Tb^{3+} and Eu^{3+} were located at a higher energy than that of CdSe QDs. Hence, due to a more pronounced spectral overlap of its emission band with the absorption profile of CdSe QDs, Tb-doped 3D-urchin-based heterostructures displayed both a higher PL intensity and a longer lifetime as compared with analogous Ce and Eu-activated heterostructures (Figure 6H and I).²⁰⁶

In terms of a different example of an orthophosphate motif immobilized with QDs, BiVO_4 QDs have been attached onto BiPO_4 nanorods to generate 0D/1D heterojunctions as visible-light-driven photocatalysts. The resulting Rhodamine B dye degradation activity of the composite heterostructure was 8.3 times and 6.3 times faster than that of pristine BiPO_4 and BiVO_4 constituent components, respectively.²⁰⁷

4.2.2. Tungstate-Based Heterostructures

- **CaWO₄: Deliberative band gap alignment between acceptors and donors – Concept of optical behavior mediated by ligands and morphology.**

CaWO_4 is known as a ‘self-activated’ luminescent material, whose optical properties (i.e. an intrinsic luminescence unrelated to any external doping) are defined and determined to a large degree by its inherent structural properties. In our initial efforts,²⁰⁸ we constructed a potentially

optically significant class of distinctive heterostructures purposely incorporating not only 1D/0D self-activating metal oxide luminescent materials but also 0D semiconducting CdSe QDs, via electrostatic interactions mediated by the presence of a 3-mercaptopropionic acid (MPA) linking agent. Our composite materials were structurally characterized by TEM (Figure 7A and B).

The actual occurrence and corresponding efficiency of charge transfer between the component constituent subunits could be tuned not only by alteration of (i) the QD coverage density onto CaWO_4 but also by modification of (ii) the crystallite size of the CaWO_4 itself. We highlight that there were no dopants at all within our tungstate system.

In so doing, we demonstrated the synthetic ability to use the chemistry and structure of these 2 constituent components to selectively alternate between and/or favor either energy or charge transfer processes or a combination of the two. Specifically, our results demonstrated that both of our 1D and 0D heterostructures evinced not only a notable PL quenching but also shorter lifetimes of the CaWO_4 signal upon attachment with CdSe QDs, especially as compared with the unbound CaWO_4 , with the relevant data shown in Figure 7C. Upon analyzing the relative band gap alignments of the various species shown in Figure 7D, we were able to ascribe this collective PL behavior to charge transfer between CaWO_4 and the adjoining CdSe QDs, a scenario corroborated by complementary NEXAFS data (Figure 7E). In effect, the CB position of CaWO_4 is much higher than that of the corresponding CB levels of not only the MPA linker as but also the CdSe QDs. As such, it is likely that electron transfer occurred from CaWO_4 to CdSe QDs in a process facilitated by the presence of the MPA linker. Conversely, we would expect complementary photoinduced holes to be presumably trapped by the ligand as opposed to flowing freely back to the metal oxides, because of the relatively low VB position of CaWO_4 relative to that of either the CdSe QDs or the MPA linker (Figure 7D).

In terms of highlighting the importance of QD coverage and CaWO_4 crystallite size, we noted that the PL quenching of heterostructures incorporating 0D CaWO_4 (despite its lower coverage) was surprisingly greater as compared with the analogous 1D CaWO_4 . This unexpected observation was attributed to the inherently larger crystallite size of 0D CaWO_4 which would have given rise not only to an intrinsically higher PL output and a PL QY, associated with the production of more photoinduced charge carriers, but also to the larger PL quenching effect noted upon coupling with adjoining CdSe QDs.²⁰⁸ As such, understanding and clearly delineating charge and energy transfer processes within our model CaWO_4 - CdSe QD heterostructures were key to fundamentally understanding the optoelectronic behavior of nanoscale interfaces.

- **CaMoO_4 - CaWO_4 : Roles of QD identity and Metal Oxide Composition.**

Scheelite materials associated with the family of tungstate and molybdate compounds are widely used as components of phosphors,²⁰⁹ scintillation detectors,²¹⁰ gas sensors,²¹¹ optical fibers,²¹² laser materials,²¹³ amplifiers,²¹⁴ and photocatalysts.²¹⁵ In our study,²¹⁶ we sought to fundamentally *understand how controlled alterations in the chemical composition* would enable *corresponding insights into relevant structure-property (in this case, optical) correlations*.

As such, we not only created stable, crystalline, and stoichiometrically pure solid solution mixtures of Eu^{3+} -activated CaWO_4 and CaMoO_4 scheelites within the structural context of a unique 1D motif but also systematically varied the relative amounts of tungstate and molybdate in a controlled and deterministic manner. Specifically, the synthesis was initiated using our U-tube protocol to produce 1D $\text{CaW}_{1-x}\text{Mo}_x\text{O}_4$: Eu^{3+} with 'x' varying in quantity from 0, 0.2, 0.4, 0.6, 0.8, to 1. The idea herein was to modulate optical behavior by tuning interactions among the emission centers associated with the constituent and discrete molybdate and tungstate subunits. Not surprisingly, under excitation at both 280 nm and 395 nm, we found that the peak located

near 270-290 nm, which was attributable to the presence of charge transfer between the oxygen and either the tungsten or molybdenum atoms within the anion complex of WO_4^{2-} or MoO_4^{2-} , generally red-shifted with increasing 'x' within the series of $\text{CaW}_{1-x}\text{Mo}_x\text{O}_4: \text{Eu}^{3+}$. This observation not only was consistent with the formation of a homogeneous, uniform, and 'ideal' solid solution with the presence of little if any impurities (Figure 8A) but also supported the notion of a clear composition-dependent optical behavior. Indeed, the highest emission intensity was observed when 'x' = 0.8 (Figure 8B).

Subsequently, to take advantage of the inherently intriguing optoelectronic properties of the constituent 'precursor' nanomaterials, we generated new classes of more complex heterostructures by attaching and immobilizing different types of 0D chalcogenide QDs (i.e. CdSe and CdS) onto the surfaces of 1D Eu^{3+} -activated CaWO_4 - CaMoO_4 metal oxides through the mediation of organic small-molecule MPA ligands as a connecting linker. Associated HRTEM and TEM images are presented in Figure 8C and D. Because we measured the highest PL intensity with $\text{CaW}_{0.2}\text{Mo}_{0.8}\text{O}_4$ (i.e. 'x' = 0.8), not surprisingly, we discovered the largest amount of PL quenching within the PL emission spectra with 1D $\text{CaW}_{0.2}\text{Mo}_{0.8}\text{O}_4: \text{Eu}$ nanowire – QD heterostructures. These data could be rationalized as originating from favorable photoexcited charge transfer from the underlying metal oxide host lattice to the immobilized QDs. Importantly, our work emphasized the importance of the *QD identity* itself, as we reported on a measurably more significant quenching of $\text{CaW}_{0.2}\text{Mo}_{0.8}\text{O}_4$ with adjoining CdSe QDs as opposed to CdS QDs (Figure 8F). We can account for this behavior in part to the larger CB band offset between $\text{CaW}_{0.2}\text{Mo}_{0.8}\text{O}_4: \text{Eu}^{3+}$ and CdSe QDs (a difference of ~ 2.2 eV) as compared with that between the corresponding $\text{CaW}_{0.2}\text{Mo}_{0.8}\text{O}_4: \text{Eu}^{3+}$ and CdS QDs (a gap of ~ 1.4 eV). Hence, it was more

advantageous and more favorable for charge transfer to occur from the mixed metal oxides to the attached CdSe (instead of CdS) QDs (Figure 8D).²¹⁶

● **Heterostructures incorporating other tungstates with CdS**

Heterostructures consisting of hydrothermally generated ZnWO₄ nanowires and CdS QDs have also been produced.²¹⁷ The as-prepared ZnWO₄ measured about 20 nm in diameter and 100 nm in length, whereas the CdS QDs had an average diameter of ~5 nm. When applied for ciprofloxacin degradation under visible light irradiation, it was noted that electron transfer from the conduction band of CdS to the corresponding conduction band of ZnWO₄ promoted exciton formation. Moreover, this composite evinced not only increased photo-activity but also improved photo-stability as compared with controls, in agreement with a parallel study.²¹⁸

With the analogous CdS-decorated CdWO₄-based heterostructures,²¹⁹ the effect of varying the structural CdWO₄ motif was probed. Specifically, pure nanowire arrays measuring ~10 – 50 nm in diameter and 8 microns in thickness and 3D flower-like micron-scale hierarchical assemblies composed of constituent 200 – 600 nm nanorods of CdWO₄ gave rise to photocurrents of 0.35 mA/cm² and 0.11 mA/cm², respectively. Upon the addition of CdS QDs, the resulting heterostructure yielded a higher absorption of visible light and greater exciton generation as compared with pristine CdWO₄ alone. In particular, the CdS 0D – CdWO₄ 1D nanowire heterostructure yielded a photocurrent of 0.66 mA/cm², which is 20% larger than that of the pristine CdWO₄ alone.

4.2.3. Other Types of Complex Metal Oxide-based Heterostructures

● **β -Pb_{0.33}V₂O₅ - Tunable interfacial energy offsets**

As highlighted with QDs attached onto carbon nanotubes, the nature of the attachment protocol creating the heterostructures interface has a major effect upon the observed charge

transfer. In the case of heterostructures created from CdSe QDs immobilized onto β - $\text{Pb}_{0.33}\text{V}_2\text{O}_5$ nanowires, composites were produced by not only a linker (i.e. cysteine) - assisted assembly method but also through a successive ionic layer adsorption and reaction (SILAR) protocol (Figure 9A, B). In the SILAR route, successive precipitation cycles could be used to tune and alter CdSe QD surface coverage. The degree of transfer of photogenerated holes from the valence bands of the CdSe QDs to the mid-gap states of β - $\text{Pb}_{0.33}\text{V}_2\text{O}_5$ nanowires could be tailored by variation of not only cation stoichiometry but also particle size, denoting a set of novel means for modulating the driving force for enabling charge transfer (Figure 9C, D), i.e. the overlap between the valence band of the CdSe QD and the midgap state of the adjoining β - $\text{Pb}_x\text{V}_2\text{O}_5$. PL measurements (Figure 9C) also provided evidence for interfacial hole transfer from CdSe QDs to the β - $\text{Pb}_x\text{V}_2\text{O}_5$. To be specific, whereas ‘free’ CdSe QDs possessed average lifetimes of 26 ± 1 ns, within heterostructures, that value reduced to 16.6 ± 0.2 ns, a finding indicative of faster charge transfer within the heterostructure. In effect, this study revealed excellent model systems for facilitating both efficient light harvesting and effective interfacial charge transfer for solar energy conversion.²²⁰

● **Silicate/Silica-based heterostructures with tunable optical emission**

As a viable phosphor, the observed color emission of wide-bandgap Zn_2SiO_4 can be tuned by the nature and amount of dopant integrated into it. Specifically, Mn-doped zinc silicate ($\text{Zn}_2\text{SiO}_4: \text{Mn}^{2+}$) has been incorporated as a key element of fluorescent lamps, neon discharge lamps, oscilloscopes, black-and-white televisions, color televisions, and many other displays and lighting devices,²²¹ respectively, due to its long lifetime, which is of significant importance in minimizing the degree of flicker within displays.²²² In our study,²²³ we systematically varied the Mn dopant quantity from 0 to 8% so as to control the corresponding Mn^{2+} emission peak

behavior. With respect to the optical properties of the corresponding CdSe QD - Mn: Zn₂SiO₄ heterostructures, we noted simultaneous energy transfer and charge transfer phenomena between the two constituent components. Specifically, upon photo-excitation, energy transfer likely occurred from the dopant Mn²⁺ species to CdSe QDs, whereas electron transfer went in the opposite direction from the CdSe QDs to the dopant Mn²⁺ ions. Upon excitation of the CdSe QDs alone, probable charge transfer emanated from the CdSe QDs to the adjoining Mn²⁺.²²³

Silica is relatively nontoxic, and its thickness can be tuned with nanometer precision.²²⁴ Moreover, silica contains free silanol groups that can be subsequently reacted with additional, appropriate functional groups through relevant silanization reactions.^{225, 226} QD-doped silica tubes have been synthesized by adding in QDs into a sodium silicate solution, and were subsequently processed so as to form QD-doped glass fibers. The resulting heterostructures characterized by a concentrated but well dispersed loading of QD exhibited reasonable near IR emission with potential for use as a component of a viable microfluidic system.²²⁷ An analogous composite structure, composed of PbS QD-doped glass fibers,²²⁸ was generated by crystallization of 2 nm QDs within a host glass matrix at 390°C for 5 h. Changing the QD size by processing at different melting temperatures yielded heterostructures with correspondingly variable near IR emission properties and lifetimes.

5. Metal Chalcogenide-based Heterostructures

5.1. Binary Metal Chalcogenide-based Heterostructures

5.1.1. 0D QD – 1D nanorod structures: quasi core/shell dot-in-rod (DIR) structures

The DIR composite is a semiconducting quasi type-II structure, wherein the energy levels of the conduction band and the valence band of the core and shell materials are offset from each

other. As such, electrons and holes readily separate. The holes are confined to the CdSe QD core, whereas electrons are localized within the CdS shell.²²⁹⁻²³³ Not surprisingly, 1D/0D DIR heterostructures denote excellent candidates as viable components of representative devices, such as photodetectors, LEDs, and lasers. Moreover, different types of metal chalcogenide-based DIR heterostructures have also been reported, including but not limited to CdSe/CdS,^{229, 231-234} ZnSe/CdS,²³⁵ Cu₂Se/Cu₂S,²³⁶ ZnSe/ZnS,²³⁷ and PbSe/PbS.²³⁶

In essence, the DIR motif resembles a ‘core/shell structure’ and is another example of the role and importance of morphology as a means of controlling observed performance. Specifically, DIR structures can be grown by coating 1D rod like shells of CdS around CdSe 0D quantum dot cores.²³⁴ In effect, the aspect ratio of CdS can be tuned continuously, while keeping the size of the CdSe QDs constant. The maximum electron-hole separation quantum efficiency was found to be 70-75% with rods possessing an aspect ratio of 1.6 to 2. An increase in aspect ratio correlated with a decrease in the oscillator strength per unit volume, thereby leading to a steady reduction in the measured fluorescence decay and a corresponding red shift to longer wavelengths for both PL and absorption spectra.

Moreover, as added refinements to this concept, photon-to-electron quantum efficiencies for various core-shell structure configurations incorporating CdSe and CdS have been comparatively reported, including those of (a) quantum dots attached onto CdS rods, (b) a traditional spherical core-shell CdSe/CdS architecture, and (c) CdS/CdSe DIR structures (Figure 10B, C), respectively, for hydrogen generation. In these sets of experiments, the chemical composition, size, and shape of the constituent components of these nanoscale heterostructures were systematically varied, and the structural modifications were correlated with the resulting photoluminescence data, a measure of the effectiveness of hole trapping efficiency.

Indeed, the DIR system evinced enhanced absorption and photoluminescence profiles that were a unique and cumulative function of individual CdS rods and CdSe seeds coupled with additional absorption transitions, originating from the interaction of both of these separate chalcogenide components (Figure 10D). As such, this DIR architecture evinced photon-to-electron quantum yields of as high as 98%, designating a far superior value to that of any of the other structures tested (Figure 10A, C). Because all of these DIR structures possess basically identical conduction and valence band alignment, the observed differences in performance can likely be ascribed to morphology considerations. When these heterostructures were subsequently coupled with a Pt catalyst, floating free in solution, the measured internal quantum yield for the reduction of water to hydrogen was 13.6%, whereas the external quantum yield was 7.5%, all of which were promising in nature.²³⁸ Not surprisingly, analogous motifs of this CdSe/CdS DIR heterostructure have been produced, encompassing disparate species such as either Pt tips^{238, 239} or different classes of electron donors and acceptors²⁴⁰ to improve upon H₂ production efficiency.

5.1.2. Complex 0D QD - 1D - 0D QD Chalcogenide-based DIR Heterostructures

As an extension of the DIR quasi-core/shell idea, 0D-1D-0D ‘bar-bell’ heterojunctions, incorporating QDs (identical or different) as caps at either the end of a 1D rod structure, have been formed. For example, linear CdTe/CdSe/CdTe heterostructure nanorods have been synthesized via a single-pot, high-temperature colloidal synthesis (Figure 10E). Because of the limited interfacial area between the CdSe and CdTe domains, the optical properties of the linear heterostructures were noted to be qualitatively different from their individual constituent components. In particular, exciton formation initially occurred within the central CdSe region with holes possibly tunneling into one of the CdTe end caps, thereby giving rise to a lower energy emission peak, indicative of type II recombination. Moreover, the photoluminescence

intensity of these materials increased with decreasing temperature (down to 5 K), while the peaks themselves simultaneously narrowed and shifted to higher energy, an observation ascribable to lattice contraction as the heterostructures cooled.²⁴¹ It is also worth noting that the interface between CdTe and CdSe is quite distinctive, partly because the difference in the lattice spacing of these two materials may lead to significant physical strain at the interface which itself can impact upon the resulting charge transfer and separation. Additional work on this system^{242, 243} corroborated the idea that the energy and lifetime of the charge-transfer photoluminescence band could be tuned by changing the relative alignment of band edges within these heterostructures.

Analogous families of ZnSe/CdS/ZnSe heterostructures were initially synthesized through a solution-phase synthesis method,²⁴⁴ and yielded a robust photoluminescence emission signal at 583 nm. Interestingly, charge transfer within this system was not hindered by the strain of overgrown quantum dot caps, due to the low lattice mismatch between ZnSe and CdS of ~2.5%. As such the photoluminescence peak for the nanoscale ‘bar-bells’ was much more intense than that for CdS nanorods alone, due to a staggered band gap alignment between the two nanoscale components. In other words, these heterostructures represented true ‘type II’ structures in that (i) the crystal domains for both constituent materials were distinct and separate and (ii) moreover, the conduction and valence bands of CdS were lower in energy than those of ZnSe, implying that holes were confined to ZnSe with electrons localized onto CdS. As expected, additional absorption features appeared at lower energies than that of the bandgap of either ZnS or CdS nanocrystals. Upon probing these heterostructures using transient absorption spectroscopy, it was noted that the photoinduced charge transfer between the two nanocrystalline domains could be controlled by changing the excitation wavelength, i.e. the excitation energy. Specifically, the resonant excitation of carriers within ZnSe led to electron injection into CdS on

a time scale of 350 fs, whereas carrier excitation within CdS resulted in a slower transfer of holes into ZnSe at a corresponding time scale of 95 ps. That is, with resonant excitation of ZnSe tips, it is expected that there will be an ultrafast transfer of excited carriers into the CdS domain in a process known as resonant pumping, thereby resulting in overall faster electron transfer.²⁴⁵

As an additional complication, a more complicated architecture consists of CdSe/ZnSe core/shell QDs anchored on either end of the CdS nanorods (Figure 10F).²⁴⁶ These composite nanorods in essence are characterized by two type II junctions, leading to additional electronic transitions as compared with CdS nanorods or CdSe/CdS nanoscale ‘bar-bells’ alone. In effect, a noticeable red shift and a much more intense photoluminescence peak were observed as compared with that of not only CdS rods alone but also CdSe/CdS DIR structures. The emission intensity also increased with increasing ZnSe content within the structure. Not surprisingly, these heterostructures, when used within an LED device as the electroluminescent layer, demonstrated notable improvement in performance over that of previously reported devices incorporating less chemically complex, control systems with similar morphologies. In effect, the measured efficiency improved from 1.7% to 2.62% with a favorably lower threshold voltage and narrow bandwidth, presumably due to the potential for more facile charge injection.

5.1.3. Doped 0D QD – 1D nanorod structures: QD/dopant chemistry with a ZnS host

Depending on its crystal structure, ZnS maintains known direct bandgaps of ~3.7 to 3.8 eV,²⁴⁷ critical for a number of optoelectronic applications, such as flat-panel displays, injection lasers, as well as light-emitting diodes. In our study,²⁴⁸ upon successful synthesis of the Mn-doped ZnS nanowire host, we attached AET-capped CdSe QDs presumably through electrostatic interactions so as to create viable 0D-1D heterostructures, as shown in Figure 11A.

By constructing these 1D Mn-doped ZnS nanowire - CdSe QD heterostructures, we sought to combine the unique emissive optical signatures of individual Mn ions, ZnS nanowires, and CdSe QDs, such that the effective optical profile of the final discrete heterostructures could span the entire visible spectrum (i.e. 400 to 700 nm) to yield white light emission. Our ‘multi-component’ architecture consisted of (a) annealed 1D ZnS: Mn²⁺ nanowires, pertaining to the cubic zinc blende phase with an intrinsic direct bandgap of 3.72 eV and characterized by a defect-related *blue* emission band located at 400-500 nm, (b) a Mn²⁺ dopant-induced *orange* emission with a peak centered at ~580 nm (associated with the ⁴T₁ to ⁶A₁ transition of Mn²⁺), and (c) 0D CdSe QDs, characterized by an average diameter of 2.3 nm with a *green* emission peak situated at ~520 nm. Hence, these heterostructures possessed *three different but independently tunable luminescent centers*, i.e. emissive ‘building blocks’

From a photophysical perspective, our as-prepared nanoscale ZnS: Mn²⁺ NW - AET-capped CdSe QD heterostructures displayed PL quenching for both ZnS and Mn²⁺ emission bands as compared with unbound 1D ZnS: Mn²⁺. Plausible explanations included a combination of (i) a photoexcited charge transfer occurring from both of the ZnS and Mn²⁺ species to attached CdSe QDs coupled with (ii) energy transfer from the ZnS host onto the immobilized CdSe QDs, in accordance with the bandgap alignment scenario presented in Figure 11E. In parallel, the emission intensities of attached CdSe QDs decreased upon incorporation within as-prepared heterostructures, as compared with their free, unbound counterparts.

More importantly, we found that we could manipulate the intensity and wavelength of these observed emission peaks within these heterostructures, through relatively simple steps such as modifying the attachment ratios of the CdSe QDs onto the underlying ZnS nanowires and/or controlling the doping amounts of Mn²⁺ ions. In Figure 11B, for example, we increased the CdSe

QD to ZnS: Mn²⁺ ratio from 1.5: 1 to 3: 1, and noted that the resulting PL profile exhibited significantly more PL quenching. Separately, we were able to produce a shift in chromaticity within the overall white color region by reducing the Mn²⁺ dopant ratio from 2.22% to 0.45%. As such, our inorganic QD-based heterostructures possessed not only broadly tunable color emission performance (Figure 11D) but also structural durability. These interesting property attributes are helpful towards engineering an increase in device lifetimes under high luminance conditions, a necessary requirement for flat panel displays and imaging applications.²⁴⁸

5.1.4. Other Examples: Epitaxial growth of 0D-1D hybrid nanostructures.

Epitaxial growth, which implies the deposition and growth of a crystalline material onto the well-defined surface of a crystalline substrate with the overlayer possessing the same crystalline orientation as the underlying substrate, is important and relevant for creating metal chalcogenide materials, such as but not limited to MoS₂ and WSe₂,^{249, 250} which maintain wide applicability in diverse fields, such as opto-electronics, photocatalysis, and plasmonics. In particular, this method is effective in creating well-defined 2D-2D heterojunction systems.²⁵¹ Nevertheless, epitaxial growth, through the mediation of techniques such as colloidal synthesis,, chemical reduction, and CVD, can also be utilized into the analogous production of 0D-1D heterostructures, characterized by high degree of control over parameters, such as chemical composition, morphology, crystalline phases, and facet production.²⁵² Herein, we provide for two illustrative examples that demonstrate the vast potential of this synthesis method.

For instance, CdS nanoparticles have been immobilized onto Bi₂S₃ nanowires to generate 0D-1D heterostructures through epitaxial growth.²⁵³ The underlying Bi₂S₃ nanowires measured several hundred nanometers long and 10 nm wide; as-prepared, 20 nm-sized, triangular CdS nanoparticles were grown epitaxially onto the surfaces of these nanowires. In this system, the

orthorhombic Bi_2S_3 (501) and Bi_2S_3 (002) planes were parallel to that of hexagonal CdS (1-210) and CdS (-1-120), respectively; moreover, the direction of the crystalline Bi_2S_3 [010] zone axis was parallel to that of the corresponding zone axis of CdS [0001]. This heterostructure was used as a photocatalyst to decompose methyl red under UV light. As compared with commercial TiO_2 , the 0D-1D heterostructure exhibited an excellent activity with the ability to degrade 90% of the dye after 40 min of reaction. This enhanced performance was attributed to the fortuitous combination of (i) the size of the CdS nanoparticles, which impacted their observed band gap, with implications for the charge carrier separation and recombination potential within the entire heterostructure and (ii) the high specific surface area of the underlying Bi_2S_3 nanowire.

A related example involved the synthesis of branched topological heterostructures²⁵⁴ in which 0D nanoparticles of CdSe were immobilized onto extended tetrapods of CdTe. What was interesting about these heterostructured branched tetrapods was that long-range charge separation could be achieved with the electrons localized at the CdSe zinc blende core and the holes delocalized in the outer CdTe branches, 30 nm or more away; as such, this charge separation was found to strongly quench heterostructure luminescence. Because this ‘charge separation distance’ could be tuned by varying the physical dimensions of the central tetrapod, this architecture was highly relevant in terms of designing novel photovoltaic energy conversion configurations.

5.2. Ternary Metal Chalcogenide-based Heterostructures

By analogy with binary metal chalcogenide-based heterostructures, ternary metal chalcogenide possess similarly desirable optical characteristics. For example, the emission of common II-III-VI ternary metal chalcogenides, such as CuInS_2 or CuInSe_2 , can be systematically tuned from the visible range to IR region,²⁵⁵ an attribute ideal for bio-imaging or LED applications. As an example, $\text{CuInSe}_2/\text{CuInS}_2$ dot-in-rod heterostructures, generated through a

series of cation exchange processes, give rise to a near IR luminescence²⁵⁵ with slower carrier dynamics and longer lifetimes, as compared with constituent control samples, an observation which is beneficial for the photovoltaic applications. A different 0D-1D heterostructure with a chemical composition of $\text{Cu}_{31}\text{S}_{16}$ - CuInS_2 was generated using an oil/aqueous interlayer and incorporating in Cu^{2+} and In^{3+} precursors; the resulting composite possessed a ‘carrot-like’ motif with a 0D $\text{Cu}_{31}\text{S}_{16}$ ‘head’ structure of ~ 28 nm in diameter atop a 1D CuInS_2 ‘tail’ with a length of 62.5 nm.²⁵⁶ Despite these tangible advances in heterostructure synthesis, we should note that neither of these composites had been effectively optimized for their photophysical attributes.

6. Ternary Metal fluoride-based Heterostructures

6.1. NaYF_4 : Idea of intrinsic morphology-specific physical surface area and porosity. Trend in energy transfer efficiency correlates well with QD loading.

NaYF_4 compounds represent an exceptional host lattice for upconversion materials, because they possess inherently lower phonon energies, and can thereby reduce non-radiative phonon relaxation processes with added rare-earth ion dopants by minimizing interactions between electrons and phonons.^{257, 258} In this effort,²⁵⁹ our foremost objective was to produce samples characterized by a pure and well-defined combination of crystallographic phase and morphology with the hope of being able to make meaningful structure-property correlations based on size, shape/morphology, and chemical composition.

What we found was that ostensibly minor alterations in reaction conditions made a substantial difference. For example, the sample synthesized in the presence of 0.2 M ammonia at 100°C for 2 h yielded exclusively α phase for composition coupled with a spherical morphology measuring 150 nm to 300 nm (Figure 12A). Interestingly, the sample generated with a slightly

higher base concentration, i.e. 0.8 M ammonia under otherwise identical conditions yielded an exclusive β crystalline phase but this environment also led to the formation of larger nanowire aggregate bundles with overall dimensions of $1.5 \pm 0.1 \mu\text{m}$ in diameter and $5.3 \pm 0.6 \mu\text{m}$ in length, each of which was individually composed of constituent, ultrathin ($d \sim 5 \text{ nm}$), micron-long one-dimensional subunits (Figure 12B). Our subsequent optical characterization analysis implied that (i) the presence of β -phase in addition to (ii) the overall crystalline domain size could account for improved upconversion efficiencies.

The corresponding NaYF₄-CdSe QD heterostructures were formed by the incubation of a mixture of fluoride, organic surfactant, and a CdSe QD solution in a controlled atmosphere, followed by a combination of sonication, low-temperature heating, and stirring steps. In terms of their resulting optical behavior, we demonstrated increased quenching with composites incorporating the notably more nanoporous 0D particulates as opposed to using 1D nanowires of NaYF₄ with the data shown in Figure 12C and D. This observation was ascribed to the relatively higher surface area of the 0D motifs, coupled with surface “anchoring” hydroxyl groups for optimal QD loading. These distinctive low dimensional morphological manifestations of fluoride structures also turned out to be an excellent energy donating species towards CdSe QDs, as we measured significant PL intensity increases in the CdSe emission peak at 620 nm upon heterostructure formation. Our data suggested that with higher QD loading ratio, the efficiency of Förster resonance energy transfer (FRET) improved and hence was dependent upon the quantitative amount of QDs present immobilized onto the underlying fluoride host. As an additional ‘reaction knob’, we found that doping with different rare-earth metal ions, i.e. Yb³⁺ and Er³⁺, could also yield distinctive optical signatures (Figure 12E). In effect, we showed that we could potentially tune the optoelectronic properties of these heterostructures, i.e. optimize the

energy transfer process from upconverting NaYF₄ to an adjoining light sensitizing species, such as CdSe QDs, by simply altering the morphology and phase of the constituent component NaYF₄ materials to effectively harness a broader range of the solar spectrum.²⁵⁹

A similar, recently reported conceptual effort centered²⁶⁰ on the production of NaYF₄:Yb, Tm micron-scale rods synthesized with Yb³⁺ and Tm³⁺ dopant concentrations set at 30% and 0.5%, respectively. Yb³⁺ was the sensitizer in the near IR region, whereas Tm³⁺ could absorb light in both the visible and UV light regions of the spectrum. CdS was subsequently deposited onto the surface of NaYF₄:Yb, Tm through an in situ reaction process, thereby forming a core-shell composite with excellent photocatalytic capability in terms of more effectively degrading Rhodamine B dye under near IR light irradiation as compared with standard CdS nanocrystals.

6.2. Metal Fluoride Systems Beyond NaYF₄

Based on a thorough search of the literature and to the best of our knowledge, apart from what we have discussed herein, we can conclude that there are no additional reports of other 1D metal fluorides bound to 0D QDs. However, we have found evidence for a number of other potential fluoride-containing motifs that could be viably construed as optically relevant, constituent ‘building blocks’ in combination with QDs for future composite heterostructures.

Examples include structures such as rare-earth fluoride nanowires incorporating Y, Sm, Eu, Gd, Tb, Dy, and Ho,²⁶¹ wherein Eu³⁺ and Tb³⁺ dopants could have been used for down-conversion with either Yb³⁺/Er³⁺ or Yb³⁺/Tm³⁺ co-dopants for up-conversion. In addition, core-shell structures composed of NaYF₄ nanorods co-doped with Yb³⁺ and Er³⁺ and coated with a thin SiO₂ shell maintain a high surface-area, porous geometry, implying the potential of NaYF₄/SiO₂-QD heterostructures for strong upconversion luminescence.²⁶² Furthermore, β-NaGdF₄ have been controllably generated as multiple, uniform morphologies including as 0D

nanoparticles, 1D micron-scale rods, and 3D submicron-scale spherical motifs, which might serve as viable platforms for subsequent attachment with QDs.²⁶³ Moreover, as both YF₃ and YOF possess the potential for multicolor emission with tunable optical properties, one could envision exploring the roles of deliberately tuning either their chemical composition (i.e., doping with different rare earth elements such as Tb, Eu, Tm, Dy, Ho, or Sm) or their morphology/aspect ratio (i.e., 1D nanorod, 0D spheres/nanoparticles, or 3D motifs)²⁶⁴ to tailor a desired optical behavior. In combination with QDs, such a strategy could be used to produce LEDs of variable emissive coloration.²⁶⁵

7. Thoughts on Future Directions for the Field

As previously mentioned, nanoscale heterostructures offer a number of desirable attributes for optical applications, including but not limited to relatively high electron and hole transport efficiencies, a tunable band-gap alignment, and the possibility of multi-exciton generation. The preponderance of research discussed herein has demonstrated that the optical properties of heterostructures can be reproducibly tuned via rational variations of physical structure, morphology, and chemical composition. However, a number of scientific issues remain unresolved, and these limitations prevent the widespread, ubiquitous, and practical use of these heterostructures, especially for solar-based applications.

For example, the role of interfaces between the 0D and 1D constituent components within these heterojunctions remains ill-defined. Furthermore, there are few if any clear theoretical models that can adequately and convincingly predict the behavior of these systems, especially a priori. As we have seen, density functional theory (DFT) calculations suggest that not only that the energy levels of QDs shift with different chemical ligand treatments²⁶⁶ but also the binding

modes of linker molecules can influence QD coverage and aggregation, all of which impact upon the nature of observed charge separation, recombination, and transport properties.^{125, 267} Indeed, there are clearly a number of complex and interconnected photodynamic processes occurring, which dominate charge separation and transfer, as manifested in (i) narrowing and broadening of the observed peak shape, (ii) shifts in the peak position itself, as well as (iii) quenching and enhancement of the peak intensity. Nonetheless, these observations are ostensibly governed by chemical and structural factors, such as the presence of point defects, internal grain boundaries, and dopants, all of which affect the degree of scattering and recombination with consequential effects upon parameters such as the observed photocurrent, fill factors, open circuit voltages, and photoconversion efficiency.¹²⁴

Therefore, understanding the local nature and effect of these interfaces is critical to fully controlling and tailoring the performance of practical ‘field-ready’ systems, such as solar cells, light emitting diodes, and photocatalysts. In our group, we have attempted to achieve deeper insights through a simultaneous and synergistic combination of Raman, NEXAFS, theory, and electrical transport measurements. As an example, within DWNT-CdSe heterostructure shown in Figure 2, the C *K*-edge of the DWNTs was analyzed as an indirect probe of charge transfer. In the literature, as an illustrative case, synchrotron radiation photoelectron spectroscopy has been used to ascertain band alignment within ZnO/PbSe heterostructured interfaces.²⁶⁸ Moreover, analogous ZnO/CdSe heterostructures have been analyzed using synchrotron-based ultraviolet photoelectron spectroscopy; bandgap alignment in the context and presence of different QD sizes were deduced more accurately using this approach.²⁶⁹ Yet much more needs to be done.

As such, it is likely that the application of more sophisticated and intrinsically more sensitive characterization techniques would be helpful towards gaining a better perspective about

the structural and electronic nature of the interfaces within these heterostructures with simultaneously high spatial and temporal resolution. Moreover, it would be preferable at some point in the future to be able to truly ‘visualize’ and monitor the intricate dynamics and evolution of charge transfer occurring not only at but also across multi-dimensional nanoscale interfaces in real time and under in situ conditions, especially in the context of realistic device configurations. What progress has been made towards achieving that specific goal?

Under current experimental conditions, what can be done reliably and reproducibly is to study photoinduced ultrafast electron transfer from CdSe QDs to a metal complex using transient spectroscopy.²⁷⁰ Indeed, transient absorption (TA) spectra have also been used to ascertain the photophysics of CdSe – metal oxide donor-to-acceptor complexes,²⁷¹ with the transient absorption kinetic decay spectra used to examine recombination behavior. Indeed, TA spectroscopy is especially suitable for understanding interfacial electron recombination and transfer within different types of systems, including but not limited to colloidal QDs,²⁷² core shell QDs,^{273,274} and ligand-modified QDs.²⁷⁵ However, this technique, especially in complementary combination with other characterization methods, has not been fully utilized to probe the interfaces of 0D-1D heterostructures, due to difficulties associated with data interpretation and sample throughput.²⁷⁶ Moreover, this type of idea has been explored in the context of analogous 0D-2D heterostructures. Specifically, ultrafast femtosecond pump-probe measurements detected sub-45 fs charge transfer in a core-shell CdSe/ZnS QD – 2D WS₂ hybrid structure, and it was concluded that electron transfer from the 2D excitons to the 0D QD was the dominant charge-transfer pathway.²⁷⁷ Within analogous core-shell CdSe/ZnS – 2D SnS₂ heterostructures, the rate of intrahybrid non-radiative energy transfer increased with the added numbers of SnS₂ atomic layers,²⁷⁸ of relevance for photovoltaics and photon sensing. These

studies collectively monitored charge and energy transfer within interfacial junctions as a means for potentially controlling exciton recombination. While comparable TA literature exists with respect to individual discrete systems such as Ag nanoparticles and nanowires,²⁷⁹ CdSe and CdTe nanowires,^{280, 281} as well as ZnO nanowires,²⁸² the more complex and interesting combination of 0D-1D heterostructures still remains to be properly analyzed using this technique.

Nonetheless, the ability to properly tune and tailor the magnitude and direction of energy versus charge transfer channels ‘on demand’ within heterostructure configurations, especially within a complex electrolytic solution environment characteristic of QDSSCs, still remains as a significant challenge. Indeed, a viable means of simultaneously enhancing absorption while optimizing light harvesting efficiencies (in terms of capturing hot electrons, encouraging MEG enhancement effects, and promoting charge diffusion) continues to be an elusive goal.

Beyond fundamental science, serious issues still remain with respect to developing protocols for reproducibly generating ‘pure’ (i.e. defect minimization so as to increase concomitant carrier mobility), homogeneous (i.e., with precise surface geometry and exposed facets of individual components), crystalline (so as to decrease trap states),²⁸³ and uniformly well-characterized heterostructures in gram and even ton quantities, which would be at a production level relevant and useful for practical commercial device applications. As an example, commercializing heterostructure-based QDSSCs would necessitate not only consistent and uniform large-scale heterostructure film fabrication (possibly incorporating multiple sensitizing species with high loadings and reproducible surface coverage) but also their proven functional compatibility with additional polymer, counter-electrode, and electrolyte components within the device configuration. Indeed, the scalability issue, i.e. the reliable generation of regularly ordered and well-packed assemblies of these composites over macroscopic areas especially incorporating

solution processing conditions, hinders the pursuit of more imaginative and more nuanced strategies towards a rational engineering of devices for improving and optimizing performance metrics within stable, effective solar cell, photocatalytic, and LED configurations. Nonetheless, as we have seen in this Perspective, ‘lab-scale’ studies have at least demonstrated the potential of these 0D-1D heterojunctions as a viable means towards improving light harvesting capabilities, light absorption and power conversion efficiencies, and enhanced photo-responses.¹⁴³

Toxicology is another critical consideration that impacts not only the choice of heterostructure production routes but also the expected life cycle of these materials in terms of their disposal, recovery, and subsequent re-use. For example, QDs contain toxic heavy metals, such as cadmium, whereas the intrinsic toxicity of CNTs themselves is dependent upon their size, anisotropic shape, and surface chemistry (i.e., degree of oxidation). Few if any reports exist on the potential toxicity of 1D-0D heterostructures, incorporating these types of materials, resulting from either inhalation, dermal contact, or ingestion routes. Hence, a number of issues remain, concerning the possible cytotoxicity and in vivo degradation pathways of these unusual composites.²⁸⁴⁻²⁸⁶ These issues have motivated the search for ‘greener’ and potentially more sustainable alternatives and improved methods for the reliable production of not only the individual nanoscale constituent components but also the composite heterostructures themselves.

Overall, an important future step would be in promoting advances towards the spatial integration, stabilization, and ultimately, optimization of these composite materials within more sophisticated, realistic device scenarios. Such an approach would minimize recombination issues and other undesirable loss mechanisms, while simultaneously maximizing key long-term performance parameters including stability and photocurrent generation, especially under ambient and/or realistic operating environmental conditions.

8. Conclusions

In reported work on heterostructures, we and others have subscribed to the notion that (a) the most interesting optoelectronic behavior (e.g. phenomena such as charge transfer as well as energy transfer) occurs at the interfaces created between 2 (or more) distinctive nanomaterials bound together and that (b) controlled synthesis can be used to impact upon structure-property correlations. Within our own group, we have been interested in the design of a series of chemically linked, multi-functional nanoscale hetero-structures using diverse and generalizable solution-based strategies. As previously mentioned, the idea is that the unique and desirable properties of individual nanostructures can be significantly enhanced in potentially unforeseen ways through the formation of inorganic nanoscale heterostructures composed of different, unique, and complementary constituent subunits. We have concentrated our attention primarily on 0D-1D heterostructure formation, and highlighted a number of distinctive heterostructures as representative model examples. However, similar concepts are highly applicable towards the production of other presumably more complex types of composites, composed of multiple constituent subunits possessing arbitrary size, shape and chemical composition. To assist in acquiring a holistic idea of the various systems discussed in this Perspective, we have constructed a series of Summary Tables in which we have presented the collective wisdom of lessons learned from the past literature. These results point out the importance of not only (i) the chemical composition and tunable reaction parameters (i.e., size and associated linker identity) of the 0D QDs but also (ii) the physical morphology, chemistry, and crystallographic nature of the underlying 1D motifs, coupled with (iii) the attachment protocol used to create the as-prepared heterostructures. All of these factors have

measurably impacted upon the net observables for various applications of these 0D-1D materials in terms of photocatalytic performance, light harvesting potential, and optoelectronic behavior.

What the community has shown in this Perspective is that the size dependent optical and electronic properties of QDs can be ‘re-defined’ and ‘re-tooled’ in the context of nanoscale QD-based heterostructures. Broadly speaking, the quenching behavior of QDs when in contact with 1D motifs can be purposefully controlled by deliberative modifications in the attachment protocols (i.e. covalent versus non-covalent). At a deeper level, tunable modifications in the chemistry and physical structure of ligands as manifested in tailorable lengths, degree of electron-rich π -conjugation, identity of functional terminal groups, and variable electron donating/withdrawing behavior become critical in terms of dictating observed optoelectronic behavior. Nevertheless, it has been demonstrated that controlling additional structural and chemical parameters also makes a tangible difference. In this light, we and others have recently correlated the optical absorption, luminescence (i.e. emission) behavior, as well as the corresponding lifetimes with tunable synthetic parameters, such as (i) morphology and dimensionality considerations (i.e. 0D, 1D, 3D, as well as DIR motifs), (ii) QD size and coverage density, (iii) QD identity, (iv) the presence of activating species such as rare earth lanthanide dopant ions (i.e. Ce, Eu, & Tb), (v) the physical tunability and chemical processability of intervening ligands, and (vi) the formation of composites incorporating co-sensitized species. All of these diverse reaction variables fundamentally govern the observed behavior of classes of *QD* (i.e. CdSe and CdS) – *one-dimensional* (i.e. carbon nanotubes as well as phosphates, tungstates, sulfides, and fluorides) *heterostructures*.

These particular efforts have been of general interest for creating interesting photovoltaic and solar cell architectures. Nonetheless, it is still experimentally non-trivial either (i) to probe the growth and structural evolution of these structures kinetically or (ii) to monitor their associated

dynamic charge transfer processes under realistic *in situ*, operando conditions. Contributions in these specific areas would enable corresponding advances in the theoretical understanding of nanoscale behavior within these complex motifs. In terms of additional challenges that still hinder progress in the field and render reliable structure-property correlations more difficult,²⁸⁷ a number of important ones still remain, despite years of concerted efforts from a number of different groups. Some of the most notable concerns include (i) developing innovative, generalizable, and reproducible ways of reliably controlling the number, density, and spatial localization of QDs functionalized onto any of these types of underlying 1D templates; (ii) understanding the role and improving the detectability of defects; as well as (iii) sustainably and reliably producing these composites on a large industrial-scale level for their widespread incorporation within functional device configurations.

9. Acknowledgements

Research funding for the original underlying studies had been provided by the U.S. Department of Energy, Office of Science, Basic Energy Sciences, Materials Sciences and Engineering Division and were related to experiments, writing, and analyses conducted at Brookhaven National Laboratory, which is supported by the U.S. Department of Energy under Contract No. DE-SC-00112704. We also thank the prior inspiration, contributions, and work of Jinkyu Han, Lei Wang, Haiqing Liu, James Misewich, Robert Harrison, Daniel Fischer, and Joerg Appenzeller, which had been instrumental in preparing the content of this paper.

References

1. P. O. Anikeeva, J. E. Halpert, M. G. Bawendi and V. Bulovic, *Nano Lett.*, 2009, **9**, 2532-2536.
2. Y. Lai, M. Meng, Y. Yu, X. Wang and T. Ding, *Appl. Catal., B*, 2011, **105**, 335-345.
3. X. Fang, Y. Bando, M. Liao, U. K. Gautam, C. Zhi, B. Dierre, B. Liu, T. Zhai, T. Sekiguchi, Y. Koide and D. Golberg, *Adv. Mater.*, 2009, **21**, 2034-2039.
4. S. Ravindran, S. Chaudhary, B. Colburn, M. Ozkan and C. S. Ozkan, *Nano Lett.*, 2003, **3**, 447-453.
5. M. Ni, M. K. H. Leung, D. Y. C. Leung and K. Sumathy, *Renewable Sustainable Energy Rev.*, 2007, **11**, 401-425.
6. S. Ye, F. Xiao, Y. X. Pan, Y. Y. Ma and Q. Y. Zhang, *Mater. Sci. Eng., R*, 2010, **71**, 1-34.
7. J. Low, J. Yu, M. Jaroniec, S. Wageh and A. A. Al-Ghamdi, *Adv. Mater.*, 2017, **29**, 1601494.
8. L. Zhang and M. Jaroniec, *Appl. Surf. Sci.*, 2018, **430**, 2-17.
9. C. B. Murray, D. J. Noms and M. G. Bawendi, *J. Am. Chem. Soc.*, 1993, **115**, 8706-8715.
10. A. P. Alivisatos, *Science*, 1996, **271**, 933-937.
11. A. J. Nozik, *Chem. Phys. Lett.*, 2008, **457**, 3-11.
12. A. J. Nozik, M. C. Beard, J. M. Luther, M. Law, R. J. Ellingson and J. C. Johnson, *Chem. Rev.*, 2010, **110**, 6871-6890.
13. M. C. Beard, *J. Phys. Chem. Lett.*, 2011, **2**, 1282-1288.
14. M. C. Beard, A. G. Midgett, M. C. Hanna, J. M. Luther, B. K. Hughes and A. J. Nozik, *Nano Lett.*, 2010, **10**, 3019-3027.
15. M. C. Beard, A. G. Midgett, M. Law, O. E. Semonin, R. J. Ellingson and A. J. Nozik, *Nano Lett.*, 2009, **9**, 836-845.
16. A. Luque, A. Martí and A. J. Nozik, *MRS Bull.*, 2011, **32**, 236-241.
17. R. J. Ellingson, M. C. Beard, J. C. Johnson, P. Yu, O. I. Micic, A. J. Nozik, A. Shabaev and A. L. Efros, *Nano Lett.*, 2005, **5**, 865-871.
18. R. D. Schaller and V. I. Klimov, *Phys. Rev. Lett.*, 2004, **92**, 186601.
19. M. C. Beard, K. P. Knutsen, P. R. Yu, J. M. Luther, Q. Song, W. K. Metzger, R. J. Ellingson and A. J. Nozik, *Nano Lett.*, 2007, **7**, 2506-2512.
20. G. Nair, S. M. Geyer, L. Y. Chang and M. G. Bawendi, *Phys. Rev. B*, 2008, **78**, 125325.
21. O. E. Semonin, J. M. Luther, S. Choi, H.-Y. Chen, J. Gao, A. J. Nozik and M. C. Beard, *Science*, 2011, **334**, 1530-1533.
22. V. I. Klimov, *J. Phys. Chem. B*, 2006, **110**, 16827-16845.
23. Y.-S. Lee, C. V. V. M. Gopi, A. E. Reddy, C. Nagaraju and H.-J. Kim, *New J. Chem.*, 2017, **41**, 1914-1917.
24. Z. Yang, J. Z. Fan, A. H. Proppe, F. P. G. Arquer, D. Rossouw, O. Voznyy, X. Lan, M. Liu, G. Walters, R. Quintero-Bermudez, B. Sun, S. Hoogland, G. A. Botton, S. O. Kelley and E. H. Sargent, *Nat. Commun.*, 2017, **8**, 1325.
25. F. Zhang, Z. Wang, H. Zhu, N. Pellet, J. Luo, C. Yi, X. Liu, H. Liu, S. Wang, X. Li, Y. Xiao, S. M. Zakeeruddin, D. Bi and M. Grätzel, *Nano Energy*, 2017, **41**, 469-475.
26. D. Bi, C. Yi, J. Luo, J.-D. Décoppet, F. Zhang, S. M. Zakeeruddin, X. Li, A. Hagfeldt and M. Grätzel, *Nat. Energy*, 2016, **1**, 16142.
27. Z. Ahmad, M. A. Najeeb, R. A. Shakoor, S. A. Al-Muhtaseb and F. Touati, *Renewable Sustainable Energy Rev.*, 2018, **82**, 1551-1564.
28. Z. Zheng, H. Ji, P. Yu and Z. Wang, *Nanoscale Res. Lett.*, 2016, **11**, 266.

29. M. C. Hanna, M. C. Beard and A. J. Nozik, *J. Phys. Chem. Lett.*, 2012, **3**, 2857-2862.
30. S. Lu and A. Madhukar, *Nano Lett.*, 2007, **7**, 3443-3451.
31. P. K. Santra and P. V. Kamat, *J. Am. Chem. Soc.*, 2012, **134**, 2508-2511.
32. A. Kongkanand, K. Tvrđy, K. Takechi, M. Kuno and P. V. Kamat, *J. Am. Chem. Soc.*, 2008, **130**, 4007-4015.
33. V. Wood, M. J. Panzer, J. E. Halpert, J.-M. Caruge, M. G. Bawendi and V. Bulovic, *ACS Nano*, 2009, **3**, 3581-3586.
34. H. McDaniel, N. Fuke, N. S. Makarov, J. M. Pietryga and V. I. Klimov, *Nat. Commun.*, 2013, **4**, 2887.
35. Y.-L. Lee and Y.-S. Lo, *Adv. Funct. Mater.*, 2009, **19**, 604-609.
36. H. Choi and S. Jeong, *IJPEM-GT*, 2018, **5**, 349-358.
37. S. Ruhle, M. Shalom and A. Zaban, *ChemPhysChem*, 2010, **11**, 2290-2304.
38. J. Tian and G. Cao, *Nano Rev.*, 2013, **4**, 22587.
39. M. R. Kim and D. Ma, *J. Phys. Chem. Lett.*, 2015, **6**, 85-99.
40. G. Wang, X. Yang, F. Qian, J. Z. Zhang and Y. Li, *Nano Lett.*, 2010, **10**, 1088-1092.
41. D. Bera, L. Qian, T.-K. Tseng and P. H. Holloway, *Materials*, 2010, **3**, 2260-2345.
42. X. Dai, Z. Zhang, Y. Jin, Y. Niu, H. Cao, X. Liang, L. Chen, J. Wang and X. Peng, *Nature*, 2014, **515**, 96-99.
43. J. Weber, R. Singhal, S. Zekri and A. Kumar, *Int. Mater. Rev.*, 2008, **53**, 235.
44. N. Wang, Y. Cai and R. Q. Zhang, *Mater. Sci. Eng., R*, 2008, **60**, 1-51.
45. L. Cademartiri and G. A. Ozin, *Adv. Mater.*, 2009, **21**, 1013-1020.
46. Y. N. Xia, P. D. Yang, Y. G. Sun, Y. Y. Wu, B. Mayers, B. Gates, Y. D. Yin, F. Kim and Y. Q. Yan, *Adv. Mater.*, 2003, **15**, 353-389.
47. B. Lim, M. J. Jiang, P. H. C. Camargo, E. C. Cho, J. Tao, X. M. Lu, Y. M. Zhu and Y. N. Xia, *Science*, 2009, **324**, 1302-1305.
48. X. N. Zhang, C. R. Li and Z. Zhang, *Appl. Phys. A: Mater. Sci. Process.*, 2006, **82**, 33-37.
49. K. Tomioka, J. Motohisa, S. Hara and T. Fukui, *Nano Lett.*, 2008, **8**, 3475-3480.
50. C. Berger, Y. Yi, Z. L. Wang and W. A. de Heer, *Appl. Phys. A: Mater. Sci. Process.*, 2002, **74**, 363-365.
51. A. Javey, G. Jing, W. Qian, M. Lundstrom and H. Dai, *Nature*, 2003, **424**, 654-657.
52. S. J. Wind, J. Appenzeller and P. Avouris, *Phys. Rev. Lett.*, 2003, **91**, 058301.
53. C. T. White and T. N. Todorov, *Nature*, 1998, **393**, 240-242.
54. H. Suzuura and T. Ando, *Phys. Rev. B*, 2002, **65**, 235412.
55. Y. Kanemitsu, *Acc. Chem. Res.*, 2013, **46**, 1358-1366.
56. H. Wang, L. Zhang, Z. Chen, J. Hu, S. Li, Z. Wang, J. Liu and X. Wang, *Chem. Soc. Rev.*, 2014, **43**, 5234-5244.
57. X. Wang, J. A. Alexander-Webber, W. Jia, B. P. Reid, S. D. Stranks, M. J. Holmes, C. C. Chan, C. Deng, R. J. Nicholas and R. A. Taylor, *Sci. Rep.*, 2016, **6**, 37167.
58. A. Kongkanand, R. M. Dominguez and P. V. Kamat, *Nano Lett.*, 2007, **7**, 676-680.
59. G. Zou, D. Zhang, C. Dong, H. Li, K. Xiong, L. Fei and Y. Qian, *Carbon*, 2006, **44**, 828-832.
60. M. Zhang, C. Shao, J. Mu, X. Huang, Z. Zhang, Z. Guo, P. Zhang and Y. Liu, *J. Mater. Chem.*, 2012, **22**, 577-584.
61. A. Robin, E. Lhuillier, X. Z. Xu, S. Ithurria, H. Aubin, A. Querghi and B. Dubertret, *Sci. Rep.*, 2016, **6**, 24909.
62. B. Farrow and P. V. Kamat, *J. Am. Chem. Soc.*, 2009, **131**, 11124-11131.

63. C. Biswas, H. Jeong, M. S. Jeong, W. J. Yu, D. Priyat and Y. H. Lee, *Adv. Funct. Mater.*, 2013, **23**, 3653-3660.
64. N. C. Giebink, G. P. Wiederrecht, M. R. Wasielewski and S. R. Forrest, *Phys. Rev. B*, 2011, **83**, 195326.
65. A. K. Geim and K. S. Novoselov, *Nat. Mater.*, 2007, **6**, 183-191.
66. A. Splendiani, L. Sun, Y. Zhang, T. Li, J. Kim, C. Y. Chim, G. Galli and F. Wang, *Nano Lett.*, 2010, **10**, 1271-1275.
67. X. Yu, M. S. Prevot, N. Guijarro and K. Sivula, *Nat. Commun.*, 2015, **6**, 7596.
68. R. H. Friend and A. D. Yoffe, *Adv. Phys.*, 1987, **36**, 1-94.
69. E. Benavente, M. A. S. Ana, F. Mendizabal and G. Gonzalez, *Coord. Chem. Rev.*, 2002, **224**, 87-109.
70. J. Kang, S. Tongay, J. Zhou, J. Li and J. Wu, *Appl. Phys. Lett.*, 2013, **102**, 012111.
71. S. Banerjee and S. S. Wong, *Nano Lett.*, 2002, **2**, 195-200.
72. S. Banerjee and S. S. Wong, *J. Am. Chem. Soc.*, 2003, **125**, 10342-10350.
73. S. Banerjee and S. S. Wong, *Adv. Mater.*, 2004, **16**, 34-37.
74. S. Banerjee and S. S. Wong, *Chem. Commun.*, 2004, **16**, 1866-1867.
75. X. Peng and S. S. Wong, *Chem. Mater.*, 2009, **21**, 682-694.
76. I. Robel, B. A. Bunker and P. V. Kamat, *Adv. Mater.*, 2005, **17**, 2458-2463.
77. N. Cho, K. R. Choudhury, R. B. Thapa, Y. Sahoo, T. Ohulchanskyy, A. N. Cartwright, K. S. Lee and P. N. Prasad, *Adv. Mater.*, 2007, **19**, 232-236.
78. F. Vietmeyer, B. Seger and P. V. Kamat, *Adv. Mater.*, 2007, **19**, 2935-2940.
79. M. Olek, T. Busgen, M. Hilgendorff and M. Giersig, *J. Phys. Chem. B*, 2006, **110**, 12901-12904.
80. V. Biju, T. Itoh, Y. Baba and M. Ishikawa, *J. Phys. Chem. B*, 2006, **110**, 26068-26074.
81. D. Wang, J. K. Baral, H. Zhao, B. A. Gonfa, V.-V. Truong, M. A. El Khakani, R. Izquierdo and D. Ma, *Adv. Funct. Mater.*, 2011, **21**, 4010-4018.
82. X. Peng, M. Y. Sfeir, F. Zhang, J. A. Misewich and S. S. Wong, *J. Phys. Chem. C*, 2010, **114**, 8766-8773.
83. L. Wang, J. Han, J. Hoy, F. Hu, H. Liu, M. M. Gentleman, M. Y. Sfeir, J. A. Misewich and S. S. Wong, *Dalton Trans.*, 2014, **43**, 7480-7490.
84. S. Azoz, J. Jiang, G. Keskar, C. McEnally, A. Alkas, F. Ren, N. Marinkovic, G. L. Haller, S. Ismail-Beigi and L. D. Pfefferle, *Nanoscale*, 2013, **5**, 6893-6900.
85. J. Schornbaum, B. Winter, S. P. Schießl, B. Butz, E. Spiecker and J. Zaumseil, *Chem. Mater.*, 2013, **25**, 2663-2669.
86. I. Ka, V. Le Borgne, D. Ma and M. A. El Khakani, *Adv. Mater.*, 2012, **24**, 6289-6294.
87. D. V. Talapin and a. E. V. Shevchenko, *Nano Lett.*, 2007, **7**, 1213-12189.
88. L. Wang, J. Han, Y. Zhu, R. Zhou, C. Jaye, H. Liu, Z.-Q. Li, G. T. Taylor, D. A. Fischer, J. Appenzeller and S. S. Wong, *J. Phys. Chem. C*, 2015, **119**, 26327-26338.
89. Y. Zhu, R. Zhou, L. Wang, S. S. Wong and J. Appenzeller, *ACS Energy Lett.*, 2017, **2**, 717-725.
90. K. O. Vieira, J. Bettini, J. L. Ferrari and M. A. Schiavon, *Mater. Chem. Phys.*, 2015, **149-150**, 405-412.
91. S. Fang, M. Sun, Y. Zhou, Q. Liang, Z. Li and S. Xu, *J. Alloys Compd.*, 2016, **656**, 771-776.
92. A. Abouelsayed, B. Anis, A. Okasha, A. M. Ali, W. Elhotaby and A. S. G. Khalil, *Mater. Chem. Phys.*, 2018, **203**, 1-8.

93. I. Robel, M. Kuno and P. V. Kamat, *J. Am. Chem. Soc.*, 2007, **129**, 4136-4137.
94. S. L. Diedenhofen, D. Kufer, T. Lasanta and G. Konstantatos, *Light: Sci. Appl.*, 2015, **4**, e234.
95. R. M. Metzger, *Chem. Rev.*, 2003, **103**, 3803-3834.
96. L. Wang, J. Han, B. Sundahl, S. Thornton, Y. Zhu, R. Zhou, C. Jaye, H. Liu, Z. Q. Li, G. T. Taylor, D. A. Fischer, J. Appenzeller, R. J. Harrison and S. S. Wong, *Nanoscale*, 2016, **8**, 15553-15570.
97. F. Mammeri, A. Ballarin, M. Giraud, G. Brusatin and S. Ammar, *Colloids Surf., A*, 2013, **439**, 138-144.
98. A. Attanzio, A. Sapelkin, F. Gesuele, A. van der Zande, W. P. Gillin, M. Zheng and M. Palma, *Small*, 2017, **13**, 1603042.
99. G. Landi, M. Henninger, A. De Girolamo del Mauro, C. Borriello, T. Di Luccio and H. C. Neitzert, *Opt. Mater.*, 2013, **35**, 2490-2495.
100. R. Thierry, G. Perillat-Merceroz, P. H. Jouneau, P. Ferret and G. Feuillet, *Nanotechnology*, 2012, **23**, 085705.
101. D. I. Son, B. W. Kwon, D. H. Park, W. S. Seo, Y. Yi, B. Angadi, C. L. Lee and W. K. Choi, *Nat. Nanotechnol.*, 2012, **7**, 465-471.
102. C.-T. Hu, J.-M. Wu, J.-W. Yeh and H. C. Shih, *RSC Adv.*, 2016, **6**, 60877-60887.
103. B. D. Boruah and A. Misra, *Nanotechnology*, 2016, **27**, 355204.
104. X. Mao, X. Yang, J. Wu, W. Tian, G. C. Rutledge and T. A. Hatton, *Chem. Mater.*, 2015, **27**, 4574-4585.
105. X. Jiang, *Phys. Status Solidi A*, 2014, **211**, 2679-2687.
106. S. Peng, L. Li, J. Kong Yoong Lee, L. Tian, M. Srinivasan, S. Adams and S. Ramakrishna, *Nano Energy*, 2016, **22**, 361-395.
107. M. Inagaki, Y. Yang and F. Kang, *Adv. Mater.*, 2012, **24**, 2547-2566.
108. L. Feng, N. Xie and J. Zhong, *Materials*, 2014, **7**, 3919-3945.
109. Z. Zhou, S. Sigdel, J. Gong, B. Vaagensmith, H. Elbohy, H. Yang, S. Krishnan, X.-F. Wu and Q. Qiao, *Nano Energy*, 2016, **22**, 558-563.
110. S. R. Gajjela, K. Anantharayanan, C. Yap, M. Grätzel and P. Balaya, *Energy Environ. Sci.*, 2010, **3**, 838-845.
111. S. H. Ko, D. Lee, H. W. Kang, K. H. Nam, J. Y. Yeo, S. J. Hong, C. P. Grigoropoulos and H. J. Sung, *Nano Lett.*, 2011, **11**, 666-671.
112. J. He, M. Zhou, L. Wang, S. Zhao, Q. Wang, B. Ding and S. Cui, *Electrochim. Acta*, 2016, **215**, 626-636.
113. I. Jeong, J. Lee, K. L. Vincent Joseph, H. I. Lee, J. K. Kim, S. Yoon and J. Lee, *Nano Energy*, 2014, **9**, 392-400.
114. P. Joshi, L. Zhang, Q. Chen, D. Galipeau, H. Fong and Q. Qiao, *ACS Appl. Mater. Interfaces*, 2010, **2**, 3572-3577.
115. J. Huo, J. Wu, M. Zheng, Y. Tu and Z. Lan, *J. Power Sources*, 2015, **293**, 570-576.
116. S. Sigdel, A. Dubey, H. Elbohy, A. Aboagye, D. Galipeau, L. Zhang, H. Fong and Q. Qiao, *J. Mater. Chem. A*, 2014, **2**, 11448-11453.
117. L. Li, J. Xiao, H. Sui, X. Yang, W. Zhang, X. Li, A. Hagfeldt and M. Wu, *J. Power Sources*, 2016, **326**, 6-13.
118. J. Qiu, D. He, R. Zhao, B. Sun, H. Ji, N. Zhang, Y. Li, X. Lu and C. Wang, *J. Colloid Interface Sci.*, 2018, **522**, 95-103.

119. C. Wang, J. Jiang, Y. Ruan, X. Ao, K. Ostrikov, W. Zhang, J. Lu and Y. Y. Li, *ACS Appl. Mater. Interfaces*, 2017, **9**, 28441-28450.
120. L. Li, H. Sui, K. Zhao, W. Zhang, X. Li, S. Liu, K. Yang, M. Wu and Y. Zhang, *Electrochim. Acta*, 2018, **259**, 188-195.
121. J. Xiao, M. Cui, M. Wang, H. Sui, K. Yang, L. Li, W. Zhang, X. Li, G. Fu, A. Hagfeldt and Y. Zhang, *J. Power Sources*, 2016, **328**, 543-550.
122. L. Li, M. Wang, J. Xiao, H. Sui, W. Zhang, X. Li, K. Yang, Y. Zhang and M. Wu, *Electrochim. Acta*, 2016, **219**, 350-355.
123. W. W. Yu, L. Qu, W. Guo and X. Peng, *Chem. Mater.*, 2003, **15**, 2854-2860.
124. P. V. Kamat, *J. Phys. Chem. C* 2008, **112**, 18737-18753.
125. V. Gonza'lez-Pedro, X. Xu, I. Mora-Sero' and J. Bisquert, *ACS Nano*, 2010, **4**, 5783-5790.
126. B. Fang, M. Kim, S.-Q. Fan, J. H. Kim, D. P. Wilkinson, J. Ko and J.-S. Yu, *J. Mater. Chem.*, 2011, **21**, 8742-8748.
127. V. Ganapathy, E. H. Kong, Y. C. Park, H. M. Jang and S. W. Rhee, *Nanoscale*, 2014, **6**, 3296-3301.
128. L. Li, P. Zhu, S. Peng, M. Srinivasan, Q. Yan, A. S. Nair, B. Liu and S. Samakrishna, *J. Phys. Chem. C*, 2014, **118**, 16526-16535.
129. L. Zhang, W. Wang, J. Yang, Z. Chen, W. Zhang, L. Zhou and S. Liu, *Appl. Catal., A*, 2006, **308**, 105-110.
130. C. Ye, Y. Bando, G. Shen and D. Golberg, *J. Phys. Chem. B* 2006, **110**, 15146-15151.
131. S. I. Lee, S. M. Jo, H. I. Joh, M. H. Lee and S. Lee, *Chem. Commun.*, 2015, **51**, 2718-2720.
132. V. Etacheri, R. Roshan and V. Kumar, *ACS Appl. Mater. Interfaces*, 2012, **4**, 2717-2725.
133. G. R. Dillip, A. N. Banerjee, V. C. Anitha, S. W. Joo, B. K. Min, S. Y. Sawant and M. H. Cho, *ChemPhysChem* 2015, **16**, 3214-3232.
134. J. Mu, C. Shao, Z. Guo, Z. Zhang, M. Zhang, P. Zhang, B. Chen and Y. Liu, *ACS Appl. Mater. Interfaces*, 2011, **3**, 590-596.
135. J. Mu, C. Shao, Z. Guo, M. Zhang, Z. Zhang, P. Zhang, B. Chen and Y. Liu, *J. Mater. Chem.*, 2012, **22**, 1786-1793.
136. Y. Mao, T. J. Park and S. S. Wong, *Chem. Commun.*, 2005, 5721-5735.
137. Y. Mao, T. J. Park, F. Zhang, H. Zhou and S. S. Wong, *Small*, 2007, **3**, 1122-1139.
138. J. M. Patete, X. Peng, C. Koenigsmann, Y. Xu, B. Karn and S. S. Wong, *Green Chem.*, 2011, **13**, 482-519.
139. A. L. Tiano, C. Koenigsmann, A. C. Santulli and S. S. Wong, *Chem. Commun.*, 2010, **46**, 8093-8130.
140. A. Loiudice, A. Rizzo, G. Grancini, M. Biasiucci, M. R. Belviso, M. Corricelli, M. L. Curri, M. Striccoli, A. Agostiano, P. D. Cozzoli, A. Petrozza, G. Lanzani and G. Gigli, *Energy Environ. Sci.*, 2013, **6**, 1565-1572.
141. H. Kim, Y. Tak, K. Senthil, J. Joo, S. Jeon and K. Yong, *J. Vac. Sci. Technol. B*, 2009, **27**, 2182-2186.
142. A. D. Liyanage, S. D. Perera, K. Tan, Y. Chabal and K. J. Balkus, *ACS Catal.*, 2014, **4**, 577-584.
143. Y. Ma, Y. Bian, Y. Liu, A. Zhu, H. Wu, H. Cui, D. Chu and J. Pan, *ACS Sustainable Chem. Eng.*, 2018, **6**, 2552-2562.

144. S. Ito, Y. Makari, T. Kitamura, Y. Wada and S. Yanagida, *J. Mater. Chem.*, 2004, **14**, 385-390.
145. A. Kar, S. Kundu and A. Patra, *RSC Adv.*, 2012, **2**, 10222-10230.
146. J. Pan, J. Li, Z. Yan, B. Zhou, H. Wu and X. Xiong, *Nanoscale*, 2013, **5**, 3022-3029.
147. V. K. Gupta, A. Fakhri, M. Azad and S. Agarwal, *J. Colloid Interface Sci.*, 2017, **508**, 575-582.
148. H. Sun, S.-Z. Kang and J. Mu, *J. Dispersion Sci. Technol.*, 2009, **30**, 384-387.
149. H. Chen, W. Liu, A. Zhu, X. Xiong and J. Pan, *Mater. Res. Express*, 2017, **4**, 045019.
150. M. L. Lu, C. H. Lin and Y. F. Chen, *Appl. Phys. Lett.*, 2011, **99**, 081109.
151. M.-L. Lu, C.-W. Lai, H.-J. Pan, C.-T. Chen, P.-T. Chou and Y.-F. Chen, *Nano Lett.*, 2013, **13**, 1920-1927.
152. T. Gao, Q. Li and T. Wang, *Chem. Mater.*, 2005, **17**, 887-892.
153. P. Chen, Z. Liu, X. Geng, J. Wang, M. Zhang, J. Liu and L. Yan, *J. Electron. Mater.*, 2017, **46**, 1532-1538.
154. Q. Nie, L. Yang, C. Cao, Y. Zeng, G. Wang, C. Wang and S. Lin, *Chem. Eng. J.*, 2017, **325**, 151-159.
155. S. Singh and N. Khare, *Chem. Phys. Lett.*, 2015, **634**, 140-145.
156. Y. Wang, F. Wang and J. He, *Nanoscale*, 2013, **5**, 11291-11297.
157. S. Kumar, R. Sharma, V. Sharma, G. Harith, V. Sivakumar and V. Krishnan, *Beilstein J. Nanotechnol.*, 2016, **7**, 1684-1697.
158. W. Lee, S. K. Min, V. Dhas, S. B. Ogale and S.-H. Han, *Electrochem. Commun.*, 2009, **11**, 103-106.
159. Z. Mo, Y. Huang, S. Lu, Y. Fu, X. Shen and H. He, *Optik*, 2017, **149**, 63-68.
160. J. Qi, W. Liu, C. Biswas, G. Zhang, L. Sun, Z. Wang, X. Hu and Y. Zhang, *Opt. Commun.*, 2015, **349**, 198-202.
161. M. Thambidurai, N. Muthukumarasamy, N. Sabari Arul, S. Agilan and R. Balasundaraprabhu, *J. Nanopart. Res.*, 2011, **13**, 3267-3273.
162. P. Sudhagar, S. Chandramohan, R. S. Kumar, R. Sathyamoorthy, C.-H. Hong and Y.-S. Kang, *Phys. Status Solidi A*, 2011, **208**, 474-479.
163. J. Y. Kim and F. E. Osterloh, *J. Am. Chem. Soc.*, 2005, **127**, 10152-11053.
164. K. S. Leschkies, R. Divakar, J. Basu, E. Enache-Pommer, J. E. Boercker, C. B. Carter, U. R. Kortshagen, D. J. Norris and E. S. Aydil, *Nano Lett.*, 2007, **7**, 1793-1798.
165. X. W. Sun, J. Chen, J. L. Song, D. W. Zhao, W. Q. Deng and W. Lei, *Opt. Express*, 2010, **18**, 1296-1301.
166. J. Huang, S. Liu, L. Kuang, Y. Zhao, T. Jiang, S. Liu and X. Xu, *J. Environ. Sci.*, 2013, **25**, 2487-2491.
167. S. B. Rawal, S. D. Sung, S.-Y. Moon, Y.-J. Shin and W. I. Lee, *Mater. Lett.*, 2012, **82**, 240-243.
168. H. M. A. Javed, W. Que, Y. Gao, Y. Xing and L. B. Kong, *Mater. Chem. Phys.*, 2016, **178**, 139-148.
169. K. Jung, J. Lee, Y.-M. Kim, J. Kim, C.-U. Kim and M.-J. Lee, *Electrochim. Acta*, 2016, **220**, 500-510.
170. K. N. Hui, K. S. Hui, X. L. Zhang, R. S. Mane and M. Naushad, *Sol. Energy*, 2016, **125**, 125-134.
171. H. Wang, T. Kubo, J. Nakazaki and H. Segawa, *ACS Energy Lett.*, 2017, **2**, 2110-2117.
172. L. Wang, D. Zhao, Z. Su and D. Shen, *Nanoscale Res. Lett.*, 2012, **7**, 106.

173. Z. Zheng, L. Gan, J. Zhang, F. Zhuge and T. Zhai, *Adv. Sci.*, 2017, **4**, 1600316.
174. N. Singh, Z. Salam, N. Sivasankar and A. Subramania, *Mater. Sci. Semicond. Process.*, 2017, **64**, 16-23.
175. R. L. Hoye, B. Ehrler, M. L. Bohm, D. Munoz-Rojas, R. M. Altamimi, A. Y. Alyamani, Y. Vaynzof, A. Sadhanala, G. Ercolano, N. C. Greenham, R. H. Friend, J. L. MacManus-Driscoll and K. P. Musselman, *Adv. Energy Mater.*, 2014, **4**, 1301544.
176. H. M. Chen, C. K. Chen, Y. C. Chang, C. W. Tsai, R. S. Liu, S. F. Hu, W. S. Chang and K. H. Chen, *Angew. Chem.*, 2010, **122**, 6102-6105.
177. H. Wang, T. Kubo, J. Nakazaki, T. Kinoshita and H. Segawa, *J. Phys. Chem. Lett.*, 2013, **4**, 2455-1460.
178. D. R. Baker and P. V. Kamat, *Adv. Funct. Mater.*, 2009, **19**, 805-811.
179. N. Singh, Z. Salam, A. Subasri, N. Sivasankar and A. Subramania, *Sol. Energy Mater. Sol. Cells*, 2018, **179**, 417-426.
180. M. Zhang, Y. Xu, G. He, X. Song, Z. Sun, J. Lv, L. Yang and X. Jiang, *Nanoscale Res. Lett.*, 2014, **9**, 636.
181. Y. Xie, G. Ali, S. H. Yoo and S. O. Cho, *ACS Appl. Mater. Interfaces*, 2010, **2**, 2910-2914.
182. M. A. Mumin, G. Moula and P. A. Charpentier, *RSC Adv.*, 2015, **5**, 67767-67779.
183. V. Nguyen, W. Li, V. Pham, L. Wang, P. Sheng, Q. Cai and C. Grimes, *J. Colloid Interface Sci.*, 2016, **462**, 389-396.
184. S. Qian, C. Wang, W. Liu, Y. Zhu, W. Yao and X. Lu, *J. Mater. Chem.*, 2011, **21**, 4945-4952.
185. Y. Li, L. Zhang, W. Wu, P. Dai, X. Yu, M. Wu and G. Li, *Nanoscale Res. Lett.*, 2014, **9**, 270.
186. X.-F. Gao, W.-T. Sun, G. Ai and L.-M. Peng, *Appl. Phys. Lett.*, 2010, **96**, 153104.
187. X. Ren, L. Yu, Z. Li, H. Song and Q. Wang, *Superlattices Microstruct.*, 2018, **113**, 696-705.
188. H. Wang, W. Zhu, B. Chong and K. Qin, *Int. J. Hydrogen Energy*, 2014, **39**, 90-99.
189. L. C. Kao, S. Y. H. Liou, C. L. Dong, P. H. Yeh and C. L. Chen, *ACS Sustainable Chem. Eng.*, 2016, **4**, 210-218.
190. J. Zhang, J. Yang, M. Liu, G. Li, W. Li, S. Gao and Y. Luo, *J. Electrochem. Soc.*, 2014, **161**, D55-D58.
191. H. Feng, T. Tran, T. L. Chen, L. Yuan and Q. Cai, *Chem. Eng. J.*, 2013, **215-216**, 591-599.
192. K. P. Acharya, T. R. Alabi, N. Schmall, N. N. Hewa-Kasakarage, M. Kirsanova, A. Nemchinov, E. Khon and M. Zamkov, *J. Phys. Chem. C*, 2009, **113**, 19531-19535.
193. Z. Gyori, Z. Konya and A. Kukovecz, *Appl. Catal., B*, 2015, **179**, 583-588.
194. W. Liao, B. Wang and Z. Liu, *Int. J. Hydrogen Energy*, 2017, **42**, 10962-10970.
195. P. Pathak, M. Podzorski, D. Bahnemann and V. R. Subramanian, *J. Phys. Chem. C*, 2018, **122**, 13659-13668.
196. R. S. Selinsky, S. Shin, M. A. Lukowski and S. Jin, *J. Phys. Chem. Lett.*, 2012, **3**, 1649-1656.
197. G. Zhang, Y. Wu, H. Ding, Y. Zhu, J. Li, Y. Lin, S. Jiang, Q. Zhang, N. Pan, Y. Luobc and X. Wang, *RSC Adv.*, 2015, **5**, 71883-74889.
198. F. Zhang and S. S. Wong, *ACS Nano*, 2009, **4**, 99-112.
199. P. Maestro and D. Huguenin, *J. Alloys Compd.*, 1995, **225**, 520-528.

200. Y. P. Fang, A. W. Xu and W. F. Dong, *Small*, 2005, **1**, 967-971.
201. C. R. Patra, R. Bhattacharya, S. Patra, S. Basu, P. Mukherjee and D. Mukhopadhyay, *Clin. Chem.*, 2007, **53**, 2029-2031.
202. F. Chen, P. Huang, Y. J. Zhu, J. Wu, C. L. Zhang and D. X. Cui, *Biomaterials*, 2011, **32**, 9031-9039.
203. V. Buissette, M. Moreau, T. Gacoin, J.-P. Boilot, J.-Y. Chane-Ching and T. Le Mercier, *Chem. Mater.*, 2004, **16**, 3767-3773.
204. Z. Fu and W. Bu, *Solid State Sci.*, 2008, **10**, 1062-1067.
205. J. Kim, A. de la Cotte, R. Deloncle, S. Archambeau, C. Biver, J.-P. Cano, K. Lahlil, J.-P. Boilot, E. Grelet and T. Gacoin, *Adv. Funct. Mater.*, 2012, **22**, 4949-4956.
206. J. Han, L. Wang and S. S. Wong, *RSC Adv.*, 2014, **4**, 34963-34980.
207. B. Li, Z. Cao, S. Wang, Q. Wei and Z. Shen, *Dalton Trans.*, 2018, **47**, 10288-10298.
208. J. Han, C. McBean, L. Wang, J. Hoy, C. Jaye, H. Liu, Z.-Q. Li, M. Y. Sfeir, D. A. Fischer, G. T. Taylor, J. A. Misewich and S. S. Wong, *Chem. Mater.*, 2015, **27**, 778-792.
209. Z. Wang, H. Liang, J. Wang, M. Gong and Q. Su, *Appl. Phys. Lett.*, 2006, **89**, 071921.
210. M. Minowa, K. Itakura, S. Moriyama and W. Ootani, *Nucl. Instrum. Methods Phys. Res.*, 1992, **A320**, 500-503.
211. S. Sekimoto, H. Nakagawaa, S. Okazaki and K. Fukuda, *Sens. Actuators*, 2000, **B66**, 142-145.
212. S. Okazaki, H. Nakagawa, S. Asakura, Y. Tomiuchi, N. Tsuji, H. Murayama and M. Washiya, *Sens. Actuators, B*, 2003, **93**, 142-147.
213. A. Kato, S. Oishi, T. Shishido, M. Yamazaki and S. Iida, *J. Phys. Chem. Solids*, 2005, **66**, 2079-2081.
214. G. Poirier, V. A. Jerez, C. B. de Araújo, Y. Messaddeq, S. J. L. Ribeiro and M. Poulain, *J. Appl. Phys.*, 2003, **93**, 1493-1497.
215. F. Amano, K. Nogami, R. Abe and B. Ohtani, *J. Phys. Chem. C*, 2008, **112**, 9320-9326.
216. J. Han, C. McBean, L. Wang, C. Jaye, H. Liu, D. A. Fischer and S. S. Wong, *J. Phys. Chem. C*, 2015, **119**, 3826-3842.
217. P. Huo, Y. Tang, M. Zhou, J. Li, Z. Ye, C. Ma, L. Yu and Y. Yan, *J. Ind. Eng. Chem.*, 2016, **37**, 340-346.
218. Q. Wang, Y. Shi, T. Niu, J. He, H. She and B. Su, *J. Sol-Gel Sci. Technol.*, 2017, **83**, 555-566.
219. W. Xua, C. Zheng, H. Hua, Q. Yanga, L. Chena, Y. Xia and C. Hua, *Appl. Surf. Sci.*, 2015, **327**, 140-148.
220. K. E. Pelcher, C. C. Milleville, L. Wangoh, S. Chauhan, M. R. Crawley, P. M. Marley, L. F. J. Piper, D. F. Watson and S. Banerjee, *Chem. Mater.*, 2015, **27**, 2468-2479.
221. C. Feldmann, T. Justel, C. R. Ronda and P. J. Schmidt, *Adv. Funct. Mater.*, 2003, **13**, 511-516.
222. T. S. Ahmadi, M. Haase and H. Weller, *Mater. Res. Bull.*, 2000, **35**, 1869-1879.
223. H. Liu, D. Moronta, L. Li, S. Yue and S. S. Wong, *Phys. Chem. Chem. Phys.*, 2018, **20**, 10086-10099.
224. M. Alejandro-Arellano, T. Ung, A. Blanco, P. Mulvaney and L. M. Liz-Marzan, *Pure Appl. Chem.*, 2000, **72**, 257-267.
225. A. Ulman, *Chem. Rev.*, 1996, **96**, 1533-1554.
226. E. Ruckenstein and Z. F. Li, *Adv. Coll. Interf. Sci.*, 2005, **113**, 43-63.

227. R. Makki, X. Ji, H. Mattoussi and O. Steinbock, *J. Am. Chem. Soc.*, 2014, **136**, 6463-6469.
228. X. Huang, Z. Fang, S. Kang, W. Peng, G. Dong, B. Zhou, Z. Ma, S. Zhou and J. Qiu, *J. Mater. Chem. C*, 2017, **5**, 7927-7934.
229. J. Müller, J. M. Lupton, A. L. Rogach, J. Feldmann, D. V. Talapin and H. Weller, *Phys Rev B*, 2005, **72**, 205339.
230. S. Asokan, K. M. Krueger, A. Alkhalil, A. R. Carreon, Z. Mu, V. L. Colvin, N. V. Mantzaris and M. S. Wong, *Nanotechnology*, 2005, **16**, 2000-2011.
231. M. V. Mukhina, A. S. Baimuratov, I. D. Rukhlenko, V. G. Maslov, F. Purcell Milton, Y. K. Gun'ko, A. V. Baranov and A. V. Fedorov, *ACS Nano*, 2016, **10**, 8904-8909.
232. H. Zahra, D. Elmaghroui, I. Fezai and S. Jaziri, *J. Appl. Phys.*, 2016, **120**, 205702.
233. K. Wu, W. E. Rodriguez-Cordoba, Z. Liu, H. Zhu and T. Lian, *ACS Nano*, 2013, **7**, 7173-7185.
234. D. V. Talapin, R. Koeppel, S. Gotzinger, A. Kornowski, J. M. Lupton, A. L. Rogach, O. Benson, J. Feldmann and H. Weller, *Nano Lett.*, 2003, **3**, 1677-1681.
235. A. N. Grennell, J. K. Utterback, O. M. Pearce, M. B. Wilker and G. Dukovic, *Nano Lett.*, 2017, **17**, 3764-3774.
236. P. K. Jain, L. Amirav, S. Aloni and A. P. Alivisatos, *J. Am. Chem. Soc.*, 2010, **132**, 9997-9999.
237. H. Li, R. Brescia, R. Krahne, G. Bertoni, M. J. P. Alcocer, C. D'Andrea, F. Scotognella, F. Tassone, M. Zanella, M. D. Giorgi and L. Manna, *ACS Nano*, 2012, **6**, 1637-1647.
238. K. Wu, Z. Chen, H. Lv, H. Zhu, C. L. Hill and T. Lian, *J. Am. Chem. Soc.*, 2014, **136**, 7708-7716.
239. K. Wu, H. Zhu and T. Lian, *Acc. Chem. Res.*, 2015, **48**, 851-859.
240. H. Zhu, Z. Chen, K. Wu and T. Lian, *Chem. Sci.*, 2014, **5**, 3905-3914.
241. A. E. Saunders, B. Koo, X. Wang, C. K. Shih and B. A. Korgel, *ChemPhysChem*, 2008, **9**, 1158-1163.
242. S. Kumar, M. Jones, S. S. Lo and G. D. Scholes, *Small*, 2007, **3**, 1633-1639.
243. B. A. K. Bonil Koo, *Nano Lett.*, 2008, **8**, 2490-2496.
244. M. Kirsanova, A. Nemchinov, N. N. Hewa-Kasakarage, N. Schmall and M. Zamkov, *Chem. Mater.*, 2009, **21**, 4305-4309.
245. N. N. Hewa-Kasakarage, M. Kirsanova, I. Nemitz, P. Z. El-Khoury, A. Nemchinov and M. Zamkov, *ACS Nano*, 2010, **4**, 1837-1844.
246. N. Oh, S. Nam, Y. Zhai, K. Deshpande, P. Trefonas and M. Shim, *Nat. Commun.*, 2014, **5**, 3642.
247. L. F. Carrette, K. A. Friedrich, U. Stimming, *ChemPhysChem*, 2000, **1**, 162-193.
248. S. Yue, Y. Zhou, S. Zou, L. Wang, H. Liu and S. S. Wong, *Adv. Opt. Mater.*, 2017, **5**, 1700089.
249. C. Tan and H. Zhang, *J. Am. Chem. Soc.*, 2015, **137**, 12162-12174.
250. M.-Y. Li, Y. Shi, C.-C. Cheng, L.-S. Lu, Y.-C. Lin, H.-L. Tang, M.-L. Tsai, C.-W. Chu, K.-H. Wei, J.-H. He, W.-H. Chang, K. Suenaga and L.-J. Li, *Science*, 2015, **349**, 524-528.
251. B. Jin, P. Huang, Q. Zhang, X. Zhou, X. Zhang, L. Li, J. Su, H. Li and T. Zhai, *Adv. Funct. Mater.*, 2018, **28**, 1800181.
252. C. Tan, J. Chen, X.-J. Wu and H. Zhang, *Nat. Rev. Mater.*, 2018, **3**, 17089.
253. Z. Fang, Y. Liu, Y. Fan, Y. Ni, X. Wei, K. Tang, J. Shen and Y. Chen, *J. Phys. Chem. C*, 2011, **115**, 13968-13976.

254. D. J. Milliron, S. M. Hughes, Y. Cui, L. Manna, J. Li, L.-W. Wang and A. P. Alivisatos, *Nature*, 2004, **430**, 190-195.
255. W. van der Stam, E. Bladt, F. T. Rabouw, S. Bals and C. de Mello Donega, *ACS Nano*, 2015, **9**, 11430-11438.
256. Y. Li, A. Tang, Z. Liu, L. Peng, Y. Yuan, X. Shi, C. Yang and F. Teng, *Dalton Trans.*, 2018, **47**, 67-73.
257. S. D. Jackson, *Opt. Lett.*, 2003, **28**, 2192-2194.
258. L. P. Singh, S. K. Srivastava, R. Mishra and R. S. Ningthoujam, *J. Phys. Chem. C*, 2014, **118**, 18087-18096.
259. H. Liu, J. Han, C. McBean, C. S. Lewis, P. Kumar Routh, M. Cotlet and S. S. Wong, *Phys. Chem. Chem. Phys.*, 2017, **19**, 2153-2167.
260. P. Feng, Y. Pan and H. Ye, *RSC Adv.*, 2018, **8**, 35306-35313.
261. Z. Xu, C. Li, P. Yang, C. Zhang, S. Huang and J. Lin, *Cryst. Growth Des.*, 2009, **9**, 4752-4758.
262. J. Yang, Y. Deng, Q. Wu, J. Zhou, H. Bao, Q. Li, F. Zhang, F. Li, B. Tu and D. Zhao, *Langmuir*, 2010, **26**, 8850-8856.
263. Y. Wu, C. Li, D. Yang and J. Lin, *J. Colloid Interface Sci.*, 2011, **354**, 429-436.
264. Y. Zhang, D. Geng, X. Kang, M. Shang, Y. Wu, X. Li, H. Lian, Z. Cheng and J. Lin, *Inorg. Chem.*, 2013, **52**, 12986-12994.
265. G. Murali, R. K. Mishra, J. M. Lee, Y. C. Chae, J. Kim, Y. D. Suh, D.-k. Lim and S. H. Lee, *Cryst. Growth Des.*, 2017, **11**, 3055-3061.
266. P. R. Brown, D. Kim, R. B. Lunt, N. Zhao, M. G. Bawendi, J. C. Grossman and V. Bulovic, *ACS Nano*, 2014, **8**, 5863-5872.
267. J. T. Margraf, A. Ruland, V. Sgobba, D. M. Guldi and T. Clark, *Langmuir*, 2013, **29**, 2434-2438.
268. C. F. Cai, B. P. Zhang, R. F. Li, H. Z. Wu, T. N. Xu, W. H. Zhang and J. F. Zhu, *Eur. Biophys. J.*, 2012, **99**, 37010.
269. R. Li, C. Cai, L. Hu, H. Wu, W. Zhang and J. Zhu, *Appl. Surf. Sci.*, 2013, **276**, 258-261.
270. J. Huang, D. Stockwell, h. Huang, D. L. Mohler and T. Lian, *J. Am. Chem. Soc.*, 2008, **130**, 5632-5633.
271. K. Tvrđy, P. A. Frantsuzov and P. V. Kamat, *Proc. Natl. Acad. Sci. U. S. A.*, 2011, **108**, 29-34.
272. R. J. Ellingson, M. C. Beard, J. C. Johnson, P. Yu, O. I. Micic, A. J. Nozik, A. Shabaev and A. L. Efros, *Nano Lett.*, 2005, **5**, 865-871.
273. M. Ben-Lulu, D. Mocatta, M. Bonn, U. Banin and S. Ruhman, *Nano Lett.*, 2008, **8**, 1207-1211.
274. L. Wang, H.-Y. Wang, B.-R. Gao, L.-Y. Pan, Y. Jiang, Q.-D. Chen, W. Han and H.-B. Sun, *IEEE J. Quantum Electron.*, 2011, **47**, 1177-1184.
275. Y. Zeng and D. F. Kelley, *J. Phys. Chem. C*, 2017, **121**, 16657-16664.
276. C. Cao, G. Zhang, J. Ye, Z. Sun, R. Hua and J. Cui, *J. Mater. Sci.: Mater. Electron.*, 2017, **29**, 1123-1130.
277. A. Boulesbaa, K. Wang, M. Mahjouri-Samani, M. Tian, A. A. Puretzky, I. Ivanov, C. M. Rouleau, K. Xiao, B. G. Sumpter and D. B. Geohegan, *J. Am. Chem. Soc.*, 2016, **138**, 14713-14719.
278. H. Zang, P. K. Routh, Y. Huang, J. S. Chen, E. Sutter, P. Sutter and M. Cotlet, *ACS Nano*, 2016, **10**, 4790-4796.

279. H. Staleva and G. V. Hartland, *Adv. Funct. Mater.*, 2008, **18**, 3809-3817.
280. C. R. Carey, Y. Yu, M. Kuno and G. V. Hartland, *J. Phys. Chem. C*, 2009, **113**, 19077-19081.
281. G. V. Hartland, *Chem. Sci.*, 2010, **1**, 303-309.
282. M. Law, L. E. Greene, J. C. Johnson, R. Saykally and P. Yang, *Nat. Mater.*, 2005, **4**, 455-459.
283. B. Bai, D. Kou, W. Zhou, Z. Zhou and S. Wu, *Green Chem.*, 2015, **17**, 4377-4382.
284. R. Hardman, *Environ. Health Perspect.*, 2006, **114**, 165-172.
285. B. A. Rzigalinski and J. S. Strobl, *Toxicol. Appl. Pharmacol.*, 2009, **238**, 280-288.
286. C.-W. Lam, J. T. James, R. McCluskey and R. L. Hunter, *Toxicol. Sci.*, 2004, **77**, 126-1347.
287. L. Wang, H. Liu, R. M. Konik, J. A. Misewich and S. S. Wong, *Chem. Soc. Rev.*, 2013, **42**, 8134-8156.

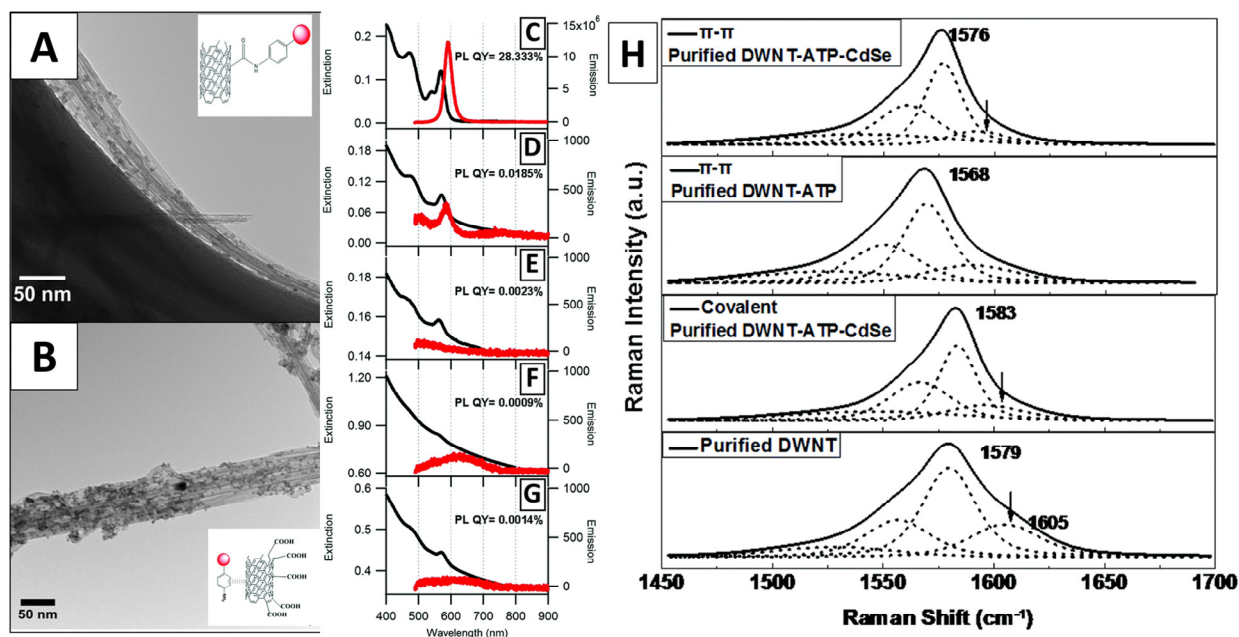


Figure 1. (A, B) TEM images of DWNT-4-ATP-capped CdSe QD heterostructures synthesized by covalent attachment and π - π stacking, non-covalent methods, respectively. Inset figures highlight the expected chemical bonding configuration, associated with each protocol. (C-G) Extinction (black curves) and emission (red curves, excited at 415 nm) spectra for (C) CdSe QDs, (D) 4-ATP-capped CdSe QDs, (E) pristine DWNT-ATP-capped CdSe QD heterostructures fabricated through a non-covalent π - π stacking protocol, and purified DWNT-ATP-capped CdSe QD heterostructures synthesized using both (F) non-covalent and (G) covalent techniques. (H) Raman spectra, measured at an excitation wavelength of 514 nm (2.14 eV) and accompanying G-band analysis of not only purified DWNTs (in the presence and absence of ATP attachment), but also purified DWNT-4-ATP-capped CdSe QD heterostructures generated both covalently and non-covalently. Adapted from L. Wang, J. Han, J. Hoy, F. Hu, H. Liu, M. M. Gentleman, M. Y. Sfeir, J. A. Misewich, and S. S. Wong, *Dalton Trans.*, **2014**, 43, 7480-7490 with permission from The Royal Society of Chemistry.

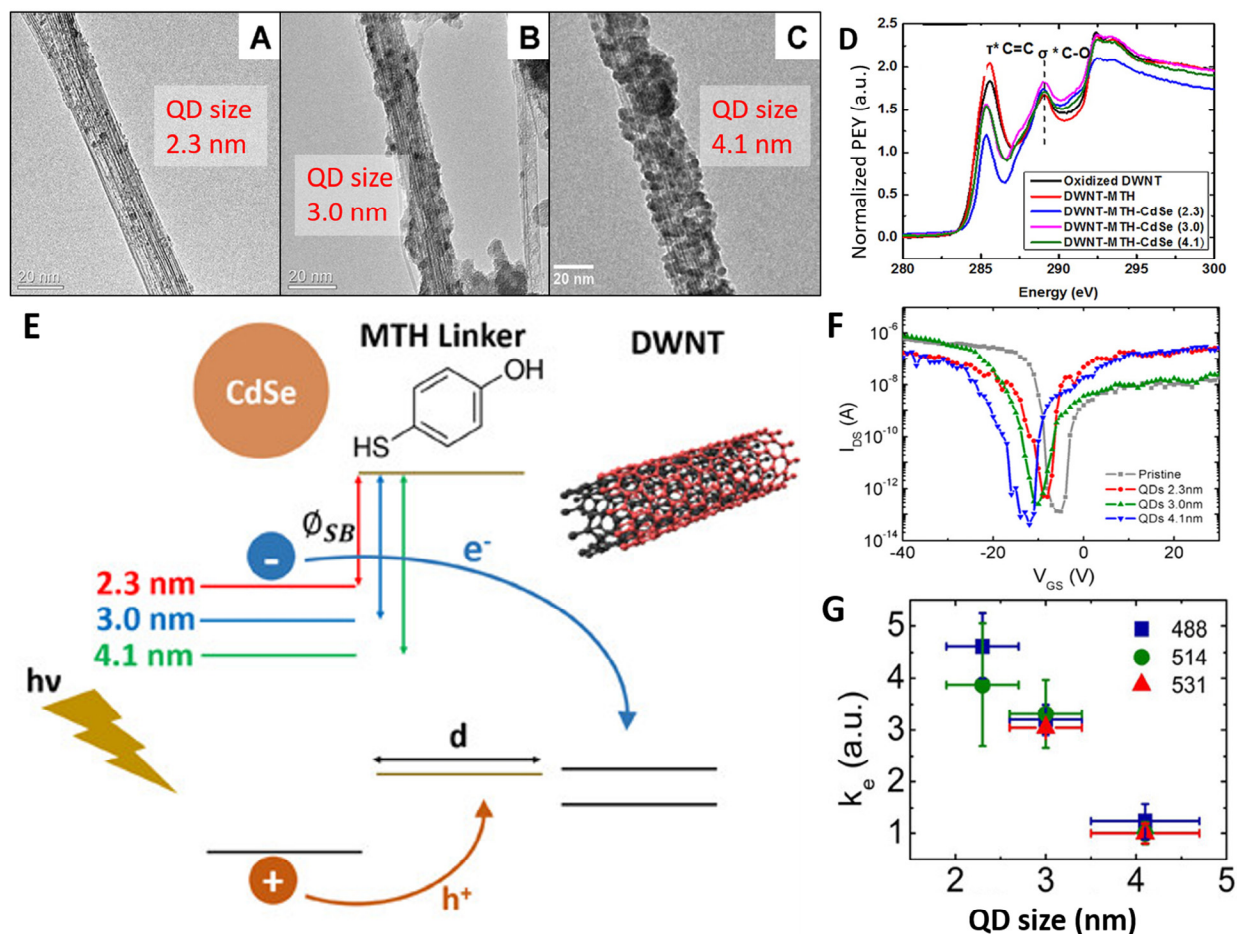


Figure 2. (A-C) TEM images of DWNT-MTH-capped CdSe QD (with average constituent QD diameters of 2.3, 3.0, and 4.1 nm, respectively) heterostructures, synthesized using a non-covalent π - π stacking methodology. (D) C K-edge spectra of oxidized DWNTs (black), DWNT-MTH composite control samples (red), and DWNT-MTH-capped CdSe QD (with constituent QD average diameters of 2.3 nm (blue), 3.0 nm (pink), and 4.1 nm (green)) heterostructures, respectively. (E) The schematic illustrates how we envision electrons tunneling from a CdSe QD possessing varying sizes to the adjoining DWNTs, mediated by the presence of the ligand. Smaller QD sizes tend to give rise to smaller tunneling barriers. The HOMO and LUMO levels shown in the Figure are merely qualitative representations of their relative positions. (F) Representative transfer characteristics for various DWNT devices, generated both with and without functionalization. (G) Extracted charge transfer efficiency (k_e) values for different QD sizes and at various laser excitation wavelengths (i.e., 488, 514, and 531 nm), assuming that the coverage density and the number of transferred electrons (Δn) are totally correlated variables. Panels A-D were adapted with permission from L. Wang, J. Han, Y. Zhu, R. Zhou, C. Jaye, H. Liu, Z.-Q. Li, G. T. Taylor, D. A. Fischer, J. Appenzeller and S. S. Wong, *J. Phys. Chem. C*, **2015**, *119*(47), 26327-26338. Copyright 2015 American Chemical Society. Panels E-G were adapted with permission from Y. Zhu, R. Zhou, L. Wang, S. S. Wong, and J. Appenzeller, *ACS Energy Lett.*, **2017**, *2* (3), 717-725. Copyright 2017 American Chemical Society.

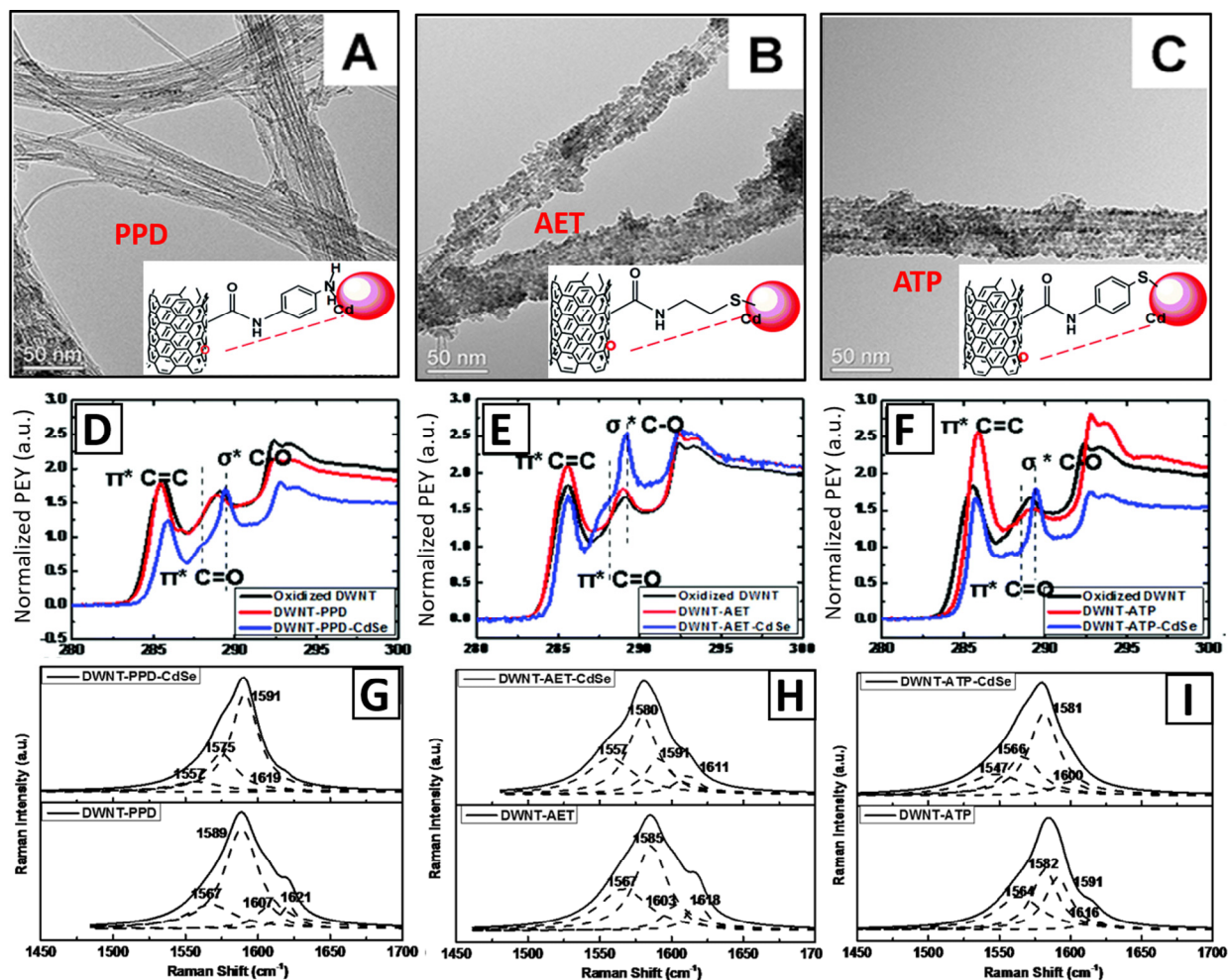


Figure 3. (A-C) TEM images of DWNT-PPD- capped CdSe QD, DWNT-AET-capped CdSe QD, and DWNT-ATP-capped CdSe QD heterostructures, respectively, synthesized by an amide-mediated covalent attachment strategy. The inset images denote the chemical structures of the various as-synthesized heterostructures, respectively. (D-F) C K-edge spectra of DWNT-ligand-capped CdSe QD systems. The ligands tested included PPD, AET, and ATP, respectively. (G-I) Raman G-band spectra, measured at an excitation wavelength of 514 nm (2.41 eV), of the three as-prepared heterostructures, associated with the previous figures, by comparison with their respective controls. Adapted from L. Wang, J. Han, B. Sundahl, S. Thornton, Y. Zhu, R. Zhou, C. Jaye, H. Liu, Z. Q. Li, G. T. Taylor, D. A. Fischer, J. Appenzeller, R. J. Harrison, and S. S. Wong, *Nanoscale*, **2016**, *8*, 15553-15570 with permission from The Royal Society of Chemistry.

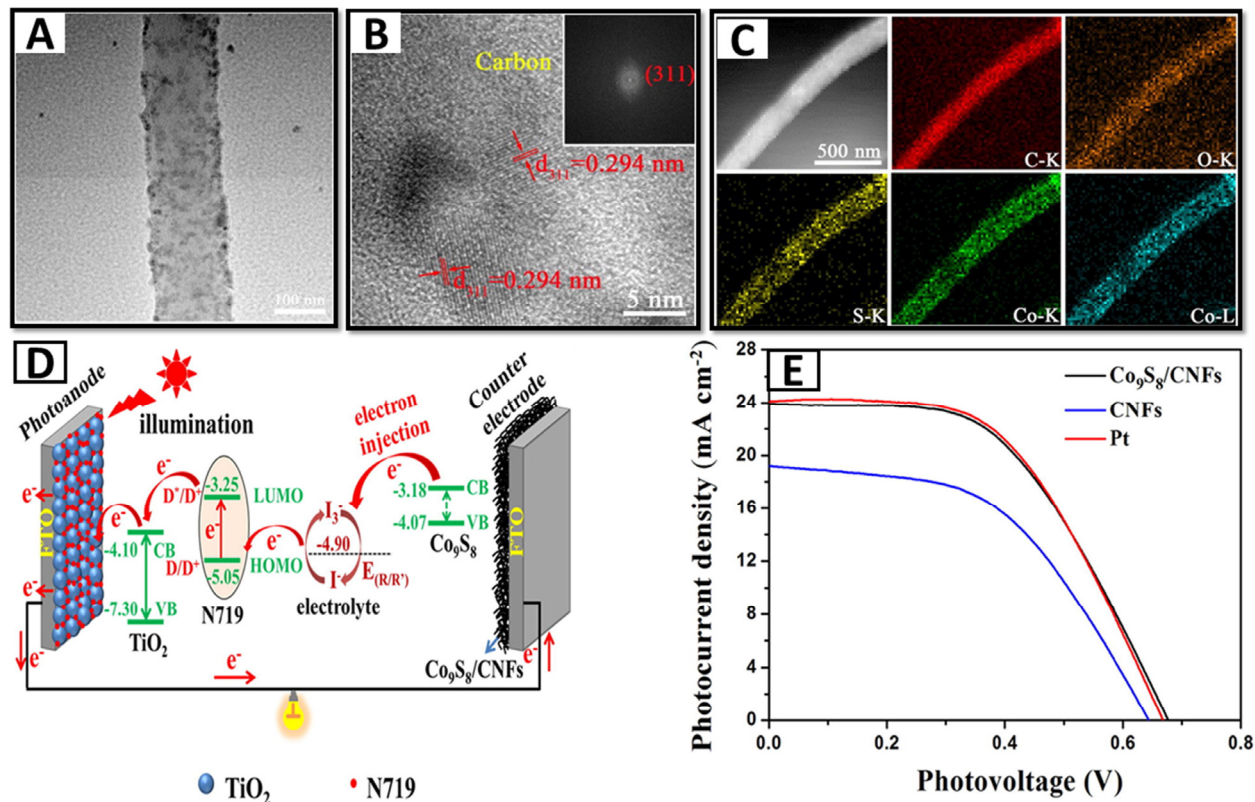


Figure 4. (A-B) Representative TEM and HRTEM images of as-prepared 0D/1D Co₉S₈/CNF composite, respectively. (C) HAADF-STEM and associated EDX mapping results for a typical Co₉S₈/CNF composite heterostructure. (D) Schematic diagram of the working principle of the DSSC fabricated using the hybrid as the counter electrode. (E) Photocurrent density-photovoltage (J-V) curves measured for the DSSCs with the Co₉S₈/CNFs composite, Pt, and pure CNFs, respectively, as counter electrodes. Adapted from Ju Qiu, Dayong He, Rui Zhao, Bolun Sun, He Ji, Nan Zhang, Yanzi Li, Xiaofeng Lu, and Ce Wang, *J. Colloid Interface Sci.*, **2018**, 522, 95-103. Copyright, with permission from Elsevier.

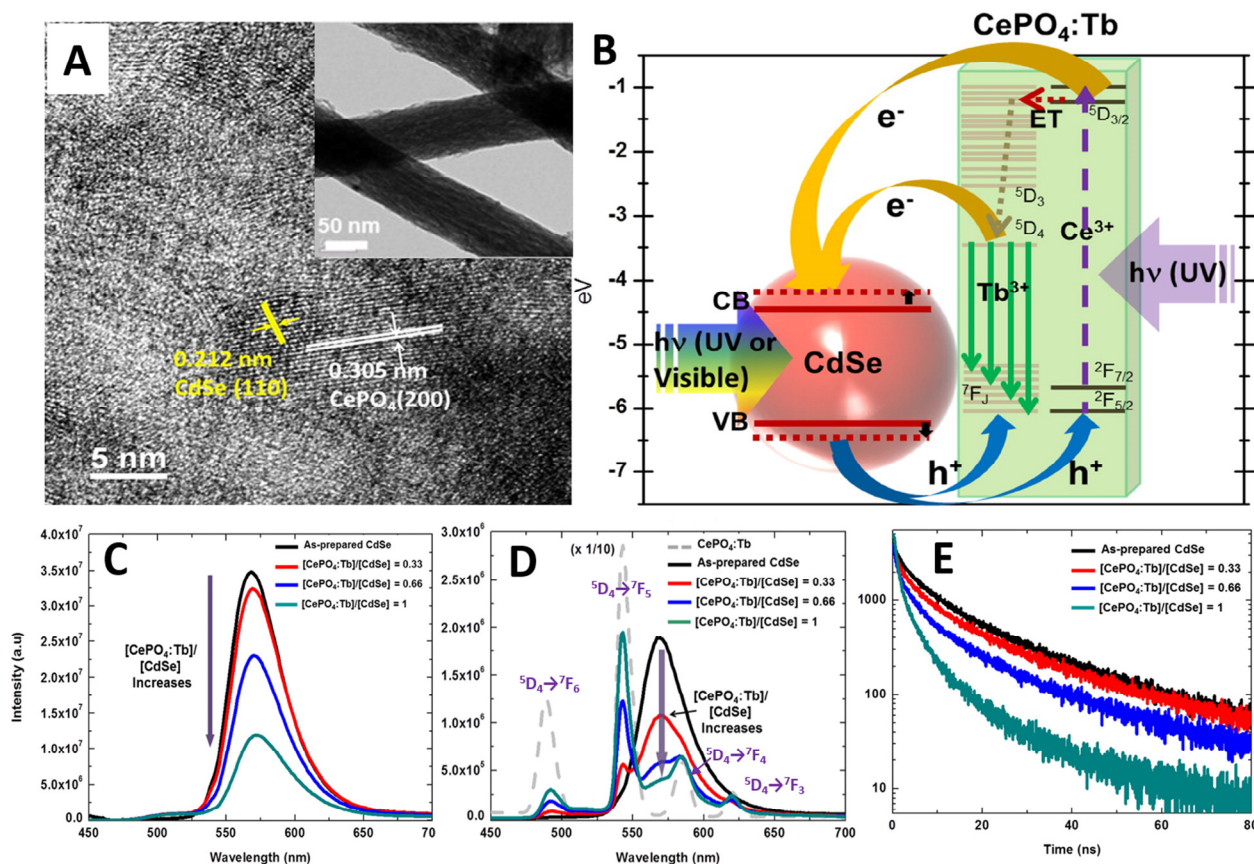


Figure 5. (A) HRTEM image of CdSe QD - CePO₄: Tb heterostructures. The inset corresponds to the TEM image of these heterostructures, obtained at low magnification. (B) Electronic energy level diagram of CdSe QD-CePO₄: Tb heterostructures. Viable charge transfer pathways for these materials are shown. (C and D) PL emission spectra of CdSe QD-CePO₄: Tb heterostructures prepared at various concentration ratios of [CePO₄: Tb]/[CdSe] (namely at 0.33, 0.66, and 1, respectively) and excited at (C) 375 nm and (D) 280 nm, respectively. (E) PL decay curves ($\lambda_{\text{ex}} = 388$ nm) associated with the excitonic emission of CdSe QD-CePO₄: Tb heterostructures prepared, from top to bottom, at increasing concentration ratios of [CePO₄: Tb]/[CdSe], used to synthesize these various nanoscale composites. Adapted with permission from J. Han, L. Wang, and S. S. Wong, *J. Phys. Chem. C*, **2014**, *118*(11), 5671–5682. Copyright 2014 American Chemical Society.

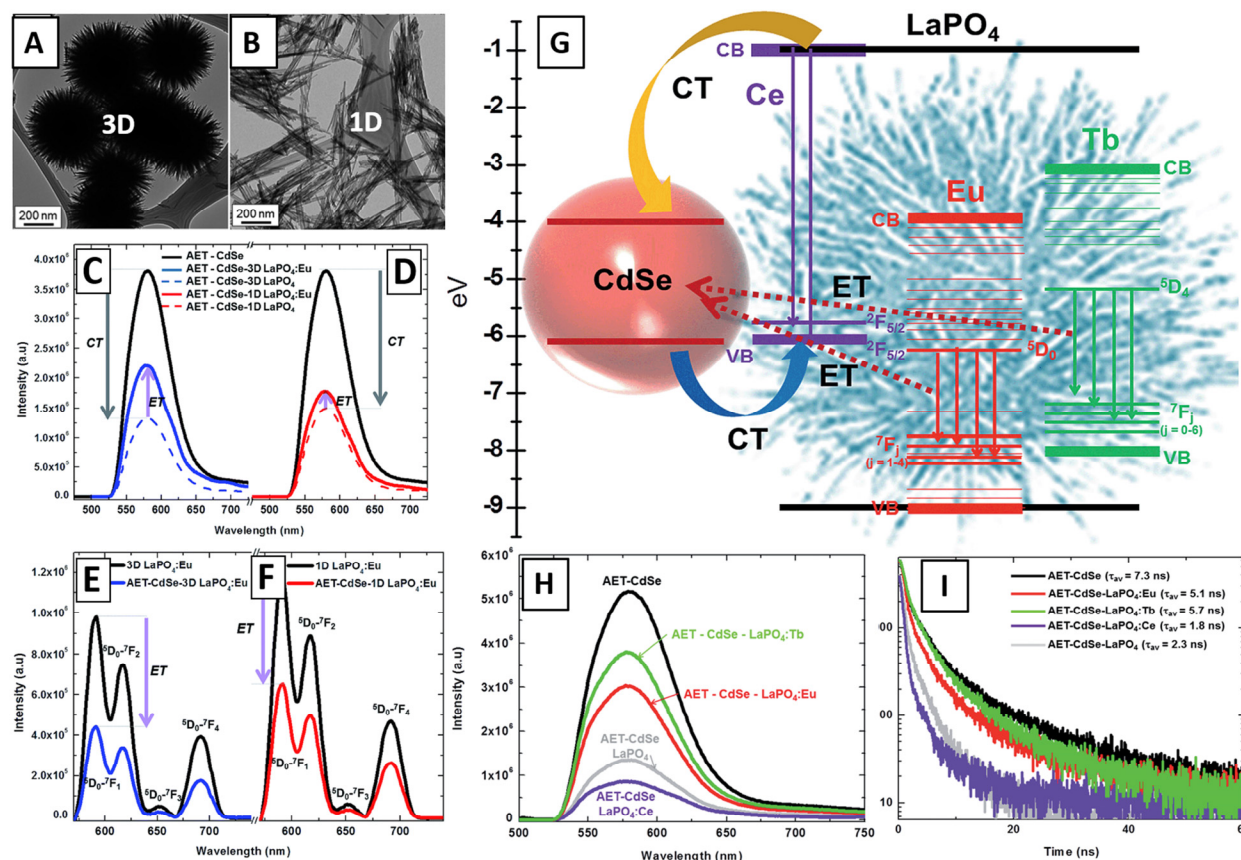


Figure 6. (A, B) Representative TEM images of $\text{LaPO}_4: \text{Eu}$ 3D urchin-like architectures and 1D nanowires, respectively. (C-F) PL emission spectra of AET-capped CdSe QDs, AET-capped CdSe QD-3D $\text{LaPO}_4: \text{Eu}$ urchin-like heterostructures, and undoped AET-capped CdSe QD-3D $\text{LaPO}_4: \text{Eu}$ urchin-like heterostructures, respectively, under (C) 380 nm and (E) 260 nm excitation, respectively. PL emission spectra of AET-capped CdSe QDs, AET-capped CdSe QD-1D $\text{LaPO}_4: \text{Eu}$ heterostructures, and undoped AET-capped CdSe QD-1D LaPO_4 heterostructures, acquired under (D) 380 nm and (F) 260 nm excitation, respectively. (G) Electronic energy diagram describing the various energy band alignments associated with heterostructures composed of CdSe QDs attached onto LaPO_4 , $\text{LaPO}_4: \text{Ce}$, $\text{LaPO}_4: \text{Eu}$, and $\text{LaPO}_4: \text{Tb}$, respectively. (H) PL emission spectra of AET-capped CdSe QDs as well as of AET-capped CdSe QDs coupled with either LaPO_4 , $\text{LaPO}_4: \text{Eu}$, $\text{LaPO}_4: \text{Tb}$, or $\text{LaPO}_4: \text{Ce}$ as components of 3D-urchin-based heterostructures, excited at 380 nm. (I) PL decay curves ($\lambda_{\text{ex}}=388 \text{ nm}$) associated with the excitonic emission of AET-capped CdSe QDs within heterostructures, composed of AET-capped CdSe QDs, coupled with 3D motifs of LaPO_4 , $\text{LaPO}_4: \text{Ce}$, $\text{LaPO}_4: \text{Eu}$, and $\text{LaPO}_4: \text{Tb}$, respectively. Adapted from J. Han, L. Wang, and S. S. Wong, *RSC Adv.*, **2014**, *4*, 34963-34980 with permission from The Royal Society of Chemistry.

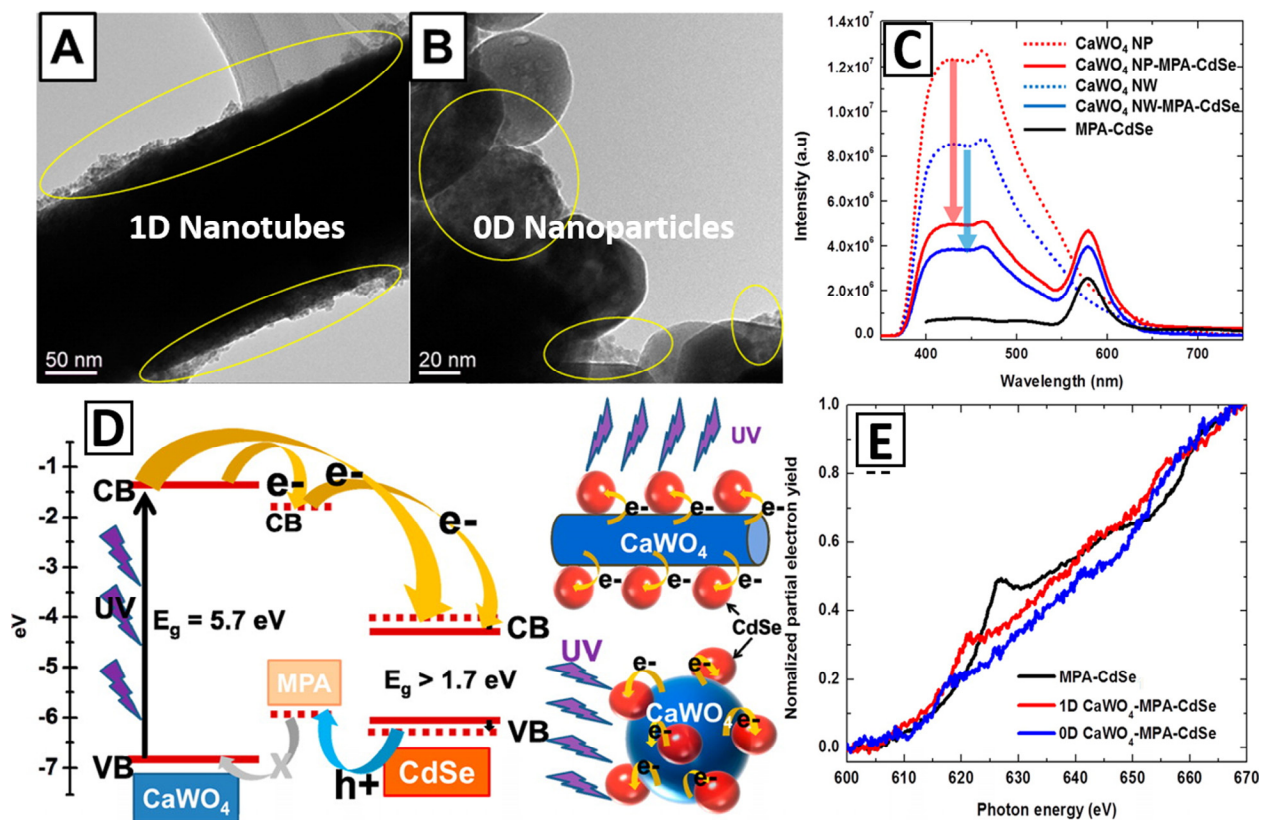


Figure 7. (A, B) Representative TEM images associated with the formation of CaWO₄ 1D/0D-MPA-capped CdSe QD heterostructures, respectively. Yellow circles highlight regions pertaining to CdSe QDs. (C) PL emission spectra of 1D CaWO₄-MPA-capped CdSe QD heterostructures prepared at various concentration ratios of [CdSe QDs]/[CaWO₄], excited at 260 nm. (D) Electronic energy diagram of CaWO₄-MPA-capped CdSe QD heterostructures and the corresponding plausible charge transfer schematics governing these materials. (E) Cd M_{2,3} edge partial electron yield spectra of both 1D/0D CaWO₄-MPA-capped CdSe 0D QD heterostructures as well as of MPA-capped CdSe QDs. Adapted with permission from J. Han, C. McBean, L. Wang, J. Hoy, C. Jaye, H. Liu, Z.-Q. Li, M. Y. Sfeir, D. A. Fischer, G. T. Taylor, J. A. Misewich, and S. S. Wong, *Chem. Mater.*, **2015**, 27(3), 778–792. Copyright 2015 American Chemical Society.

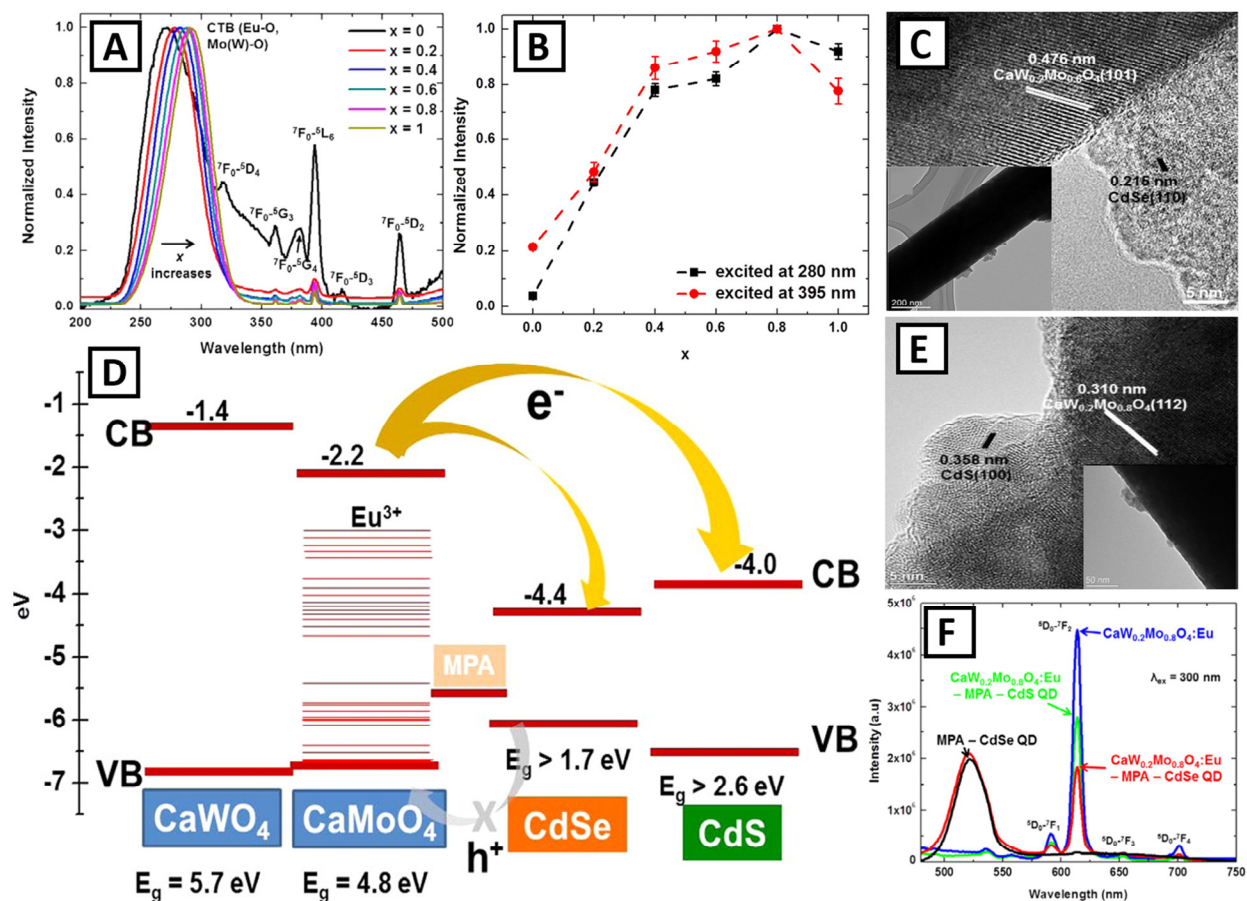


Figure 8. (A) PL excitation spectra of nanowires of as-prepared 1D $\text{CaW}_{1-x}\text{Mo}_x\text{O}_4:\text{Eu}^{3+}$ (“x”=0, 0.2, 0.4, 0.6, 0.8, and 1). (B) Normalized PL emission intensity of the Eu^{3+} emission in $\text{CaW}_{1-x}\text{Mo}_x\text{O}_4:\text{Eu}^{3+}$ as a function of increasing “x” under both 280 nm and 395 nm excitation conditions. (C and E) Representative HRTEM images and the corresponding TEM images (inset), associated with the formation of $\text{CaW}_{0.2}\text{Mo}_{0.8}\text{O}_4:\text{Eu}^{3+}$ -(0D CdSe or CdSe QD) heterostructures, respectively. (D) Electronic energy diagram schematic, describing plausible electronic interactions within CaWO_4 - $\text{CaMoO}_4:\text{Eu}^{3+}$ -MPA-capped CdS QD heterostructures and the corresponding CaWO_4 - $\text{CaMoO}_4:\text{Eu}^{3+}$ -MPA-capped CdSe QD heterostructures. (F) PL emission spectra of $\text{CaW}_{0.2}\text{Mo}_{0.8}\text{O}_4:\text{Eu}^{3+}$ -CdS QD heterostructures, $\text{CaW}_{0.2}\text{Mo}_{0.8}\text{O}_4:\text{Eu}^{3+}$ -CdSe QD heterostructures, $\text{CaW}_{0.2}\text{Mo}_{0.8}\text{O}_4:\text{Eu}^{3+}$ nanowires, and MPA-capped CdSe QDs, excited at a wavelength of 300 nm. Adapted with permission from J. Han, C. McBean, L. Wang, C. Jaye, H. Liu, D. A. Fischer, and S. S. Wong, *J. Phys. Chem. C.*, **2015**, *119*(7), 3826-3842. Copyright 2015 American Chemical Society.

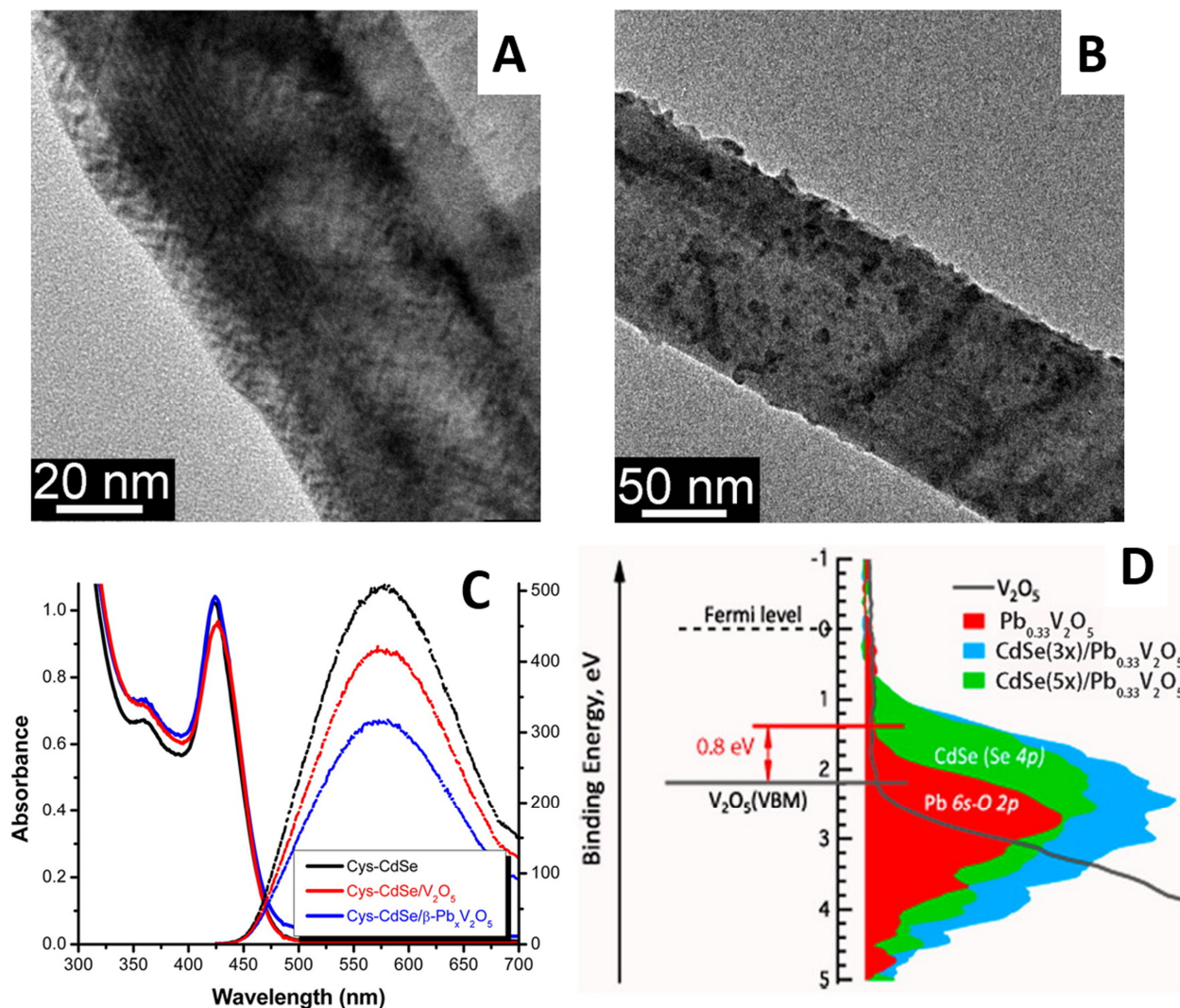


Figure 9. TEM images of β - $\text{Pb}_x\text{V}_2\text{O}_5$ nanowires coated with CdSe QDs via (A) a linker-assisted assembly method and (B) via three SILAR cycles. (C) Absorption (solid) and emission (dashed) spectra of cysteine-capped CdSe (Cys-CdSe) QDs, mixed dispersions of Cys-CdSe QDs coupled to V_2O_5 nanowires, and mixed dispersions of Cys-CdSe QDs linked with β - $\text{Pb}_x\text{V}_2\text{O}_5$ nanowires. (D) Illustration of binding energies of V_2O_5 , $\text{Pb}_{0.33}\text{V}_2\text{O}_5$, and CdSe- $\text{Pb}_{0.33}\text{V}_2\text{O}_5$ characterized by different coverage ratios. Adapted from K. E. Pelcher, C. C. Milleville, L. Wangoh, S. Chauhan, M. R. Crawley, P. M. Marley, L. F. J. Piper, D. F. Watson, and S. Banerjee, *Chem. Mater.*, **2015**, 27 (7), 2468–2479. Copyright (2018) American Chemical Society.

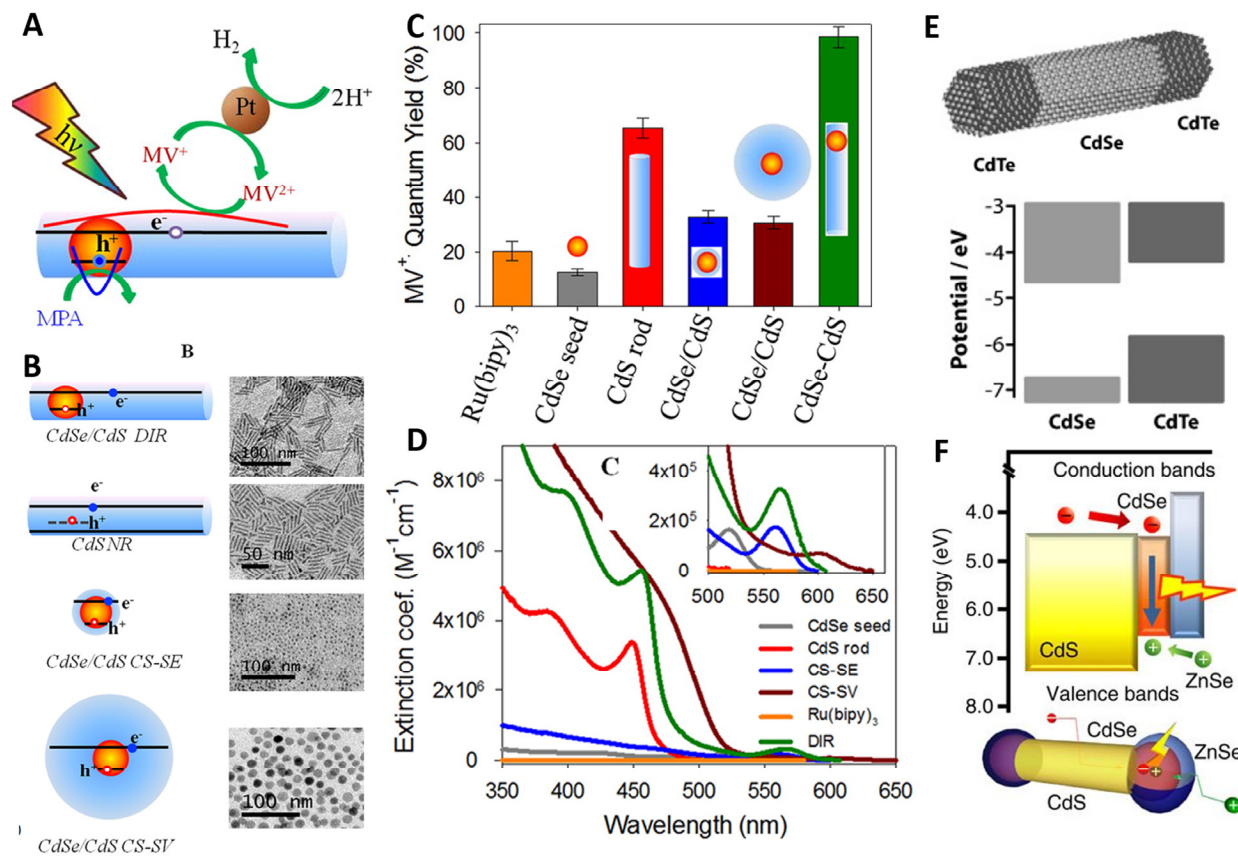


Figure 10. (A) Schematic depiction of relevant processes in a light-driven reduction of methylviologen (MV^{2+}) with colloidal quasi-type II CdSe/CdS dot-in-rod nanorods as a light absorber and charge separator and mercaptopropionic acid as a sacrificial electron donor. (B) Schematic structure and TEM images of CdSe/CdS dot-in-rod (DIR) nanorods (NRs) as well as of CdS NRs of similar dimensions, CdSe/CdS core/shell QDs of similar lowest exciton energy (CS-SE), and CdSe/CdS core/shell QDs of similar volume (CS-SV) as the DIR. The horizontal lines in the schematic structures indicate the extent of delocalization of the lowest energy conduction band electron and valence band hole. (C) Initial quantum yields of MV^{+} radical generation using different sensitizers with the schematic structure of each, as shown. (D) Extinction coefficient spectra of CdSe/CdS DIR, CdSe seed, CdS NR, CdSe/CdS CS-SE, CdSe/CdS CS-SV, and $Ru(bipy)_3^{2+}$, with the inset figure highlighting the expanded view of the lowest energy exciton bands. (E) Illustration of a linear CdTe/CdSe/CdTe heterostructure nanorods. The conduction and valence band offsets for bulk CdSe and bulk CdTe form a type-II (staggered) alignment. (F) Energy band diagram and schematic of the geometric structure of double-heterojunction nanorods, consisting of a type II staggered band offset CdS and ZnSe, both in contact with the smaller band gap emitting CdSe quantum dot. Panels A-D adapted from H. Zhu, N. Song, H. Lv, H. Zhu, C. L. Hill and T. Lian, *J. Am. Chem. Soc.*, **2012**, *134* (28), 11701–11708. Copyright (2018) American Chemical Society. Panel E adapted with permission from A. E. Saunders, B. Koo, X. Wang, C. K. Shih, and B. A. Korgel, *Chemphyschem.* **2008**, *9*, 1158-1163. Copyright © 2008 WILEY-VCH Verlag GmbH & Co. KGaA, Weinheim. Panel F

adapted with permission from N. Oh, S. Nam, Y. Zhai, K. Deshpande, P. Trefonas, and M. Shim, *Nat Commun.* **2014**, *5*, 3642. Copyright © 2014 Macmillan Publishers Limited.

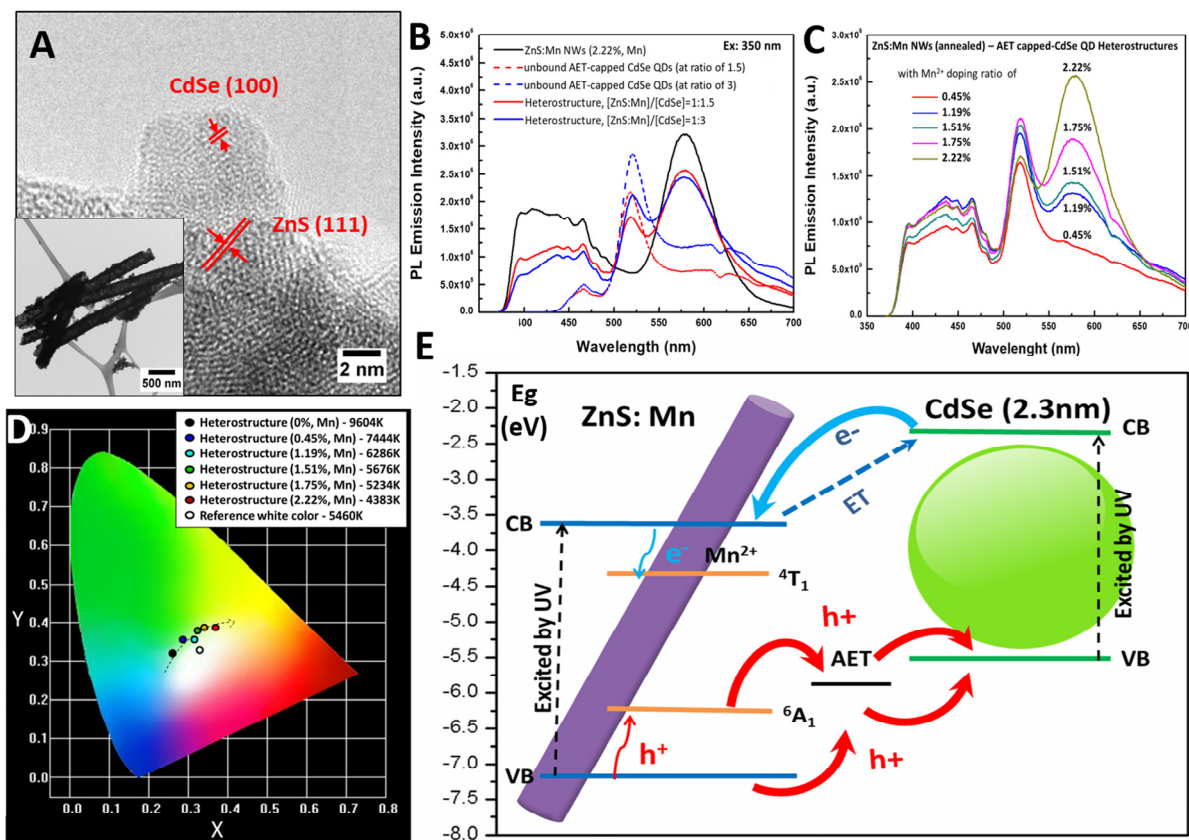


Figure 11. (A) HRTEM image and associated TEM image (inset) for ZnS: Mn²⁺ NW-AET-capped CdSe QD heterostructures. (B) PL emission spectra of ZnS: Mn²⁺ NW-AET-capped CdSe QD heterostructures, possessing [ZnS: Mn²⁺]: [AET-capped CdSe QD] ratios of 1:1.5 (red) and 1:3 (blue), respectively. (C) PL emission spectra of ZnS: Mn²⁺ NW-AET-capped CdSe QD heterostructures, associated with a series of actual Mn²⁺ doping ratios of 0%, 0.45%, 1.19%, 1.51%, and 2.22%, respectively. (D) CIE chromaticity diagram of corresponding ZnS: Mn²⁺ NW-AET-capped CdSe QD heterostructures (molar ratio of 1:1.5) with actual Mn²⁺ doping ratio of 0% (black), 0.45% (blue), 1.19% (cyan), 1.51% (green), 1.75% (yellow), and 2.22% (red), respectively. (E) Diagram of energy level alignments of ZnS: Mn²⁺ NW-AET-capped CdSe QD heterostructures with labeled charge transfer pathways as well as possible energy transfer channels. Adapted with permission from S. Yue, Y. Zhou, S. Zou, L. Wang, H. Liu, and S. S. Wong, *Adv. Optical Mater.*, **2017**, 5(20), 1700089. Copyright © 2017 WILEY-VCH Verlag GmbH & Co. KGaA, Weinheim.

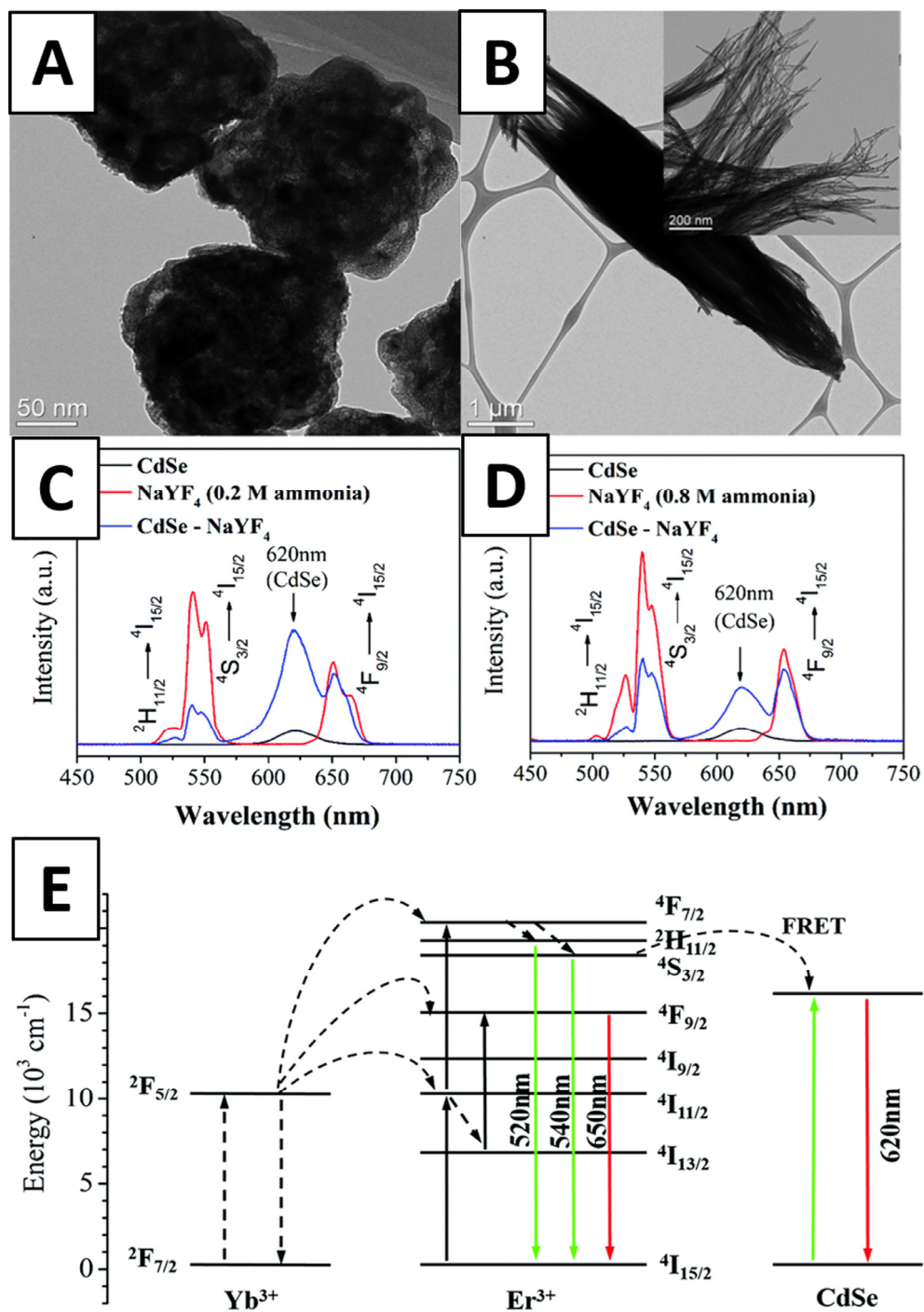


Figure 12. (A, B) Representative TEM images of α -phase nanoscale spheres and β -phase nanowire bundles (with a higher resolution TEM image (inset)), respectively. (C) Upconversion data associated with heterostructures composed of CdSe QDs attached onto 0D NaYF₄ nanoscale sphere samples. (D) Upconversion data associated with heterostructures composed of CdSe QDs attached onto samples of 1D NaYF₄ nanowire bundles. (E) Electronic energy diagram associated with CdSe QD-NaYF₄ heterostructures. Adapted from H. Liu, J. Han, C. McBean, C. S. Lewis,

P. Kumar Routh, M. Cotlet, and S. S. Wong, *Phys. Chem. Chem. Phys.*, **2017**, *19*, 2153- 2167
with permission from The Royal Society of Chemistry.

| Underlying 1D Platform | Parameter Tested and/or Reaction Variable Analyzed with Intended Structure and Application | Chemical Composition | Key Concept Tested | Further Elaboration and Details on Crucial Idea Tested | Effect on Applications |
|------------------------|--|----------------------|--|--|---|
| Carbon Nanotubes | Attachment protocol | CdSe-DWNTs | Covalent attachment | ATP as linker | Less efficient charge transfer |
| | | | Non-covalent attachment | ATP with π - π stacking | More efficient charge transfer |
| | | CdSe-MWNTs | Ligand-free method | Ligand exchange by ultrasonication | Fast charge transfer |
| | | CdSe-fMWNTs | Presence or absence of functional CNTs | Carboxylic functional groups | Enhanced attachment |
| | | PbSe-SWNTs | In situ growth | Non-covalent linkage | Effective size control |
| | QD size and coverage variation | CdSe-DWNTs | 2.3 nm | Lowest coverage | Larger driving force for charge transfer |
| | | | 3.0 nm | Medium coverage | Mediocre effects on charge transfer |
| | | | 4.1 nm | Highest coverage | Smaller driving force for charge transfer |
| | | CdTe-MWNTs | Different QD coverages | Higher density | Improved charge transfer |

| | | | | | |
|-------------------|----------------|--------------------------------------|-----------------------------------|------------------------------------|--|
| | | CdS-MWNTs | QD loading | Pollutant degradation efficiency | Higher activity with higher loading |
| | | CdSe-MWNTs | 2.49 to 3.06 nm | Larger sizes | More charge transfer noted |
| | Ligand control | CdSe-DWNTs | PPD linker | Lower coverage | Worsened charge transfer |
| | | | AET linker | Higher electron affinity | Mediocre effects on charge transfer |
| | | | ATP linker | π – conjugation | Improved charge transfer |
| | | CdSe/ZnS-MWNTs | Diazonium salt linker | Attachment onto sidewalls | Less efficient charge transfer |
| | | | Mercaptotriethoxysilane as ligand | Attachment onto ends | More efficient charge transfer |
| | | CdSe/ZnS-DNA/SWNTs | Amino-terminated linker | End attachment | Varying length and chemical nature affect properties |
| | Others | InP/ZnS-MWNTs | --- | PMMA matrix | Active layer in Solar Cell |
| | | ZnO-MWNTs | --- | VLS method | Enhanced field emission properties |
| Carbon Nanofibers | DSSC | Co _x S _y -CNFs | Chemical composition | Co ^{3+/2+} redox couple | Enhanced solar cell stability |
| | | MoO ₂ -CNFs | Thickness of the composite layer | Higher power conversion efficiency | Counter electrode in solar cell |

| | | | | | |
|--|--------|-------------------------------------|---|------------------------------------|--------------------------------------|
| | | Doped Pt ₃ Ni-CNF | Transition metal dopant | Rapid charge transport | Enhanced light-reflecting capability |
| | QDSSC | CuS-CNF | CNF network | Strong 0D-1D connection | Increased catalytic activity |
| | Others | TiO ₂ -CNF | CNF activation time | Porous structure | Water pollutant decomposition |
| | | ZnO-CNF | --- | Enhanced photocatalytic activity | Degradation of pollutant |
| | | In ₂ O ₃ -CNF | In ₂ O ₃ morphology | Efficient electron-hole separation | Degradation of pollutant |

Table 1. Summary of Carbon-based Heterostructured Systems, discussed in this Perspective.

| Heterostructure Theme Investigated | Underlying 1D Platform | Material System with Corresponding Application | | Chemical Composition | Key Parameter Tested or Observation Made | Further Elaboration of Effects on Application | Effects on Applications | |
|------------------------------------|------------------------|--|------------|-----------------------|---|---|---|--------------------------------------|
| Metal Oxides | Binary Metal Oxides | CeO ₂ - HER | | CdS-CeO ₂ | 50 times increased HER activity | 2 times longer lifetime | Photocatalytic H ₂ evolution | |
| | | SnO ₂ | Catalysis | CdS-SnO ₂ | --- | Higher activity | Photocatalytic degradation | |
| | | | Solar cell | CdSe-SnO ₂ | CdSe QDs deposited on SnO ₂ NW surface | Low photocurrent | High IPCE | |
| | | | | | Hierarchical composition | 350% higher | | |
| | | | | CIS-SnO ₂ | Cd-free QDs (at 325 nm) | 700% increase | Increased charge transfer | |
| | | | | | | ZCIS-SnO ₂ | | 400% increase |
| | | | | | | ZCIS/ZnS core/shell-SnO ₂ | | 200% increase |
| | | | | ZnO – Solar Cell | | CdS-ZnO | QD composition | Bi-sensitized photoelectrode |
| | | | | | CdSe-ZnO | Capping ligand | Faster charge transfer | Excellent quantum efficiency |
| | | | | | CdSe/ZnS core/shell-ZnO | Shell layer | Hindered charge transport | Decreased photocatalytic performance |

| | | | | | | |
|--|----------------------------|---|---------------------------|--|-----------------------------------|---|
| | | | CdTe-ZnO | --- | Efficient photoconversion | Water splitting |
| | | | PbS-ZnO | Surface morphology of ZnO | Efficient carrier collection | Heterojunction solar cell |
| | | TiO ₂ – Solar Cell & Catalysis | CdSe-TiO ₂ | TiO ₂ morphology | QD surface loadings | Pollutant degradation; IPCE value of 55% |
| | | | CdS-TiO ₂ | Attachment method | Photocatalytic activity increment | Pollutant degradation of 98.83% (highest report to date) |
| | | | CdSe/CdS-TiO ₂ | QD distribution | Efficient energy conversion | Hydrogen generation |
| | | | CdTe-TiO ₂ | --- | High photocurrent density | Pollutant degradation |
| | | | PbSe-TiO ₂ | Methyl orange degradation noted at levels of 90% | Photoinduced charge injection | Photocatalysts |
| | | | Others | PbSe-Fe ₂ O ₃ | Synthesis method | Interface matching |
| | | CdTe-ZnO/TiO ₂ | | TiO ₂ thin layer | Passivation of surface defects | PCE value of 1.44% |
| | | Ternary Metal Oxides | Orthophosphates | CdSe-CePO ₄ :Tb ³⁺ | QD loading ratio | Higher coverages; shorter lifetimes; and increased PL quenching |
| | CdSe-LaPO ₄ :Re | | | 1D vs 3D | 1D – Lower coverages | More quenching and shorter lifetimes |
| | | | | Ce ³⁺ /Tb ³⁺ /Eu ³⁺ | Band gap alignment of 3 RE ions | Tb-dopant: higher PL intensities and longer lifetimes |

| | | | | | | | |
|--|--|--------------------|--|---|--|---|--|
| | | Tungstates | CdSe-CaWO ₄ | 0D | Larger crystallite size | Higher PL output and QY | |
| | | | | 1D | Larger PL quenching | Lower PL output and QY | |
| | | | CdSe/CdS-CaW _{1-x} Mo _x O ₄ :Eu ³⁺ | CdS vs. CdSe | Larger band offset between 1D and CdSe | CdSe: more charge transfer observed | |
| | | | | X = 0, 0.2, 0.4, 0.6, 0.8, and 1 | Red shift when increasing 'x' | X = 0.8 yielded highest emission intensity | |
| | | | CdS-ZnWO ₄ | Electron transfer from CdS to ZnWO ₄ | Increase in photoactivity and stability | Photocatalyst for ciprofloxacin degradation | |
| | | | CdS-CdWO ₄ | Nanowires vs. Nanoflowers | 1D motifs yield improved photocurrents. | | |
| | | Others | β -Pb _{0.33} V ₂ O ₅ | CdSe-Pb _{0.33} V ₂ O ₅ | SILAR cycle – tuning QD surface coverage | Degree of hole transfer proportional to coverage | Light harvesting and solar cell applications |
| | | | Silicates / Silica | CdSe-Zn ₂ SiO ₄ :Mn ²⁺ | Mn doping amounts | Energy transfer from 1D to 0D and charge transfer from 0D to 1D | Controllable LED emission |
| | | | | | Aspect ratio of 1D | | |
| | | | | CdSe/ZnS-Silica glass | QD loading concentration | in situ growth inside glass tube | Near IR emission |
| | | PbS-silicate glass | QD size tuning by temperature | Different emission | Near IR emission | | |

| | | | | | | |
|---------------------|---------------------|------------------|--|--|---|--|
| Metal Chalcogenides | Binary Metal Oxides | DIR | CdSe – CdS (expand to other compositions) | QD on rod surface | Low photon- to electron QY | H ₂ generation |
| | | | | 0D core/shell | | |
| | | | | Dot in rod | Highest photon- to electron QY | |
| | | 0D-1D-0D | CdTe-CdSe-CdTe | Bar-bell | Interface lattice matching | Band edge alignment with optimized charge transfer |
| | | | ZnSe-CdS-ZnSe | Bar-bell | | |
| | | | CdSe-ZnSe | QD at one end | Lower threshold voltage, narrow bandgap | LED device |
| | | QDs on surface | CdSe-ZnS:Mn ²⁺ | Mn ²⁺ doping ratios | Orange emission | Higher ratios – ‘warmer’ light |
| | | | | QD loading ratios | Green emission | Higher amounts – ‘whiter’ hue |
| | | | HgTe-CdSe/CdS | HgTe QD | mid IR | Bi-color detector |
| | | | | Core/crown CdSe/CdS nanoplatelets | visible light | |
| | | | MoS ₂ /MoSe ₂ -CdS | MoS ₂ /MoSe ₂ few layers | MoSe ₂ as bridge | HER |
| | | Epitaxial Growth | CdS-Bi ₂ S ₃ | Surface matching | CdS size control | photocatalysis |
| | | | CdSe-CdTe | CdSe central core coupled with CdTe | CdTe phase control (zinc) | LEDs or phototransistors |

| | | | | | | |
|-----------------|----------------------------|---|-----------------------------------|--|--|--|
| | | | extended tetrapod branches | blende / würtzite); PL quenching | | |
| | Ternary Metal Oxides | CuInSe ₂ /CuInS ₂ | Dot-in-Rod | Cation exchange | Near IR luminescence | |
| | | Cu ₃₁ S ₁₆ -CuInS ₂ | Carrot shape 'head-tail' motif | Oil/aqueous interlayer synthesis | Optoelectronic devices or solar cells | |
| Metal Fluorides | NaYF ₄ | CdSe-NaYF ₄ : Yb ³⁺ /Eb ³⁺ | 0D nanospheres: α phase | Higher surface area | More PL quenching | |
| | | | 1D nanowire bundles: β phase | Lower surface area | Less PL quenching | |
| | | CdS-NaYF ₄ : Yb ³⁺ /Tm ³⁺ | Yb ³⁺ - 30% | Near-IR region | Good photocatalyst for Rhodamine B degradation | |
| | | | Tm ³⁺ - 0.5% | UV-visible region | | |
| | Other potential candidates | NaYF ₄ : with Y, Sm, Eu, Gd, Tb, Dy, and Ho elements | | | | |
| | | NaYF ₄ : Yb ³⁺ , Er ³⁺ with SiO ₂ shell | | | | |
| | | NaGdF ₄ | | | | |
| | | YF ₃ | | | | |
| | | YOF | | | | |

Table 2. Summary of Non-Carbonaceous-based Heterostructured Systems, discussed in this Perspective.